



Review

# Mid-Infrared Observations of the Giant Planets

Michael T. Roman <sup>1,2</sup> <sup>1</sup> School of Physics and Astronomy, University of Leicester, Leicester LE1 7RH, UK; m.t.roman@leicester.ac.uk<sup>2</sup> Facultad de Ingeniería y Ciencias, Universidad Adolfo Ibáñez, Av. Diagonal las Torres 2640, Peñalolén, Santiago 7941169, Chile

**Abstract:** The mid-infrared spectral region provides a unique window into the atmospheric temperature, chemistry, and dynamics of the giant planets. From more than a century of mid-infrared remote sensing, progressively clearer pictures of the composition and thermal structure of these atmospheres have emerged, along with a greater insight into the processes that shape them. Our knowledge of Jupiter and Saturn has benefitted from their proximity and relatively warm temperatures, while the details of colder and more distant Uranus and Neptune are limited as these planets remain challenging targets. As the timeline of observations continues to grow, an understanding of the temporal and seasonal variability of the giant planets is beginning to develop with promising new observations on the horizon.

**Keywords:** giant planets; atmospheres; dynamics; atmospheres; chemistry

## 1. Introduction

The mid-infrared region of the electromagnetic spectrum provides a unique and important window into the atmospheric physics and chemistry of the giant planets. Linking the near- and far-infrared, it spans a range of wavelengths (variously defined), over which the dominant source of planetary radiation transitions from scattered sunlight to intrinsic thermal emission. As the scattered solar component fades with increasing wavelength, the various features and colors that define the planets' appearances in visible and near-infrared images give way to distinct thermal structures shaped by the temperatures and chemistry of these atmospheres. Against this changing backdrop of scattered and emitted radiation, numerous molecules leave their distinct spectral signatures, indicative chemical abundances, kinetic temperatures, and ambient pressures. The observation and analysis of reflected and radiant energy can thus be used to reveal the composition, temperature, and structure of a planetary atmosphere from afar, providing remote measurements of fundamental properties largely inaccessible by other means.

From more than a century of mid-IR observations, a rich picture of the four giant planets' atmospheres has emerged. Now, with the anticipated results from the new JWST promising to revise our knowledge of these planets in the years ahead [1], we use this opportunity to look back and take stock of the field. In this review, we examine remote sensing of the Solar System's giant planets across the mid-infrared. We trace an observational history from its modest beginnings to present-day efforts, highlighting what we have learned along the way and what questions remain for future work.

### 1.1. The Mid-Infrared

Infrared radiation (IR) occupies the region of the electromagnetic spectrum between visible light and radio waves (specifically, microwaves), corresponding to wavelengths from about 750 nm to 1 mm. In the modern literature, it is commonly divided into three subdivisions—near-, mid-, and far-infrared (see Figure 1). The precise boundaries of these divisions are generally not agreed upon and differ widely across various disciplines and applications. The International Commission on Illumination [2], for example, defines the



**Citation:** Roman, M.T. Mid-Infrared Observations of the Giant Planets. *Remote Sens.* **2023**, *15*, 1811. <https://doi.org/10.3390/rs15071811>

Academic Editors: Giancarlo Bellucci and Vijay Natraj

Received: 26 November 2022

Revised: 27 February 2023

Accepted: 2 March 2023

Published: 28 March 2023



**Copyright:** © 2023 by the authors. Licensee MDPI, Basel, Switzerland. This article is an open access article distributed under the terms and conditions of the Creative Commons Attribution (CC BY) license (<https://creativecommons.org/licenses/by/4.0/>).

mid-IR as radiation with wavelengths of only 1.4 to 3 microns, while the International Organization for Standardization (ISO) [3] adopts a much broader range for the mid-IR, spanning from 3 to 50  $\mu\text{m}$ . In some engineering literature, the infrared is divided into five regions, classified as short-wave (1–3  $\mu\text{m}$ ), mid-wave (3–5  $\mu\text{m}$ ), long-wave (8–12  $\mu\text{m}$ ), and very-long (12–30  $\mu\text{m}$ ) infrared (e.g., [4]), with significant variation in the defined demarcations.

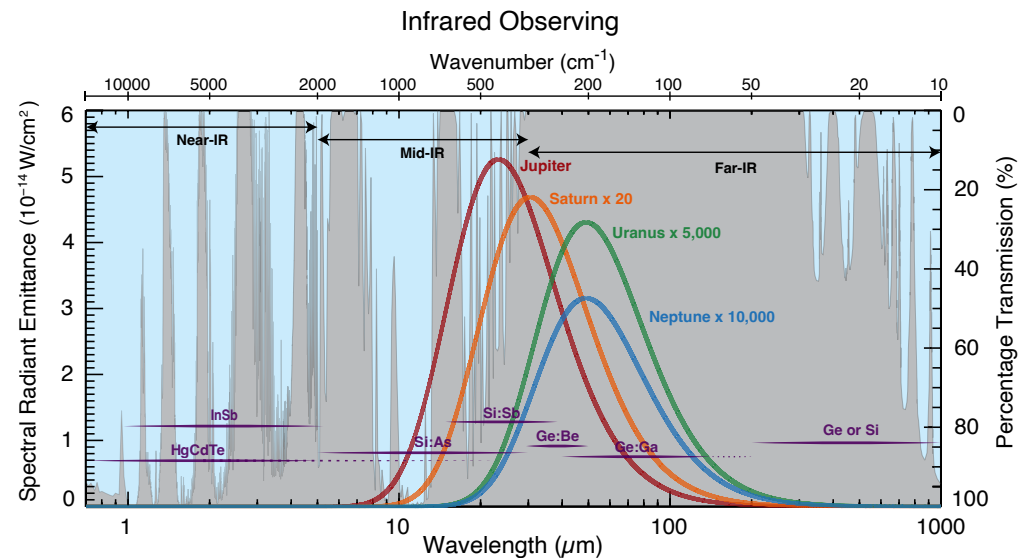


**Figure 1.** Idealized blackbody emittance of the giant planets compared to the telluric atmospheric transmission and typical detector sensitivities across the infrared. The assumed boundaries of the near-, mid-, and far-infrared regions are indicated. Colored curves show the black body spectral radiant emittance for the effective temperatures of the giant planets, accounting for their distances, scaled and labeled for clarity. Jupiter and Saturn peak in the mid-infrared, while Uranus and Neptune peak in the far-infrared. The atmospheric transmission is indicated by the blue–gray interface varying between 100% (full transmission) and 0% (total attenuation) from the top of the atmosphere down to a surface altitude of 2640 m (corresponding to the altitude of the Very Large Telescope (VLT) at Cerro Paranal, with a precipitable water vapor (PWV) of 1.66 mm at an air mass of 1.15 [5,6]). Characteristic ranges for various thermal detectors are shown in purple [7–13].

In astronomy and planetary science literature, the mid-infrared typically refers to wavelengths between roughly 5  $\mu\text{m}$  and 20 to 30  $\mu\text{m}$  [9,10,14,15]. These bounds are a natural consequence of practical constraints, namely astronomical detector technology and the transparency of Earth’s atmosphere. This adopted lower limit around 5  $\mu\text{m}$  roughly coincides with the longest wavelengths detected by most common near-infrared detectors, typically composed of indium antimonide (InSb) or mercury-cadmium-telluride (HgCdTe) (see Figure 1). At longer wavelengths, arsenic- or antimony doped silicon (Si:As and Si:Sb) Impurity Band Conduction (IBC) detectors are typically employed, sensitive to ranges of  $\sim 6\text{--}27$   $\mu\text{m}$  and  $\sim 14\text{--}38$   $\mu\text{m}$ , respectively, followed by germanium photoconductive detectors and bolometers in the far-infrared [7–13]. Case in point, the JWST Near Infrared Camera (NIRCam) instrument uses HgCdTe detectors for the 0.6–5  $\mu\text{m}$  region, while the JWST Mid-Infrared Instrument (MIRI) uses a Si:As detectors to measure radiation from 5 to 28  $\mu\text{m}$  [16–18]. As discussed in the next section, the so-called atmospheric window of infrared transparency provides a natural upper boundary to the mid-infrared around 30  $\mu\text{m}$ , beyond which little infrared radiation is transmitted through the atmosphere.

For the purpose of this review, we will adopt the definition of the mid-infrared as radiation between 5 and 30  $\mu\text{m}$  (or 2000–333  $\text{cm}^{-1}$ , in terms of wavenumber) and limit our scope to remote sensing within this wavelength range. We will also restrict ourselves to the giant planets without our Solar System, leaving the growing number of extrasolar planet infrared observations to other reviews [19,20].

### 1.2. Atmospheric Transmission, Emission, and Mid-Infrared Sub-Bands

Gaseous absorption, primarily by telluric water vapor, renders the Earth's atmosphere largely opaque to extraterrestrial infrared radiation as seen from the ground at various wavelengths. Between about 30  $\mu\text{m}$  and several hundred microns, the atmosphere is nearly continuously opaque, marking the adopted cutoff between the mid- and far-infrared (see Figure 1). Owing to this absorption, the far-infrared (or sub-millimeter) spectral region is only accessible from extremely high-altitude, airborne, and space observatories [21]. The atmospheric transparency begins to increase once again approaching the millimeter region, which has been used to sense deeper into the atmospheres of the giant planets than that which can be accessed by visible and infrared observations [22–24].

Between 5 and 30  $\mu\text{m}$ , the atmospheric transmission is more variable and frequency dependent, with  $\text{H}_2\text{O}$ ,  $\text{CO}_2$ ,  $\text{O}_3$ ,  $\text{CH}_4$ , and nitrous oxides contributing to the opacity [25–27] (see Figure 2). Strong absorption by  $\text{CO}_2$  between 14 and 17  $\mu\text{m}$  effectively blocks the atmospheric window near its center, and thus mid-infrared is typically divided into two sub-regions known as the N and Q bands in photometric systems. The precise ranges of these bands are not universally standardized, but the N band is typically recognized as ranging from roughly 8 to 14  $\mu\text{m}$ , while the Q band extends between 17 and 25–27  $\mu\text{m}$  [9,10]. These bands are often divided further into various sub-bands for filtered imaging (e.g., Q1, Q2, Q3, etc.), naturally demarcated by the numerous absorption lines [9,28].

Additionally, corresponding to a narrow window of atmospheric transparency between 4.6 and 5.0  $\mu\text{m}$ , the M band straddles the rough boundary between the near- and mid-infrared. It has been grouped with the mid-infrared in at least some literature (e.g., [29]), although it is more commonly considered as a near-infrared band [9].

The gases in Earth's atmosphere do not only absorb radiation—they also emit, with an emission spectrum characteristic of the atmospheric temperature and composition. Given the Earth's effective temperature of 255 K, the atmosphere's black body thermal emission peaks near 12  $\mu\text{m}$  (see Figure 2). Likewise, the telescope itself inescapably emits thermal radiation corresponding to the observatory's ambient temperature (typically 280–290 K at the VLT, for example [30,31]) leading to an additional source of thermal radiation that also peaks in the N-band [31]. This combined telluric emission easily overwhelms the faint celestial emission from the colder, distant atmospheres of the outer planets. One solution to this problem is to actively cool the instrument and to place the telescope above as much of the Earth atmosphere as possible, ideally well into space. However, when space is out of reach, observations from the ground are still possible over much of the mid-IR owing to specialized techniques developed by observers over the past century.

The standard approach is to attempt to remove the thermal contribution of the sky and telescope by a process known as chopping and nodding [32]. Chopping entails oscillating the telescope's secondary mirror at a frequency of several hertz, cycling on and off target in order to isolate and subtract the sky's thermal contribution from the total signal. Likewise, nodding attempts to remove the residual, non-uniform emission from the telescope by alternating the telescope's pointing every few minutes. By this approach, measurements of Uranus' 13- $\mu\text{m}$  emission, for example, can be made from the ground despite being roughly 100,000 times fainter than the combined sky and telescope emission [33]. However, even this approach cannot overcome the atmosphere's considerable infrared opacity beyond the atmospheric window, and significant portions of the infrared spectrum (e.g.,  $\sim 5.5\text{--}8\ \mu\text{m}$ , 13.5–17  $\mu\text{m}$ , and 25–30  $\mu\text{m}$ ) remain inaccessible from the ground.

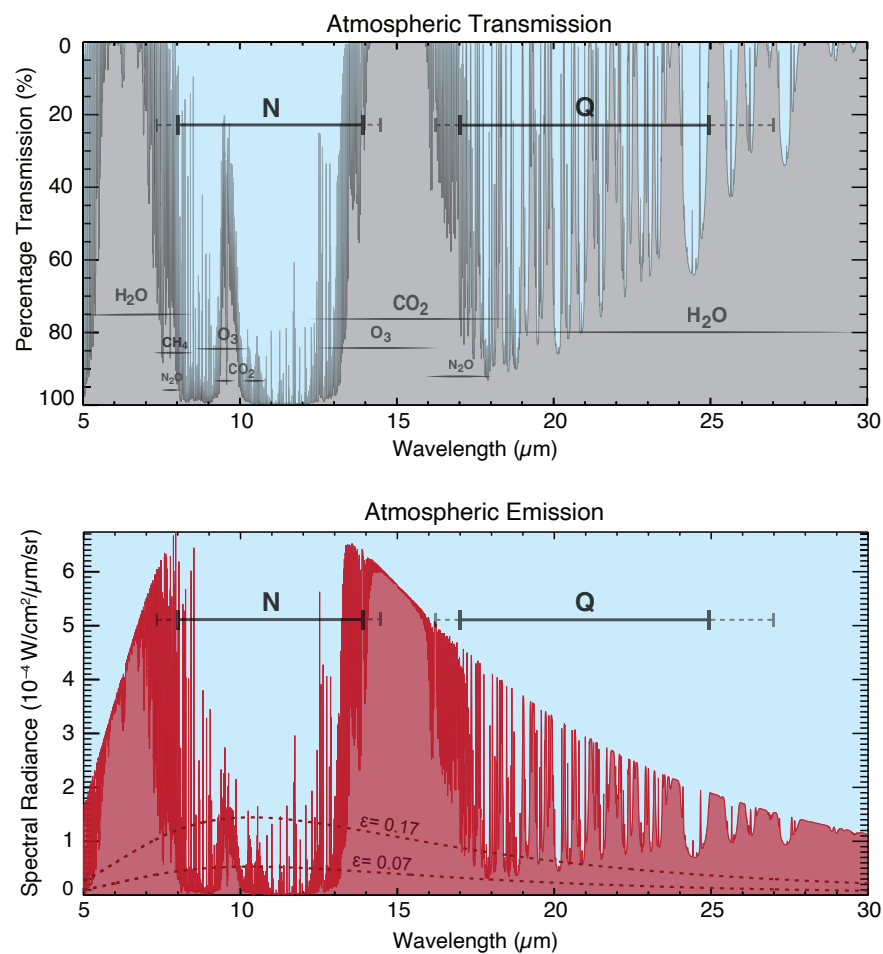


**Figure 2.** The atmospheric transmission (top) and emission (bottom) in the mid-IR, for conditions at Cerro Paranal, as described in Figure 1. Transmission is indicated by the blue–gray interface varying between 100% (full transmission) and 0% (total attenuation) from the top of the atmosphere down to the surface [5,6]. Emission from the atmosphere is indicated by the red shaded curve, assuming annual average temperatures, 1.5 mm PWV, and an airmass of 1.16. Additional emission from the telescope is shown for two different assumed values of emissivity, spanning typical values found in the literature ( $\epsilon = 0.07\text{--}0.17$ ) [31,34,35], and typical ambient temperature of 280 K. The total telluric thermal radiance is orders of magnitude greater than that received from the giant planets.

### 1.3. Why We Observe in the Mid-Infrared

While observations of scattered sunlight at visible wavelengths define our most familiar views of the giant planets, they do not reveal a complete picture of the important processes that shape these atmospheres. A complementary understanding of the atmospheric environment, within and above the clouds, can be achieved with infrared observations. Although scattered sunlight from aerosols can contribute to mid-IR radiances (particularly at shorter wavelengths), mid-IR is dominated by intrinsic emission from the atmosphere, indicative of temperature and composition (see Figure 3).

With effective temperatures of less than 125 K, the idealized black body emission of the Solar System’s giant planets primarily emit energy in the infrared region of the electromagnetic spectrum. The spectral radiant black body emission of Jupiter’s and Saturn’s peak in the mid-infrared, while emission from the colder atmospheres of Uranus’ and Neptune’s peak at longer wavelengths of the far-infrared (see Figure 2). In either case, considerable energy is radiated in the mid-infrared, and this thermal emission is relatively more accessible to observers on Earth’s surface than that radiating in the far-infrared. Understanding the temperature structure and energy budget of these giant planets, therefore, requires mea-

measurements of mid-infrared radiances. This idealized picture of the mid-infrared emission is, however, complicated—and greatly enriched—by the presence of radiatively active molecules, which profoundly alter the emission spectrum.

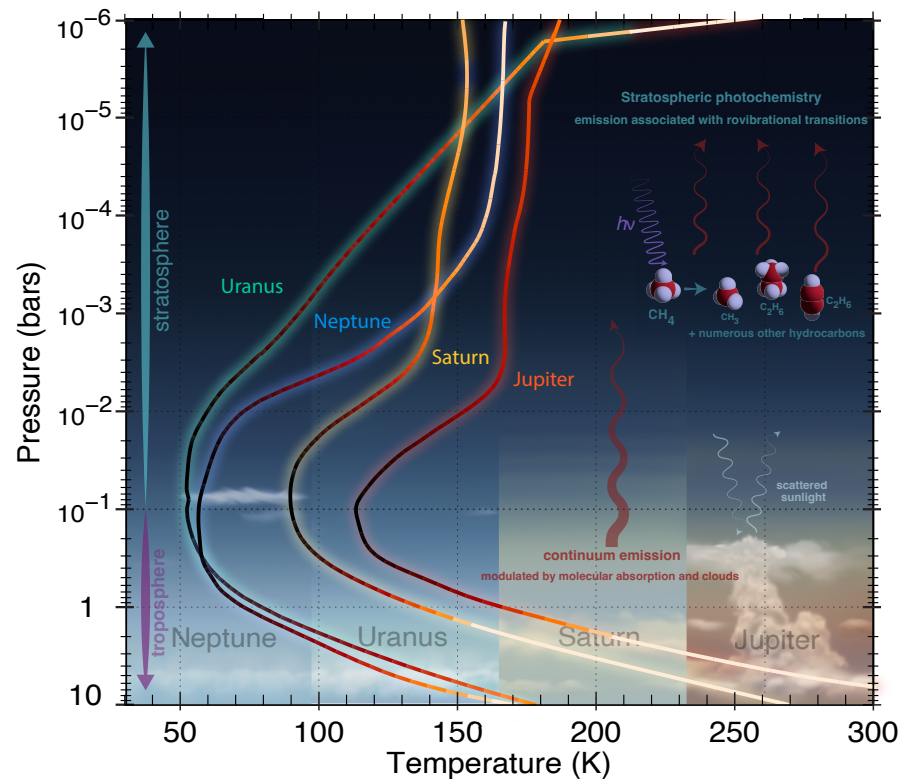


**Figure 3.** Contributions to observed mid-infrared emission from the giant planet atmospheres. Vertical temperature profiles for Jupiter, Saturn, Uranus, and Neptune are shown for pressures ranging from 10 bar to 1 microbar. While scattered sunlight from aerosols weakly contributes at shorter wavelengths, the mid-IR is dominated by intrinsic thermal emission from the atmosphere. The mid-IR emission originates from heights above the cloud layers, within the upper troposphere and lower stratosphere. Stratospheric emission is primarily associated with various stratospheric hydrocarbons that result from methane photochemistry.

The mid-infrared is home to rotational-vibrational transitions of numerous molecules found in the giant planet atmospheres, including  $\text{CH}_4$ ,  $\text{C}_2\text{H}_6$ ,  $\text{C}_2\text{H}_2$ ,  $\text{NH}_3$ ,  $\text{PH}_3$ ,  $\text{H}_2\text{O}$ ,  $\text{C}_2\text{H}_4$ ,  $\text{CH}_3$ ,  $\text{GeH}_4$ ,  $\text{AsH}_3$ ,  $\text{C}_6\text{H}_6$ ,  $\text{CO}_2$ , and more [36–39]. In spectroscopic observations, these state transitions show up as emission or absorption features, depending on the vertical temperature and chemical structure within the atmosphere. The intensity of spectral lines is dependent on both the abundance of the emitting or absorbing molecule and its ambient pressure and temperature (assuming local thermodynamic equilibrium, which may be assumed generally valid at pressures corresponding to the tropospheres and lower-to-mid stratospheres). If the ambient temperature is known, the molecular abundance can be inferred, typically by comparison of the observations with simulations from theoretical radiative transfer models (e.g., [40]). Alternatively, if the molecular abundances are known, the observed spectrum can be used to constrain the temperature. The greater the spectroscopic resolution of the observations, the better the vertical resolution of the inferred temperatures or abundances. Imaging essentially provides an integrated radiance over a finite passband and, therefore, yields poorer vertical resolution (effectively vertically averaging), but it typically has the advantage of greater angular (spatial) resolution and radiometric sensitivity.

The detection and measurement of specific molecules can provide unique insight into processes active in giant planets' atmospheres. Some species are expected as a result

of a solar composition atmosphere in thermodynamic chemical equilibrium ( $\text{CH}_4$ , for example [41,42]), but are nonetheless useful as indicators of temperatures, vertical structure, and circulation [43–46]. Others are unexpected given the ambient temperatures and bulk chemistry, and they require specific mechanisms to explain their abundances (for example,  $\text{CO}_2$  [47] and  $\text{H}_2\text{O}$  [48] in Uranus atmosphere, implying external, meteoric sources).

N-band (8–14  $\mu\text{m}$ ) spectroscopy and imaging have been used in numerous investigations to infer temperatures, chemistry, and aerosol abundances in the troposphere and stratosphere of Jupiter (e.g., [49–54]) and Saturn (e.g., [55–65]). For Uranus and Neptune, the N band has been used to measure stratospheric emission associated with hydrocarbons (e.g., [33,66–74]), but interpretations have been limited by larger uncertainties in both temperatures and chemical abundances.

The dominant components of giant planets' atmospheres are hydrogen and helium, the collision of which produces continuum absorption dependent on the pressure and temperature. Since the abundance of hydrogen and helium are homogeneous and relatively well constrained by the overall atmospheric density, this collision-induced absorption (CIA) provides a powerful, unambiguous indicator of the atmospheric thermal structure. Q-band observations (17–25  $\mu\text{m}$ ) are dominated by this absorption, and have thus successfully been used to infer atmospheric temperatures in the upper tropospheres of all the Solar System giant planets (e.g., [33,50,51,61,65,72,74–79]). Hydrogen *emission* can also be found in the Q band, and this can additionally serve as a remote sensing thermometer of the stratosphere, as discussed in Section 3.1.

Observations at roughly 5  $\mu\text{m}$  have notably been used to study Jupiter's deep atmosphere [80–88], producing striking, high-contrast images of Jupiter's clouds silhouetted against the underlying thermal emission as shown in Figure 4. (See [89] for a review of 5- $\mu\text{m}$  imaging of Jupiter, and see [90] for a review of Jupiter's deep clouds). Saturn show less contrast at 5  $\mu\text{m}$  owing to thicker, scattering hazes, but such observations have helped constrained vertical cloud structure and deeper chemistry [91–96]. As a consequence of their colder temperatures and weakly scattered sunlight, the Ice Giants have smaller radiances at 5  $\mu\text{m}$ , and as a result, have largely been unexplored at this wavelength [69,76,97]. JWST promises to provide the first detailed observations of the Ice Giants in this spectral region in the years ahead. It will be one of many observational breakthroughs that JWST promises in the mid-infrared, as it observes the giant planets with unprecedented precision and sensitivity.

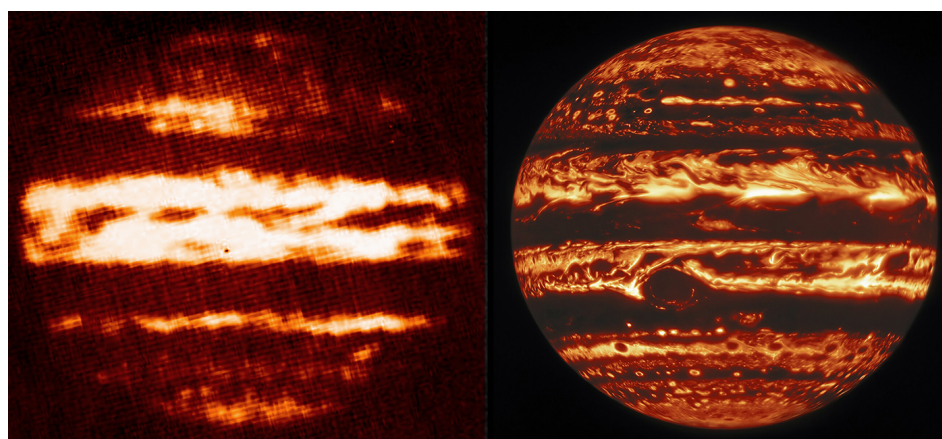


**Figure 4.** Images of Jupiter at roughly 5  $\mu\text{m}$ . Brighter regions indicate strong thermal radiation emerging from the atmosphere below the clouds, while darker patches reveal opaque clouds, silhouetted by underlying thermal emission. The image on the left is one of the earliest examples of 5- $\mu\text{m}$  imaging, made with the Hale 200-in (5-m) telescope at Palomar Observatory in 1973 [83]. The 4.7- $\mu\text{m}$  image on the right is from the Near-InfraRed Imager (NIRI) instrument [98] at Gemini North in Hawai'i, composed of multiple images captured in 2017 [99]. The images reveal the dramatic improvement in the imaging quality, as well as changes in cloud structure over the past half-century.

## 2. A Historical Overview: Observing the Giant Planets in the Mid-Infrared

Infrared characterization of the giant planets developed in parallel with the evolution of broader infrared astronomy in general. It is marked by advances in theory, technology, and techniques that sparked new discoveries, inevitably prompting new theories, technologies, and techniques. Unlike galactic and most stellar astronomy, however, planetary astronomy has the advantage of being able to apply remote sensing with relatively generous proximity, including very close encounters via robotic spacecraft. Robotic missions to the giant planets have afforded leaps in knowledge in recent decades, building upon and complementing a long history of ground-based observing. Beginning with basic measurements of effective planetary temperatures, mid-infrared investigations grew to provide critical insight into the chemistry, structure, and dynamics of the giant planets.

Repeatedly over this observational history, Jupiter, by virtue of its superior size, proximity, and brightness, was naturally investigated first and most thoroughly. Successful investigations were then typically extended to Saturn shortly thereafter. Finally, Uranus and Neptune, owing to their great distances and cold temperatures, were investigated if and when even viable, consistently lagging many years behind the Gas Giants in thermal and chemical characterization.

### 2.1. Beyond the Visible: Measuring Heat from the Giant Planets

In the closing year of the 18th century, William Herschel demonstrated that radiant heating from the Sun extended beyond the red light of the visible spectrum [100], arguably marking the birth of infrared astronomy. Over the following century, quantitative investigations of this “invisible thermometrical spectrum” and the infrared properties of materials developed alongside innovations in optics and instrumentation (e.g., see early reviews by [101]). As theory and tools developed, astronomers pushed their observations further into the uncharted infrared spectrum while aiming their instruments at increasingly fainter celestial targets.

Beginning in the late 1850s, the first successful measurements of the “non-luminous” radiation from the Moon’s surface were made using telescopes equipped with sensitive early thermopiles, which converted observed radiative energy into electrical energy that was then read as needle deflection on a galvanometer. Increasingly sensitive radiometers were subsequently developed, including the Langley bolometer in 1878 [102], giving rise to an enduring limerick, dubiously attributed to Langley’s student:

“Prof. Langley devised a Bolometer.  
It’s really a sort of Thermometer.  
It’ll detect the heat  
Of a Polar Bear’s feet  
At a distance of Half-a Kilometer.” [103,104]).

The bolometer has found continued use in modern submillimeter instruments [105] (e.g., Herschel-PACS [106]).

Lacking spectrometers with dispersive prisms and gratings tuned to the infrared [101,107,108], early observers simply used glass filters, transparent to visible light but opaque to thermal radiation, to remove and isolate the thermal component from the total observed radiation. This filtering approach provided ratios of relative band radiances, leading to the first (somewhat disputed) estimates for the extreme diurnal range of lunar surface temperatures [109–113].

By the early 20th century, observations extended progressively further into the mid-infrared. Improved radiometers and observing techniques were combined with larger reflecting telescopes to provide the first quantitative estimates of thermal emission from the planets. In pioneering work by Coblentz and Lampland [114–118] and Pettit and Nicholson [119,120], observations of Venus, Mars, Jupiter, Saturn, and Uranus were made between 1914 and 1924 using sensitive new radiometers and a series of filters in order to separate observed radiances into five discrete spectral bands ranging between 0.3  $\mu\text{m}$  to

15  $\mu\text{m}$ —specifically, a water cell 1 cm in thickness was used to pass radiation between 0.3 and 1.4  $\mu\text{m}$ , while filters of quartz, glass, and fluorite were transparent up to 4  $\mu\text{m}$ , 8  $\mu\text{m}$ , and 12.5  $\mu\text{m}$ , respectively (see Figure 5).

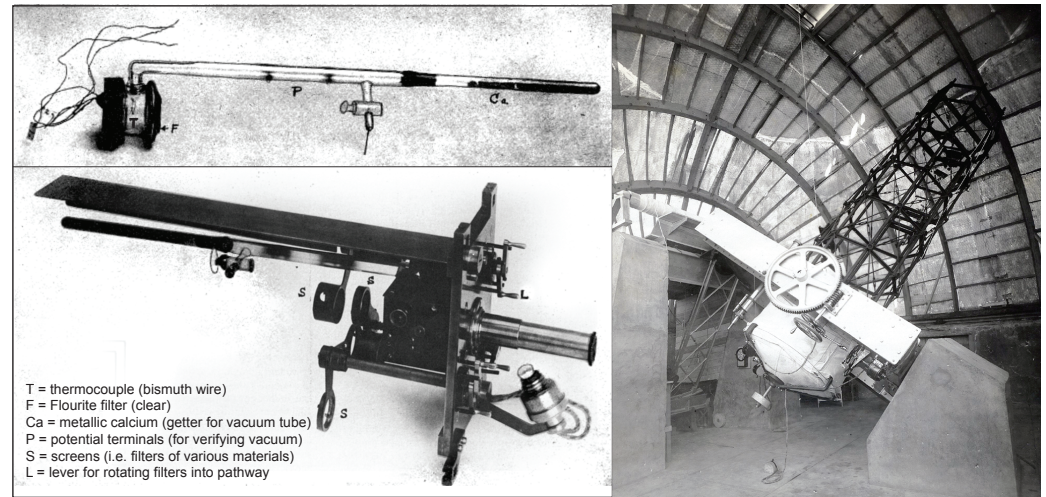


**Figure 5.** Photographs of the Coblentz-Lampland radiometer, used to make groundbreaking measurements of thermal from stars and the giant planets [115]. Top left: Evacuated glass tube containing the thermocouple—a wire of bismuth that converts temperature differences to electric voltage via the thermoelectric effect. The thermocouple is kept in an evacuated tube, with the vacuum maintained by the presence of reactive calcium metal (serving as a getter). Bottom left: The thermocouple is placed into the radiometer, which was fastened to the photographic plate holder of the telescope. The thermocouple was placed in the optical path between the target and eyepiece, while filters of different passbands were selectively rotated in and out of view. By these means, coarse spectra could be inferred. Right: The Lampland 40-inch telescope of the Lowell Observatory, on which the radiometer was mounted for much of Coblentz’s planetary work, inside its dome, ca. 1909 (*Image credit: Slipher, E.C., “The 42-inch Lampland Telescope inside of its dome,” Lowell Observatory Archives, <https://collectionslowellobservatory.omeka.net/items/show/1047>, accessed on 22 December 2022*).

The combination of filtered observations thus provided the first rough spectra of the giant planets. Analysis of these spectral data revealed Jupiter and Saturn to have temperatures (at the effective emission layers) of 120–140 K and 125–130 K, respectively, while Uranus was colder yet, with an upper limit of 100 K [121,122]—not far from modern estimates of planetary effective temperatures:  $124.4 \pm 0.3$ ,  $95.0 \pm 0.4$ , and  $59.1 \pm 0.3$  for Jupiter, Saturn, and Uranus, respectively [123]. These measured temperatures indicated the giant planets were cold—not much warmer than expected for equilibrium with the solar heating—and therefore contributed to evidence that the low density of the outer planets could only be explained by a bulk composition rich in hydrogen [124].

Over the following decades, improvements in technology and technique continued. Advances in mid-infrared bandpass filters and gratings (i.e., those that transmit only in the mid-infrared) enabled improved calibration of stars and planets by allowing for the direct comparison with known blackbody cavities at the telescope [125]. Errors due to the drift in detector response and changing sky radiance were minimized by shifting the sensor on and off target at high frequency [125–127]—an approach that evolved into the chopping and nodding technique still used today to remove the thermal signal of the sky and telescope [32,128]. By the 1960s, photometric systems utilizing mercury-doped germanium detectors cooled by liquid hydrogen allowed for increased sensitivity in the mid-infrared spectral region [128].

Utilizing the new detectors and techniques, observations in the early 1960s provided the first truly spatially resolved photometry of the thermal radiation emitted by a giant planet. Beginning in 1962, radiances across the disk of Jupiter were measured at 8–14  $\mu\text{m}$

using the Palomar Observatory Hale 200-inch telescope—the world’s largest telescope at the time. These spatially resolved data revealed thermal limb-darkening indicative of temperatures increasing with depth; temperature contrast ( $\sim 0.5$  K) between the warmer darker belts and the cooler brighter zones [129]; and that the Great Red Spot (GRS) was 1.5–2.0 K cooler than the surrounding disk (see Figure 6).

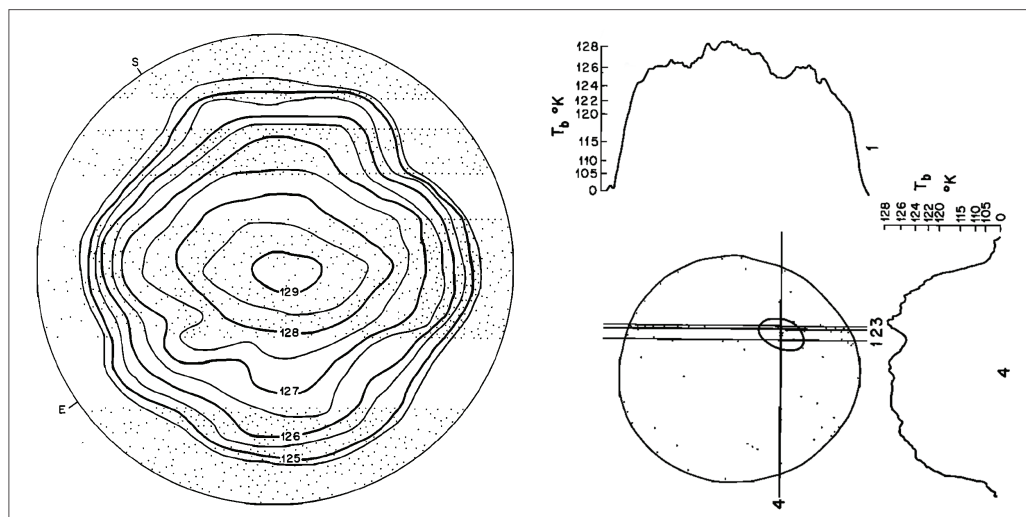


**Figure 6.** Among the earliest maps of Jupiter’s mid-infrared radiances, reproduced from Murray et al. [129]. Left: Contours show brightness temperatures derived from 8 to 14  $\mu\text{m}$  observations, made over five nights in mid-December 1963 using the Hale 200-inch (5.1 m) Telescope of the Palomar Observatory. The contours indicate modest limb-darkening and early hints of possible zonal thermal structure, with the visible belt-zone structure superimposed (oriented south pole upwards). Right: Perpendicular lines represent scans passing through the Great Red Spot (GRS). Corresponding brightness temperature curves (as numbered just to the right and above) show a depression in temperature at the location of the GRS.

Soon after, the first observations of Saturn and Uranus at 10  $\mu\text{m}$  [130] and 17–25  $\mu\text{m}$  [131,132] were made and flux calibrated by comparison to recently defined photometric standard stars. These observations yielded a 20- $\mu\text{m}$  brightness temperature and  $95 \pm 3$  K for Saturn, roughly consistent with modern values, and  $55 \pm 3$  K for Uranus, which established “the current lower limit to the brightness temperature of a celestial object which can be measured in the infrared” [132]. The opacity of Earth’s atmosphere limited the infrared spectrum that can be obtained from the ground, leading observers to seek greater heights.

Observations from airborne observatories began in the 1960s, with rockets [133,134], balloons [135,136], and jets [137,138] rising above Earth’s moist lower atmosphere. A 12-inch telescope flown on a modified Lear jet (NASA 701) in 1968 captured thermal radiances from Jupiter and Saturn using a series of broad filters with bandpasses sampling the spectrum between 1.5  $\mu\text{m}$  to 350  $\mu\text{m}$ . Analysis of these brightness temperatures showed that both Jupiter and Saturn radiated roughly twice as much energy as they receive [137,138]. The energy balances—ratios of emitted to received radiation—for Jupiter and Saturn have since been revised down to 1.7 and 1.8, respectively, following Voyager measurements [139]; however, following Cassini, the balance for Jupiter was raised to 2.1 [140], while Saturn was shown to be seasonally variable [141].

Neptune’s thermal emission was finally measured years later, when, in 1972, observations were made from the newly constructed high-altitude observatory on Maunakea. At over 4200-m above sea level, the observatory’s altitude sits above a majority of the Earth’s attenuating water vapor, permitting observations further into the mid-infrared. Both Uranus and Neptune were observed between 17 and 28  $\mu\text{m}$  using a liquid-helium-cooled bolometer mounted on a 2.24-m telescope [142,143]. Surprisingly, it was discovered that Neptune had a brightness temperature of  $57.2 \pm 1.6$  K at 24- $\mu\text{m}$ —warmer than that

of Uranus ( $54.7 \pm 1.6$  K) despite Neptune's greater distance from the Sun [143–145]. Combined with observations in the visible, far-infrared, and millimeter wavelengths, this led to the conclusion that Neptune radiates excess heat— $2.4^{+1.3}_{-0.9}$  times as much power as it absorbs [146]—similar to Jupiter and Saturn. Uranus was evidently the outlier, as the only giant planet apparently lacking an internal heat source.

Observations continued to improve over the following decades, refining these initial temperature measurements with effective temperatures constrained at longer and longer wavelengths, including far-infrared [147,148], sub-millimeter [149], millimeter [150–152], and microwave [153,154] wavelengths. Spatially resolving the temperature structure on the Ice Giants had to wait for spacecraft encounters and larger telescopes in the following decades. Meanwhile, the spectral resolution was quickly improving from the ground, allowing for the detection of discrete spectral signatures [14,155].

## 2.2. A New Window into the Giant Planets' Atmospheric Composition

In the 1970s, the focus of mid-infrared planetary studies arguably shifted from temperatures to chemistry. Until then, the detection and measurement of the atmospheric composition had been investigated primarily in the visible and near-infrared for the better part of a century [41,156–162], but such observations had only succeeded in spectroscopically identifying molecular hydrogen ( $H_2$ ) and methane ( $CH_4$ ) in the giant planets, plus ammonia ( $NH_3$ ) in Jupiter and Saturn. Based on assumptions of solar-composition in chemical and adiabatic equilibrium, the newly-constrained atmospheric temperatures of the planets were used to predict theoretical abundances of several hundred volatile compounds throughout Jupiter's atmosphere [42,163], while photochemical models were predicting disequilibrium of stratospheric hydrocarbons such as ethane ( $C_2H_6$ ) and acetylene ( $C_2H_2$ ) due to photolytic destruction of  $CH_4$  [164,165]. The mid-infrared provided a promising new window to potentially detect these molecular signatures via fundamental rovibrational and pure rotational transitions.

In 1973, excess radiance at 11–14- $\mu m$ —as seen in moderate resolution ( $R \sim 50$ –66) spectra of Jupiter [80] from the ground at  $\sim 2500$ -m (8200-ft) altitude—was correctly identified as the first evidence of stratospheric  $C_2H_6$  and  $C_2H_2$  on Jupiter, enhanced by an atmospheric temperature inversion [166,167], confirming photochemical model predictions [164,165]. This 12- $\mu m$   $C_2H_6$  enhancement was also seen in the spectrum from Saturn the following year [168].

Following from theory and techniques applied in the analysis of terrestrial satellite data [169,170], spectral inversion techniques were at this time being developed for the giant planets in order to infer vertical temperature profiles and chemical abundances [171,172]. In particular, Taylor [171] showed that measurements of the  $\nu_4$  branch of  $CH_4$  (at  $\sim 7.74$   $\mu m$ ) could be inverted to provide temperature profiles for relatively warm Jupiter and possibly Saturn. For colder Uranus and Neptune, collision-induced rotational  $S(0)$  absorption by hydrogen at 25–40  $\mu m$  could be used to infer temperature profiles. Indeed, measurements of  $S(0)$  and  $S(1)$  collision-induced  $H_2$  absorption were successfully used to retrieve upper tropospheric temperature structure in the giant planets from Voyager-IRIS spectra decades later [173].

An instrumental leap forward came with the advent of high-resolution Fourier Transform Spectrometers (FTS) in the late 1960s [155,174,175], which allowed for greater spectral resolution ( $R > 500$ ) at longer wavelengths. With the promise of further discoveries already evident in modest-resolution high-altitude observations [80], high-resolution mid- and far-infrared spectroscopy rapidly emerged, opening a window to new molecules and greater constraints on atmospheric composition and vertical temperature structure.

Spectroscopy in the decade that followed yielded the first detections of  $CH_3D$  [176],  $13-NH_3$  [177],  $H_2O$  [178],  $PH_3$  [179,180],  $GeH_4$  [84], and  $CO$  [181,182] in the atmosphere of Jupiter. Given that  $PH_3$ ,  $GeH_4$ , and  $CO$  are not thermodynamically stable at the low temperatures and pressures at which they were detected, their presence suggested strong vertical mixing from below producing tropospheric disequilibrium chemistry [183,184]. Similarly,  $CH_3D$  [185] and  $PH_3$  [186,187] were detected in Saturn's atmosphere, along with

conclusive evidence of stratospheric  $C_2H_6$  [188] and tentative detection of  $C_2H_4$  [189].  $NH_3$  was also found [190], but at a factor of at least 20 less than on Jupiter, consistent with Saturn's colder temperature and deeper condensation levels. Likewise, disequilibrium  $GeH_4$  on Saturn was not detected until a decade later [191]. With even greater distances and colder temperatures, the chemistry (and temperature structure) of Uranus and Neptune remained almost unconstrained in the mid-infrared until their encounter with Voyager 2.

### 2.3. Remote Sensing Up Close: Missions to the Giant Planets

Beginning in the 1970s, robotic spacecraft missions to the giant planets permitted infrared remote sensing of the giant planets at relatively close proximity without attenuation from the Earth's atmosphere. Infrared radiometers on Pioneer 10 and Pioneer 11 flew by Jupiter in 1973 and 1974, respectively, [192], equipped with broadband filters (11- and 26- $\mu\text{m}$ -wide) centered at roughly 20  $\mu\text{m}$  and 40  $\mu\text{m}$ , respectively. Though broadly filtered in wavelength, the spatially resolved measurements provided new, stronger constraints on the energy balance [193,194] and thermal structure of Jupiter [49]. Similarly, Pioneer 11 observed Saturn in 1979, providing similar refinements of Saturn's thermal structure and energy balance [43,195], before continuing out towards interstellar space. The first to encounter Jupiter and Saturn, the Pioneer missions were envisioned as precursors to a more ambitious Mariner program mission to the giant planets, later renamed as the Voyager Program.

Launched in 1977, Voyager 1 and Voyager 2 carried the Infrared Interferometer Spectrometer and Radiometer (IRIS) experiment—arguably the most fruitful infrared instrumentation in the history of solar system exploration. A combination of three instruments, IRIS included a Michelson interferometer that operated in the infrared from 2.5  $\mu\text{m}$  to 55  $\mu\text{m}$  (180 and 2400  $\text{cm}^{-1}$ ) with a spectral resolution of  $R \sim 42\text{--}558$  (4.3  $\text{cm}^{-1}$ ), in contrast to the Pioneer radiometer's filters.

Voyager 1 reached Jupiter in March 1979, followed four months later by Voyager 2. Initial findings from these observations included refined estimates of the effective temperature and energy balance [196]; improved measurements of meridional thermal structure and cold anomaly of the Great Red Spot (GRS) [197]; confirmation of excess thermal emission near Jupiter's north magnetic pole [198] new constraints on the ammonia cloud density and particle sizes [199]; new constraints on the chemical abundances [197], including that of helium [200]; and the first detection of several new hydrocarbons, including  $C_2H_4$ ,  $C_3H_4$ , and  $C_6H_6$  [198]. Similarly, IRIS placed new constraints on the temperature structure and chemistry of Saturn during the Voyager 1 and Voyager 2 encounters in 1980 and 1981, respectively, [44,55,201–205]. Following the Saturn encounters, Voyager 1 began its extended mission on course to depart the solar system, while Voyager 2 continued onward towards the Ice Giants.

The subsequent Voyager 2 flybys of Uranus in 1986 and Neptune in 1989 marked watershed moments in the exploration of the outer planets. With unprecedented spatial resolution and phase-angle coverage, Voyager substantially improved constraints on the Bond albedos, effective temperatures, thermal structure, and energy balances [139,206–208] of both planets, confirming that Uranus was indeed anomalous in its lack of interior heat. In particular, the spatial resolution allowed the upper-tropospheric temperature structure of both planets to be mapped for the first time, revealing relative cold anomalies (2–4 K) at mid-latitudes compared to the warmer low and high latitudes [209]. This latitudinal structure was interpreted as evidence of mid-latitude upwelling and resulting adiabatic cooling as part of a meridional circulation cell, compensated by downwelling at the equator and poles [209–211]. New constraints were also placed on the helium abundances of both planets [207,208], although stratospheric hydrocarbons remained poorly constrained due to insufficient instrument sensitivity at wavelengths less than 25  $\mu\text{m}$ . Nonetheless, the Voyager 2 flybys of the Ice Giants remain to be the only close encounter with these distant worlds and the definitive account of their temperature structure.

Notably, the IRIS observations also allowed for the first measurement of ortho-para hydrogen disequilibrium in the outer planets. Pressure-induced  $H_2$  absorption at  $\sim 17$   $\mu\text{m}$

and  $\sim 27 \mu\text{m}$  result from transitions in ortho- $\text{H}_2$  and para- $\text{H}_2$  energy levels, respectively, and the ratio of these absorption features are theoretically dependent on temperature [212,213]. Conrath and Gierasch found ortho-para fractions were not in equilibrium with the retrieved temperatures on Jupiter, particularly at the equator, implying upwelling from warmer depths [214]. Combined with implied zonal wind shear inferred from thermal wind relations, these observations provided powerful new insight into the atmospheric circulation on the giant planets [72,77,173,201,215].

Following the success of Voyager, the Galileo orbiter examined the Jupiter system over the course of 35 orbits between 1995 and 2003 [216–219]. On-board instruments included the Near-Infrared Mapping Spectrometer (NIMS) [220], which observed from 0.7 to 5.2  $\mu\text{m}$ , and the Photopolarimeter-Radiometer (PPR) experiment [221], which observed in five mid-infrared spectral bands between 15 and 100  $\mu\text{m}$ . The NIMS spectra, combined with contemporaneous visible imaging, found evidence of deep water clouds [222] and showed that most, *but notably not all*, bright clouds blocking thermal emission extended vertically to the upper troposphere [223–225]. The PPR was used to derive the 200–700-mbar temperature field of the Great Red Spot (GRS) using four discrete mid-infrared filters centered on 15, 22, 25, and 37  $\mu\text{m}$ . These filtered data showed that the GRS was roughly 3 K colder than regions to its east and west, consistent with Voyager and previous investigations [226].

While Galileo was still in orbit around Jupiter, the next great flagship mission to the outer planets was already en route to Saturn. The Cassini-Huygens spacecraft launched in 1997, beginning its two-decade-long journey of exploration [227,228]. It observed Jupiter over a period of roughly six months, reaching its closest approach in December 2000 at just under 10 million kilometers [229], before entering orbit around Saturn in July 2004.

The Cassini spacecraft was equipped with two state-of-the-art instruments sensitive to the infrared: the Cassini Visual and Infrared Mapping Spectrometer (VIMS) [230] and the Composite Infrared Spectrometer (CIRS) [231,232]. VIMS was an improved successor to Galileo-NIMS [220] (even inheriting some of its mechanical and optical parts from the original NIMS engineering model [230]). As an imaging spectrometer, it produced spectra for each pixel (or *spaxel*) in an image. It was composed of a visible and infrared channel, allowing for measurements from the ultraviolet to the edge of the mid-infrared (0.3–5.1  $\mu\text{m}$ ). By simultaneously sensing both near-infrared scattering and thermal emission, VIMS allowed for new constraints on Saturn's cloud opacity and composition [94,233–235] (see Figure 7). For observations at longer wavelengths, Cassini's CIRS instrument was used [231,232]. Unlike Galileo's infrared instrument (PPR), Cassini's CIRS was a proper spectrometer. Following the FTS principles used since the 1960s, CIRS was composed of a mid-infrared Michelson interferometer and a far-infrared polarizing interferometer that could together provide spectra from 7.1 to 1000  $\mu\text{m}$  at a spectral resolution that could be set between 0.5 and 15.5  $\text{cm}^{-1}$ .

With its unprecedented spectral coverage, CIRS observations of Jupiter provided new constraints on temperature structure [236], energy balance [237], cloud structure and composition [87,238,239], and chemical abundances, including that of  $\text{NH}_3$  [240],  $\text{PH}_3$  [241,242],  $\text{C}_2\text{H}_2$  [243] and  $\text{C}_2\text{H}_6$  [243], the D/H ratio [244], halides [245], and trace hydrocarbons [246,247]. Then, from its unrivaled vantage point in orbit around Saturn for more than 13 years, CIRS revolutionized our understanding of Saturn's seasonally variant chemistry and thermal structure [78,231,248–253]. It placed the new and improved constraints on numerous molecular and isotopic abundances [45,60,242,244,254–262]. The CIRS observations of Saturn remain the definitive measurements of the planet at mid-infrared wavelengths, and largely define our current knowledge of Saturn's temperature and chemistry (see [263] for a comprehensive review).

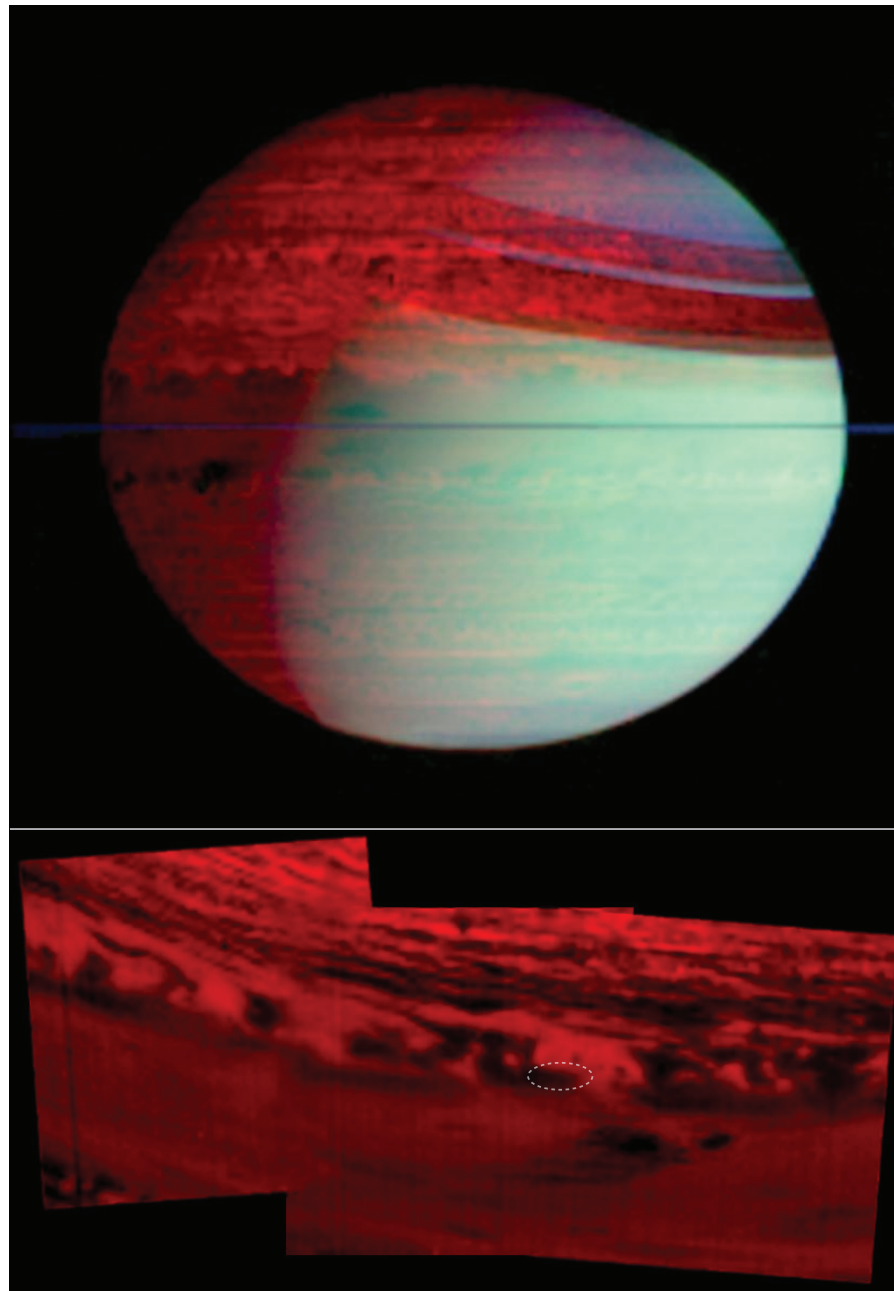


**Figure 7.** Images of Saturn from Cassini-VIMS. Top: False-color mosaic of Saturn from February 2006 showing thermal infrared radiation at 5.02- $\mu\text{m}$  (in red) and scattered sunlight at 1.07  $\mu\text{m}$  and 2.71  $\mu\text{m}$  (in blue and green, respectively). Discrete clouds appear silhouetted against the glow of Saturn's thermal emission at 5- $\mu\text{m}$ , while the rings cast a shadow upon Saturn's northern hemisphere. Bottom: The last images from VIMS, captured on 14 September, 2017, as the spacecraft made its final descent towards Saturn. Thermal emission at 5  $\mu\text{m}$  appears brighter where the cloud opacity is less. The dotted ellipse marks the approximate location where the Cassini spacecraft soon thereafter entered into the atmosphere, concluding the mission. *Image credits: NASA/JPL-Caltech/University of Arizona.*

#### 2.4. From High above the Atmosphere: Observations from Space Telescopes

While robotic spacecraft missions were venturing far into the outer Solar System, new discoveries were being made relatively closer to home with a series of space-borne telescopes. Though modest in size compared to ever-larger ground-based telescopes, these versatile observatories were unencumbered by telluric absorption, possessing a sensitivity only possible in the coldness of space.

The Infrared Space Observatory (ISO) was the first such space observatory to make great contributions in mid-infrared (and far-infrared) observations of the giant planets. Operated from 1995 to 1998, it was equipped with the Short Wave Spectrometer (SWS)—a scanning spectrometer sensing from 2.35 to 45.4  $\mu\text{m}$  with grating resolutions between 930 and 2450 ( $\lambda/\Delta\lambda$ ) and a higher resolution Fabry–Pérot mode (20,600–31,000) [264,265]. The combination of high spectral resolution and coverage led to the new detection of several molecules on all four giant planets [266,267], although Uranus and Neptune proved too faint to be observed below 7  $\mu\text{m}$ . Discoveries included the detection of water vapor in Saturn’s troposphere at 5  $\mu\text{m}$  [266]; detection of new hydrocarbons (e.g.,  $\text{CH}_3\text{C}_2\text{H}$  and  $\text{C}_4\text{H}_2$ ) in Saturn’s stratosphere [268]; detection of stratospheric  $\text{CO}_2$   $\nu_2$  bands on Saturn [268], Jupiter [269] and Neptune [48]; and the first detection of methyl ( $\text{CH}_3$ )—a molecule diagnostic of the height to which methane is mixed—in the stratospheres of Saturn [267] and Neptune [270]. Numerous discoveries were also made at longer wavelengths with the Long Wavelength Spectrometer (LWS). See Encrenaz et al. [271] for an excellent summary.

ISO was followed by the Spitzer Space Telescope, launched in 2003 [272]. Sensing from 5.2 to 38  $\mu\text{m}$  with low ( $R\sim 60\text{--}130$ ) and moderate ( $R\sim 600$ ) resolution spectroscopy, the Spitzer-Infrared Spectrograph (IRS) [273] observed Neptune on four occasions between 2004 and 2006 [274,275], and Uranus in 2004 [47] and 2007 [71,76], near the time of the planet’s equinox. With a primary mirror of 0.85 m, Spitzer, like ISO, was not able to spatially resolve the Ice Giants’ disks, but the observations nonetheless led to strong new constraints on the planets’ disk-averaged temperature structure [76,275,276] and chemistry [71]. The observations yielded the first detections of  $\text{C}_2\text{H}_6$  and possibly  $\text{CH}_3$  on Uranus and the first detections of methylacetylene ( $\text{C}_3\text{H}_4$ ) and diacetylene ( $\text{C}_4\text{H}_2$ ) in both Ice Giants [47,274].

Finally, it is worth noting that the new JWST promises to far surpass these previous mid-infrared space observatories and provide the definitive mid-infrared spectra of the giant planets. The Mid-Infrared Instrument (MIRI) [18] is capable of providing spatially resolved (integral field unit) spectra from 5 to 28  $\mu\text{m}$  with resolving powers from 1300 to 3700 ( $\lambda/\Delta\lambda$ ). The telescope successfully launched on 25 December 2021 and is expected to be operational for 20 years. All four giant planets will be observed in the first two years following launch. With superior sensitivity and spatial resolution, the results are anticipated to greatly advance our understanding of Uranus and Neptune, in particular.

### 2.5. Matured Mid-Infrared Observing from the Ground

Back on the ground, improvements in detectors, telescopes, and observing techniques advanced ground-based observations to a quality rivaling spacecraft observations (e.g., see Figures 4 and 8). The early contour maps of Jovian brightness temperatures from Palomar [129] gave way to raster-scanned maps from the NASA Infrared Telescope Facility (IRTF) in the 1980s and 1990s [50,277], followed by the first modern 2-D array detectors in the 1990s. A notable example of these early 2-D arrays was the Mid-Infrared Array Camera (MIRAC), a  $20 \times 64$ -pixel Si:As IBC detector sensitive to radiation from 2 to 26  $\mu\text{m}$ , made by a collaboration of the University of Arizona, Smithsonian Astrophysical Observatory, and Naval Research Laboratory [278,279].

By the mid-2000s, numerous mid-infrared instruments were in operation on 8-m class telescopes, including: Long Wavelength Spectrometer (LWS) [280] at Keck; Michelle [281] at Gemini North; The VLT Imager and Spectrometer for Mid-Infrared (VISIR) [282] at the Very Large Telescope (VLT); the Thermal-Region Camera Spectrograph (T-ReCS) at Gemini South, [283]; and the Cooled Mid-Infrared Camera and Spectrometer (COMICS) [284] at Subaru. Typically, planetary observations with these instruments have applied narrow-band filters covering spectral ranges between 8 and 13  $\mu\text{m}$  (the N-band) and 17 to 25  $\mu\text{m}$  (the Q-band), from which chemistry and/or temperatures were retrieved [33,51,53,65,74,77]. Additionally, such observations were frequently used to complement contemporaneous spacecraft observation, providing greater spatial or temporal coverage than possible from orbit [46,62,78,285].

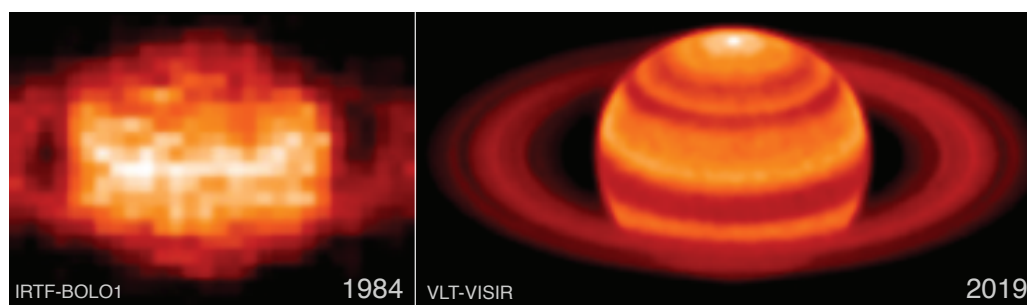


**Figure 8.** Improvements in mid-IR imaging, as illustrated by an early image of Saturn acquired with the IRTF-BOLO1 instrument in 1984 (left) compared to a recent image from the VLT-VISIR instrument in 2019 [65].

In terms of spectroscopy, a notable workhorse of ground-based remote sensing at mid-infrared wavelengths over the past two decades is the Texas Echelon Cross Echelle Spectrograph (TEXES) [286]. Capable of the spectral resolving power of 15,000 to 100,000 ( $\lambda/\Delta\lambda$ ) in windows between 5 and 25  $\mu\text{m}$ , TEXES has been used to great effect on IRTF and Gemini North to map chemistry and temperatures in Jupiter [287–292], Saturn [293–296], and to a lesser extent Uranus [297,298] and Neptune [70,74], with the exceptionally high spectral resolution needed to resolve fine lines. The resulting quality of retrieved maps of temperature, composition, and aerosols have been noted to even surpass previous spacecraft results for Jupiter [52].

Of the aforementioned mid-IR instruments, only VLT-VISIR and TEXES remain in operation as of 2023. Given the significant and unique information provided by mid-infrared ground-based observations, it can only be hoped that these continue to serve the community until the next generation of instruments is developed, at least.

Looking ahead, promising future mid-infrared instruments to include a mid-infrared imager and spectrometer called MIMIZUKU (Infrared Multi-field Imager for Gazing at the UnKnown Universe) [299], developed for the planned 6.5-m telescope of the University of Tokyo Atacama Observatory (TAO), currently under construction in the Chilean Atacama at a remarkable 5640-m altitude [300]. MIMIZUKU will cover a wavelength range of 2 to 38  $\mu\text{m}$  with a spectral resolution of  $\lambda/\Delta\lambda \sim 60\text{--}230$  and diffraction-limited (wavelength-dependent) angular resolution of 0.077–1.47 arcseconds. This spatial resolution is exceptional by current far-infrared standards, although it will not surpass the current leading resolution of the larger VLT across much of the mid-IR (e.g., TAO-MIMIZUKU's 0.7'' diffraction-limited resolution versus VLT-VISIR's 0.55'' resolution at 18  $\mu\text{m}$ ). The larger disks of Jupiter and Saturn will, therefore, be particularly well suited for MIMIZUKU, but all the Solar System's giant planets will benefit from its exceptionally broad spectral range, innovative technical design [301], and long-term monitoring capabilities in the years ahead. MIMIZUKU has already seen its first light, having been successfully tested on the Subaru Telescope in 2018 [302].

Looking even further ahead, the European Southern Observatory's planned 39.3-m Extremely Large Telescope (ELT) first-generation instruments will include the Mid-infrared ELT Imager and Spectrograph (METIS) [303]. METIS promises to provide diffraction-limited imaging and medium resolution slit-spectroscopy from 3 to 13  $\mu\text{m}$  (covering the M and N bands), as well as high resolution ( $R \sim 100,000$ ) integral field spectroscopy (IFU) from 2.9 to 5.3  $\mu\text{m}$  [304]. N-band imaging will be capable of an amazing 6.8-mas (milli-arcsecond) angular resolution over a  $13.5'' \times 13.5''$  field of view (FoV). The high spatial resolution and narrow FoV will make the instrument ideally suited for observing the small disks of Uranus and Neptune, while mosaicking or regional targeting will be required for Jupiter and Saturn. Likewise, the even narrower FoV of the M-band IFU ( $0.58'' \times 0.93''$ ) will be optimal for analyzing small-scale, 5- $\mu\text{m}$  atmospheric features with unprecedented resolution from the ground. With METIS' first light expected in 2028 [304], the complementary capabilities of

MIMIZUKU, VISIR, and METIS promise exciting advances in mid-infrared observations from the ground over the next decade.

### 3. What We Have Learned

From more than a century of mid-infrared remote sensing, a picture of the general atmospheric thermal structure and chemistry of the giant planets has emerged. For Jupiter and Saturn, the picture can appear quite intricate, with complex structure, unexplained variability, and puzzling correlations across different heights and hemispheres. By comparison, our pictures of Uranus and Neptune in 2023 are little more than rough sketches, lacking details but nonetheless challenging our understanding of temporal variation in the outer solar system.

Figures 9 and 10 compare the observed mid-infrared spectra of the giant planets derived from ISO-SWS [266] and Cassini-CIRS [141,237] for Jupiter and Saturn, and Spitzer-IRS [74,76,275] for Uranus and Neptune. Figure 11 compares ground-based images in three key mid-infrared windows.

#### 3.1. Chemistry and Temperature from Mid-IR Spectra

##### 3.1.1. 5–6 $\mu\text{m}$

From 5 to 6  $\mu\text{m}$ , scattered light and thermal emission contribute to the spectrum, modified by gaseous absorption. On Jupiter and Saturn,  $\text{NH}_3$  and  $\text{H}_2\text{O}$  are the primary absorbers [266,268,305]. Measurements of  $\text{NH}_3$ , have been used to provide insights into the accretion stage of the planets' formation histories. Analyses of the nitrogen ratios (at 5 to 6  $\mu\text{m}$  and  $\sim 10$ –11  $\mu\text{m}$ ) indicate identical values of these isotopic ratios for both Jupiter and Saturn, suggesting a similar history of primordial  $\text{N}_2$  accretions during the formation of each planet [245,287]. Likewise, the water abundance is important because oxygen is potentially telling of the carbon-to-oxygen (C/O) ratio, which is seen as diagnostic of the planet's formation history in the solar nebula [306–308]. The quest for Jupiter's and Saturn's deep water abundances has been a challenge since the mid-IR cannot sense well below the  $\text{H}_2\text{O}$  condensation level on either planet [309]. The Galileo probe (in situ) and Juno (microwave radiometer) have aimed to resolve this value for Jupiter, but uncertainties remain due to the inhomogeneous nature of Jupiter's atmosphere. A proper discussion is beyond the scope of this review, but see [88,89].

On Uranus and Neptune, this region of the spectrum was too weak to be observed by ISO-SWS, and even Spitzer-IRS spectra are in doubt [76,275,276]. The high opacity of Earth's atmosphere, particularly around 6  $\mu\text{m}$ , makes these observations impractical from the ground. Observations with JWST-MIRI should provide the first comprehensive examination of this spectral region.

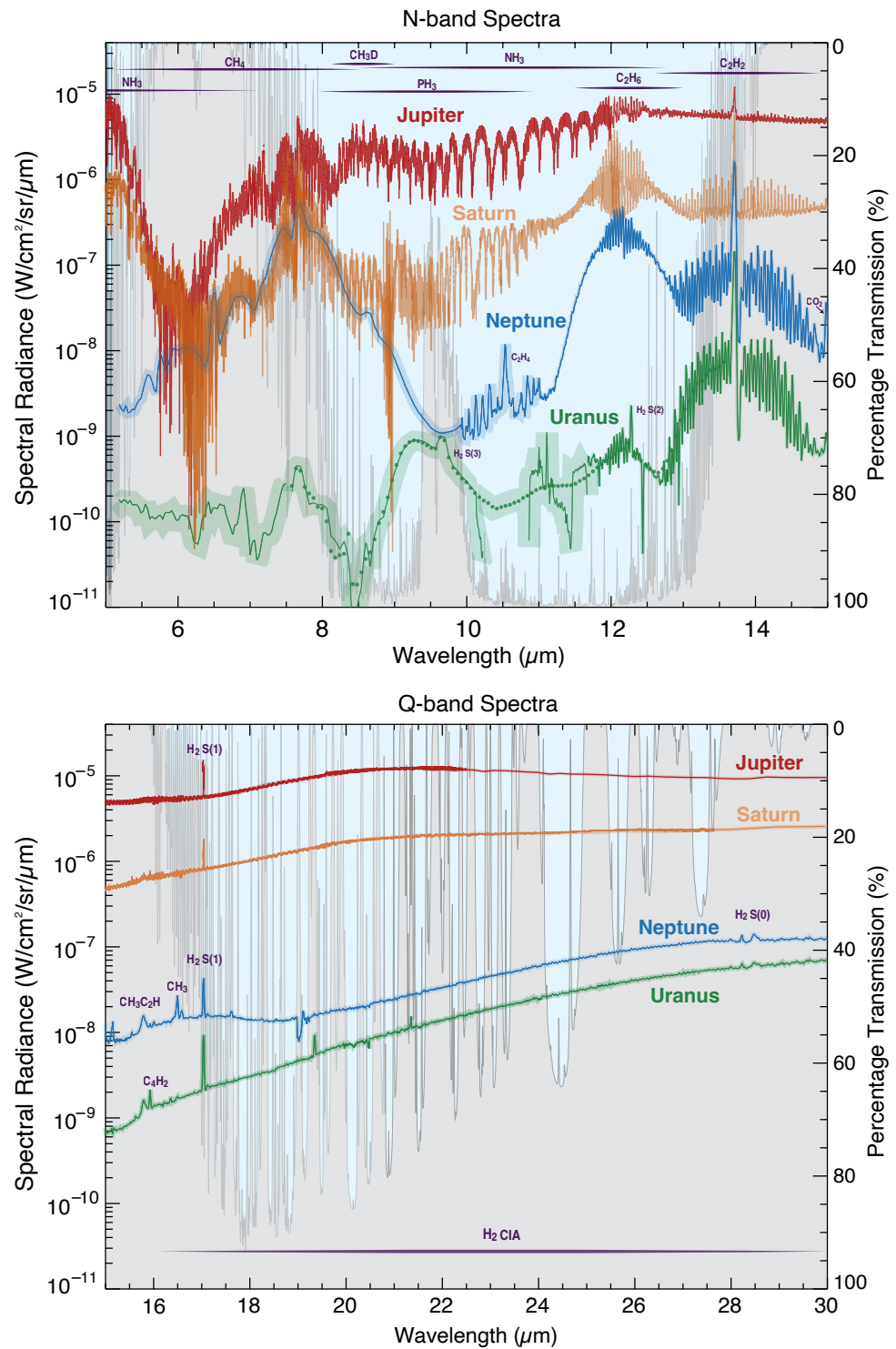


**Figure 9.** Observed mid-infrared spectra of giant planets in the N- and Q-bands (top and bottom panels, respectively). The spectra of Jupiter (red) and Saturn (orange) are from ISO-SWS [266] and Cassini-CIRS [141,237], while Uranus (green) and Neptune (blue) are disk-averaged radiances from Spitzer-IRS [74,76,275,276]. The rough uncertainty of the spectra (most evident for Uranus) is suggested by the faint transparent envelopes. Select emission features are indicated, and the wavelengths at which different gases broadly contribute to spectra are indicated by the labeled horizontal lines (purple). The atmospheric transmission is indicated by the blue–gray interface varying between 100% (full transmission) and 0% (total attenuation) from the top of the atmosphere down to a surface, as in Figure 2.

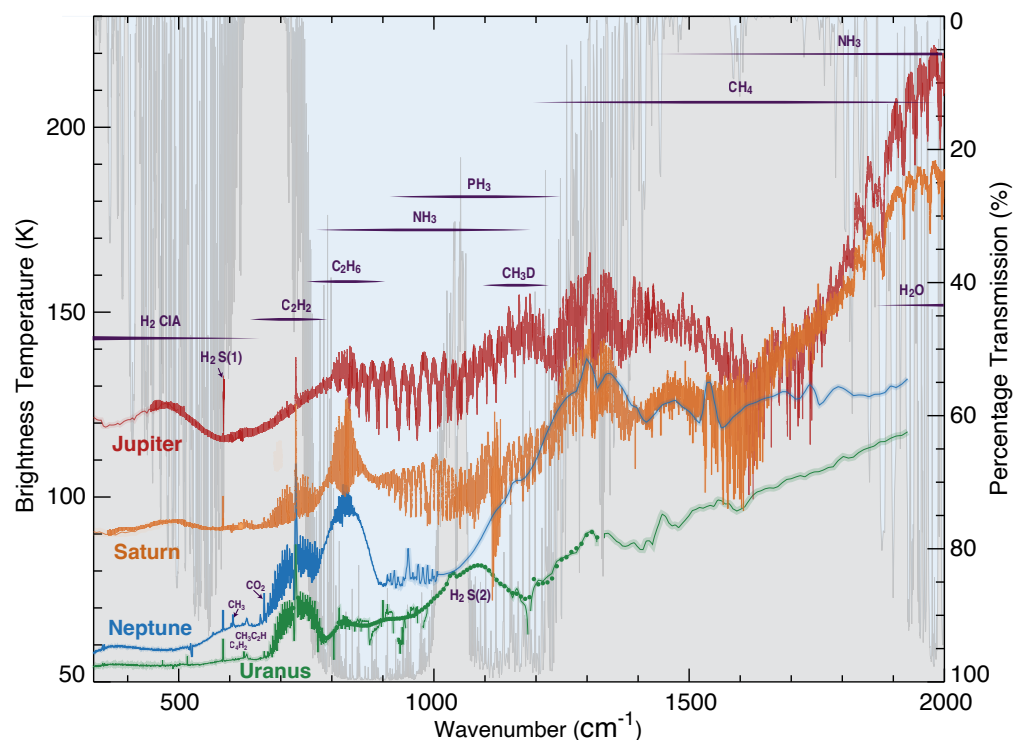


**Figure 10.** As in Figure 9, mid-infrared spectra of the giant planets, but now expressed in brightness temperature versus spectroscopic wavenumber.

### 3.1.2. 6–15 $\mu\text{m}$

From 6 to 15  $\mu\text{m}$ , the spectra are shaped by numerous strong emission and absorption features against a backdrop of the hydrogen-helium continuum emission from around the tropopause (roughly 100 mbar). On Jupiter and Saturn, absorption is produced by  $\text{NH}_3$ ,  $\text{PH}_3$ , and  $\text{H}_2\text{O}$ , while  $\text{CH}_3\text{D}$  (at  $\sim 9 \mu\text{m}$ ) and deeper  $\text{CH}_4$  absorption is found in the spectra of all four giant planets.

$\text{PH}_3$  is a disequilibrium species in the cold upper troposphere of Jupiter and Saturn, and its presence indicates vigorous vertical mixing on time scales less than that of chemical conversion [186,187,310]. It has yet to be detected on Uranus and Neptune [311]. The spatial distribution reveals latitudinal variation in mixing, as discussed in Section 3.2.

Combined measurements of  $\text{CH}_4$  and  $\text{CH}_3\text{D}$  have been used to estimate the D/H ratio of the planets, providing powerful clues as to their formation history in the solar nebula [312]. From theory, Jupiter and Saturn are expected to have D/H ratios consistent with the solar nebula, from which they derived most of their mass; Uranus and Neptune, however, should have higher D/H ratios if they formed from proportionately larger, deuterium-rich icy cores. Measurements have shown that D/H ratios on Uranus and Neptune are indeed a factor of a few larger than those of Jupiter and Saturn [69,71,244,275,276,313–315].

Nearly all the emission lines between 6 and 15  $\mu\text{m}$  are from stratospheric hydrocarbons, primarily  $\text{CH}_4$  (peaking at 7.7  $\mu\text{m}$ ),  $\text{C}_2\text{H}_6$  ( $\sim 12 \mu\text{m}$ ),  $\text{C}_2\text{H}_2$  (13 to 15  $\mu\text{m}$ ).  $\text{C}_2\text{H}_6$ ,  $\text{C}_2\text{H}_2$ , and other minor hydrocarbons (including methyl radicals ( $\text{CH}_3$ ), ethylene ( $\text{C}_2\text{H}_4$ ), methylacetylene ( $\text{CH}_3\text{C}_2\text{H}$ ) and diacetylene ( $\text{C}_4\text{H}_2$ )), are the result of photochemistry in the stratospheres of the giant planets [39]. Methane from the troposphere is mixed up into the stratosphere, where it is then broken down by ultraviolet radiation, prompting a chain of chemical reactions that result in a mélange of new hydrocarbons [37,39,164,165,316,317]. Estimates of the abundances of these hydrocarbons have been used to infer vertical mixing within the atmospheres and constrain seasonal-chemical models of their formation and destruction, e.g., [317]. Emission from  $\text{CH}_4$  has been used to infer stratospheric temperatures

on Jupiter and Saturn since it is considered uniformly well mixed in the warm atmospheres of the Gas Giants [171,248,293], whereas it cannot necessarily be used as a thermometer on Uranus and Neptune given that colder temperatures are expected to condense methane and alter the distribution [70]. However, hydrogen is well mixed in all these atmospheres, and the H<sub>2</sub> S(0), S(1), S(2), S(3), and S(4) quadrupole emissions contribute at observed radiances roughly 28, 17, 12, 9.7, 8 μm, respectively, to varying degrees. The S(2) and S(3) lines are weakly emitted from pressures near 1 μbar, and though they are detected in the Spitzer-IRS observations of Uranus [276], they are generally lost in the forest of ethane lines on the other planets. The H<sub>2</sub> (S1) and H<sub>2</sub> (S0), observed at longer wavelengths, are most easily measured and have proven the most useful for evaluating temperatures and ortho-para fractions, as discussed below.

The relatively intense spectra of Jupiter and Saturn at wavelengths beyond ~9 μm is telling of their relatively warmer upper-tropospheric temperatures, as inferred from the earliest observations of these planets [114]. This can be seen in typical temperature profiles derived from spectra (see Figure 3). Neptune, however, appears relatively bright at 7–8 μm—comparable to Saturn and indicative of Neptune’s surprisingly warm and methane-rich stratosphere. The large methane abundance is generally interpreted as evidence that Neptune has particularly strong vertical mixing, while Uranus is particularly stagnant [39,144,317]. The stratospheric methane mole-fraction ( $(1.15 \pm 0.10) \times 10^{-3}$  [69,318]) is greater than the expected value limited by the colder temperatures of the underlying tropopause (i.e., the cold-trapped minimum) [209,319,320]. Moist convection has been discussed as a possible explanation for the stratospheric methane enhancement [292,308,321]. Alternatively, another possible avenue for transferring methane from the troposphere to the stratosphere, despite the cold trap, was suggested following discoveries from thermal imaging. Images from ground-based imaging show the south pole of Neptune to be warmer at the tropopause and lower stratosphere than elsewhere on the planet [322]. Orton et al. [322] proposed that methane could potentially be seeping up from the troposphere at the warm pole before spreading to lower latitudes, avoiding cold-trapping. However, evidence of meridional transport or strong stratospheric methane gradients has yet to be found [70,74]. Furthermore, the excess methane and potential associated hydrocarbon hazes are still not enough to explain the high stratospheric temperatures of Neptune, which exceed that expected from radiative heating models [211,323–326]. Additional modeling is necessary to explain these observations.

The comparison of the planets’ spectra at 12–14 μm also reveals a striking difference between Uranus and the other giant planets. Uranus appears anomalously faint, with a conspicuous absence of C<sub>2</sub>H<sub>6</sub> emission. Modeling of the stratospheric photochemistry has suggested that this is a consequence of Uranus’ apparently weak vertical mixing, which results in meager lower-stratospheric methane abundances ( $1.6 \times 10^{-5}$ ) and a lower-altitude homopause ( $7 \times 10^{-5}$  bars). This limits methane and hydrocarbon photochemistry to relatively higher pressures, where the dominant hydrocarbon reactions and loss rates differ. With less CH<sub>4</sub> in the stratosphere, C<sub>2</sub>H<sub>6</sub> is also less shielded and more easily photolyzed. This results in relatively lower ethane abundances ( $1.3 \times 10^{-7}$  at 0.2 mbar) [71] compared to Jupiter ( $2.08 \times 10^{-5}$  [327], Saturn ( $9 \times 10^{-6}$  [251]), and Neptune ( $8.5 \times 10^{-7}$  [69]).

### 3.1.3. 15–30 μm

Finally, from 15 to 30 μm, the spectrum is dominated by the hydrogen-helium continuum emission from the upper troposphere and lower stratosphere. At these wavelengths, the differences in radiances between the planets clearly express the relative temperatures around the tropopause (~40–200 mbar) (see Figure 3). Uranus, with its apparent weak internal flux and vertical mixing of solar-absorbing methane, is overall coldest at these pressures, despite being nearer to the Sun than Neptune. Several small emission features can also be seen, including CO<sub>2</sub> on both Jupiter [48,328] and Saturn [268] at 14.98 μm; CH<sub>3</sub>C<sub>2</sub>H (methylacetylene) and C<sub>4</sub>H<sub>2</sub> (diacetylene) at 15.80 and 15.92 μm, respectively, on all giant planets [71,76,268,275,276,329]; likewise CH<sub>3</sub> has been detected at 16.5 μm, although only tentatively for Uranus [71,267,276]. Retrieved CH<sub>3</sub> on Jupiter and Saturn

have been shown to be inconsistent with predicted values based on theoretical eddy diffusivity and  $\text{CH}_3$  recombination rates [267]. Subsequent analysis of TEXES spectra also revealed a  $3 \times$  greater abundance of  $\text{CH}_3$  in Jupiter's polar regions [292] than predicted by photochemical models [330]. These inconsistencies suggest a need for additional sources of  $\text{CH}_3$  production or uncertainties in chemical rates [292], and the topic remains an area of active research.

Standing out among the emission features are the  $\text{H}_2$  (S1) and  $\text{H}_2$  (S0) hydrogen quadrupoles, observed at roughly 17 and 28  $\mu\text{m}$ . These lines are unambiguously sensitive to the lower stratospheric temperatures within a larger continuum that is sensitive to the *ortho* and *para* fractions [211–213]. Retrievals exploiting the  $\text{H}_2$  S(1) quadrupole have been particularly important for the Ice Giants, where methane emission cannot be used as an unambiguous proxy for stratospheric temperature owing to its potentially variable distribution. Several studies have used the  $\text{H}_2$  (S1) line to determine lower stratospheric temperatures and, combined with the  $\text{H}_2$  and He continuum emission, derive vertical temperature profiles [70,74,76,276]. Notably, the  $\text{H}_2$  (S1) has also been used to confirm that Neptune's enhanced polar stratospheric emission and its changes in time are due primarily to variations in temperatures, as discussed in the next sections [74].

### 3.2. Structure and Dynamics from Spatially Resolved Mid-IR Spectra and Imaging

As current exoplanetary investigations demonstrate, a rich amount of atmospheric data can be inferred from an unresolved target [331,332]. However, constraining many of the processes shaping a three-dimensional atmosphere—often in unanticipated ways—requires observations to characterize the spatial structure.

The Solar System planets vary significantly in observed structure at mid-infrared wavelengths, as can be seen in the representative examples of mid-infrared images shown in Figure 11. Filtered images are shown in three typical mid-infrared passbands for each planet. Each of these filters senses radiation from a different wavelength and is thus associated with different molecular transitions and pressure levels in the atmosphere. The Q-band is represented by the images with filtered bandpasses around 18–19  $\mu\text{m}$ . These sense thermal emission from the upper troposphere to the lower stratosphere that results from the collision-induced hydrogen-helium continuum. The 12–13- $\mu\text{m}$  filters are centered on wavelengths dominated by ethane and/or acetylene emission lines originating from the stratospheres. The 7.9- $\mu\text{m}$  filters are sensing emissions from stratospheric methane.

In general, the measured mid-infrared radiances are dependent on the abundance of the emitting gas as well as the temperature of the gas. In all cases, hydrogen and helium are assumed to be uniformly well mixed throughout the atmosphere below the homopause, and so the observed spatial structure can be explained by spatially varying temperatures. On Jupiter and Saturn, methane is likewise considered well mixed, and thus the 7.9- $\mu\text{m}$  observations are again indicative of temperatures structure [53,54], but at lower pressures. However, on Uranus and Neptune, it is cold enough for methane to condense in the troposphere, and therefore methane cannot necessarily be assumed to be uniformly well mixed [70,74]. Similarly, stratospheric ethane and acetylene are disequilibrium species, with sources and sinks dependent on photochemistry and temperatures, and so these hydrocarbons are not expected to be uniformly well mixed in pressure or latitude on any of the planets. For these potentially variable gases, the cause of the structure is inherently ambiguous, and interpretation of the radiances requires independent knowledge of the temperatures or assumptions regarding the gaseous distributions. Hence, temperatures derived from thermal observations, particularly from imaging and low-resolution spectra, are inherently subject to large degeneracies with chemical composition (and sometimes cloud opacity), resulting in potentially large uncertainties.

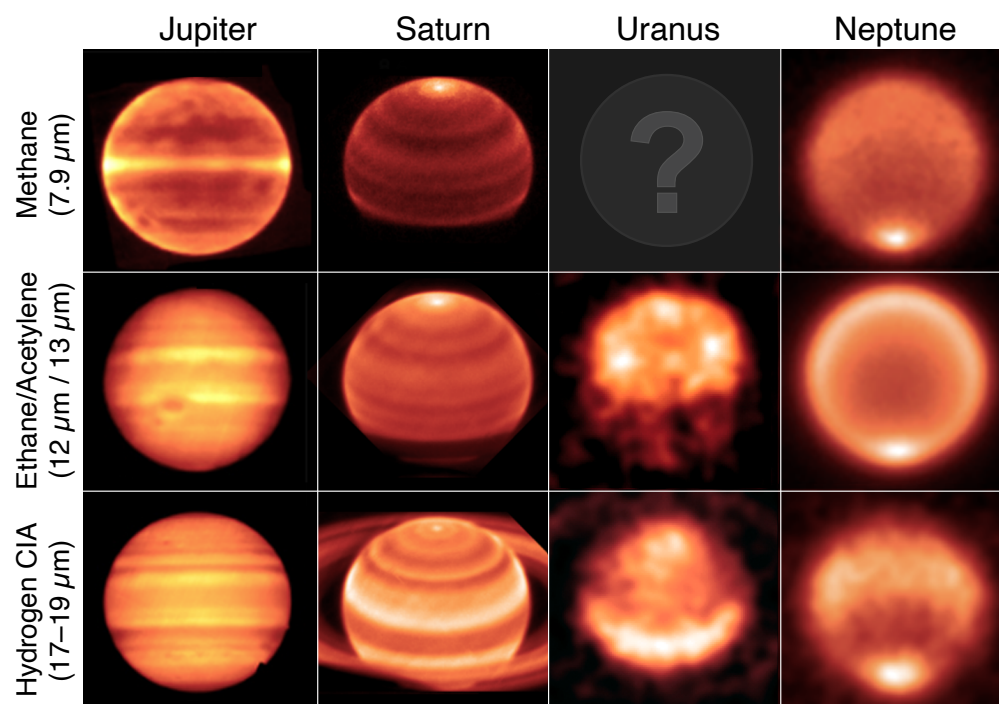


**Figure 11.** Mid-infrared images of the giant planets from ground-based observatories at three different wavelengths regions, each primarily sensitive to different molecules and pressures: stratospheric methane (centered at  $\sim 7.9 \mu\text{m}$ ); stratospheric ethane ( $\sim 12.2 \mu\text{m}$ , relevant to Jupiter, Saturn, and Neptune) and acetylene ( $\sim 13 \mu\text{m}$ , relevant to Uranus); and tropospheric hydrogen ( $\sim 17\text{--}19 \mu\text{m}$ ). Images have been rotated so that north is up in all cases. Note that Uranus appears remarkably different in structure in its stratospheric emission compared to other planets. Furthermore, note that Uranus images are of starkly poorer quality owing to Uranus' weaker emission. Images of Uranus at  $7.9\text{-}\mu\text{m}$  do not exist in the literature, given poorer telluric transmission and Uranus' particularly weak emission at these wavelengths. Images are from the following sources: Jupiter from IRTF-MIRSI in 2010 [333]; Saturn from VLT-VISIR in 2016 [65]; Uranus from VLT-VISIR in 2018 [33]; Neptune from VLT-VISIR, averaged from images dating between 2008 and 2018 [74].

### 3.2.1. Spatial Structure of Jupiter and Saturn

Jupiter and Saturn show distinct zonal banding across the mid-infrared, indicative of a complex temperature structure associated with belt-zone dynamics [49,197,334,335]. Temperature structures retrieved from spatially resolved spectra are shown in Figure 12. Regions that appear brighter in thermal infrared emission (see Figures 4 and 11) are warmer with thinner clouds, whereas darker areas are colder with thicker clouds. The mechanism behind these regional temperature differences has been interpreted as evidence of adiabatic warming and cooling associated with sinking and rising currents of gas, respectively, [44,173,211,215,334]. However, it has been argued that the temperature anomalies can be sustained dynamically given cyclonic/anticyclonic zonal shear and the strong vertical stability of the tropopause [335]. In this interpretation, pressure differences between cyclonic and anticyclonic shear regions lead to temperature differences, given constraints on the column thickness imposed by the static stability of the tropopause. However, upwelling and downwelling may still be necessary to explain evidence of chemical disequilibrium, including that of ortho-para hydrogen, which suggests equatorial upwelling on Jupiter and Saturn [46,52,214,336,337].

The meridional temperature gradients imply vertical wind shear by the geostrophic thermal wind balance, and the regions of maximum gradients appear well correlated with the latitudes of localized peaks in the zonal winds (i.e., zonal jets) detected by cloud tracking [338–342]. The vertical motions and shears implied by the temperature field must

also be balanced by meridional winds, and Cassini-CIRS observations evidence of this meridional transport in chemical tracers (e.g.,  $C_2H_2$ ,  $C_2H_6$ ,  $C_3H_8$ ) on Saturn [60,254,293] and Jupiter [343,344]. Distributions of ammonia [240] on Jupiter and phosphine [242] on both Jupiter and Saturn also show signs of dynamical motions, with maximum abundances in the cool equatorial zone and reduced abundances in the adjacent warm belts. This is consistent with the picture suggested by the temperature field, with strong uplift in the equatorial zone and descent in the neighboring belts at the top of the troposphere. As these results demonstrate, the mid-infrared measurements provide an independent diagnostic of the winds and dynamics, beyond which visual imaging of aerosol scattering alone can provide.

This full picture of the gas giant circulations becomes more complicated when one also considers the distribution of storms, deep ammonia, and microwave radiances—all of which potentially point towards deeper, vertically coincident, but directionally opposite circulation cells (“stacked” circulation cells) on Jupiter [345–349]. A discussion of this circulation is beyond the scope of this review, but see Fletcher et al. [334] for a comprehensive review.

Saturn also displays enhanced emission at its poles, which measures 4–7 K warmer than the surrounding latitudes [78,350]. As can be seen in the consistency across three filtered images in Figure 11, the feature extends from the upper troposphere into the stratosphere. The enhanced emission implies downwelling and adiabatic warming, consistent with the local reduction in phosphine [242]. Observations over time have shown that this is a seasonally varying feature, as discussed in Section 3.3.2.

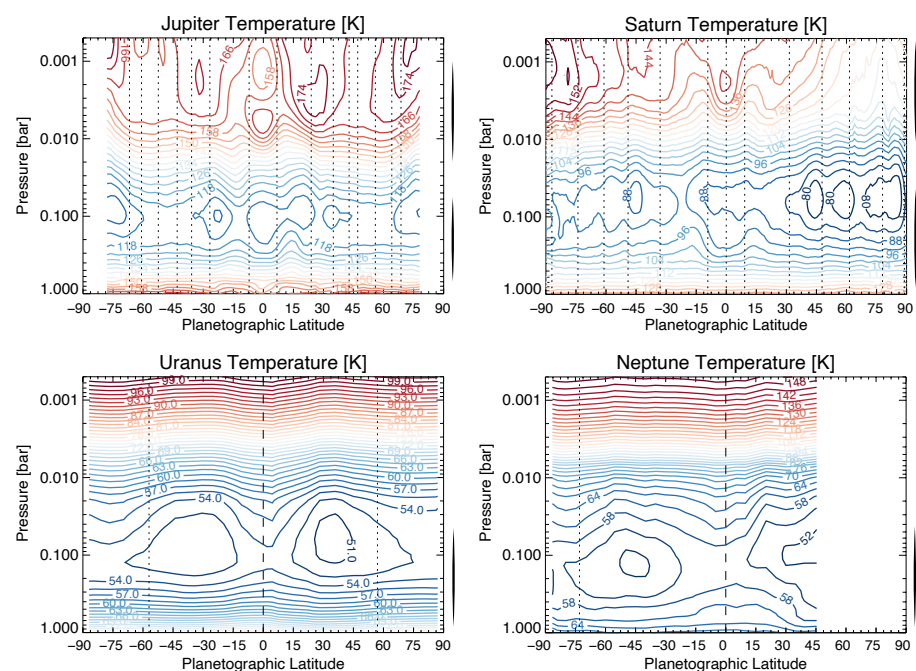


**Figure 12.** Contours depicting retrieved temperatures versus latitude and pressure for each of giant planets, reproduced from Fletcher et al. [334]. Colors suggest the transition from warmer (redder) to colder (bluer) temperatures. Temperature data for Jupiter are from the Cassini-CIRS Jupiter flyby in 2000 [242]. Data for Saturn are from Cassini-CIRS while in orbit around the planet, dating between 2006 and 2010 [351]. Temperature data from Uranus [77,352] and Neptune [72] are from the Voyager 2 flybys in 1986 and 1989, respectively. The vertical lines to the right of each plot indicate the pressures at which temperatures are constrained by the observations; outside these pressure ranges, temperatures simply relax to an assumed starting profile [334]. Vertical dotted and dashed lines indicate the position of prograde and retrograde zonal jets, respectively, (from [338,339,353]). Zonal winds and temperatures are in geostrophic balance.

### 3.2.2. Uranus and Neptune

In the case of Uranus and Neptune, the thermal structures appear, at first glance, less complex. On both planets, the equators and poles appear relatively more radiant than do the mid-latitudes in the Q-band images (18–19- $\mu\text{m}$ ) [33,72,74,77,322,354–356]. This is consistent with tropopause pressures (40–200 mbar) being colder (roughly 3–6 K) compared to the warmer equator and poles [33,72,74,77,210,211,352]. The stratospheres of the Ice Giants, however, appear significantly different in structure compared to each other and their tropospheres.

Neptune possesses signs of faint banding at 7.9  $\mu\text{m}$  and strong limb-brightening at 12  $\mu\text{m}$ , but only slightly enhanced equatorial brightening [74,292]. The limb brightening can be explained by temperature and ethane profiles that increase with height at the range of pressures sensed [72,74,317], in contrast to the decreasing profile. However, the banding, if truly present, appears somewhat more complicated than the temperature structure below. With some squinting, one may even argue that 7.9  $\mu\text{m}$  images of Neptune appear vaguely more similar to those of Saturn, with its strong polar vortex and banding, only degraded by poorer spatial resolution. With slightly weaker radiances at mid-latitudes compared to the equator and pole, it is possible that we are simply seeing an extension of the upper tropospheric circulation imprinted upon a more complex stratospheric temperature and/or chemical structure, but this cannot be conclusively determined with existing data [73,74].

Observations of Neptune's hydrogen quadrupole emission (17.03- $\mu\text{m}$   $\text{H}_2$  S(1)) suggest that Neptune's stratospheric emission structure is primarily owing to latitudinal gradients in its temperature field [74]. Assuming that the atmospheric composition is uniform with latitude, retrievals of atmospheric temperatures reveal a strong meridional gradient, with a 30 K difference between the cool mid-latitudes and the warm polar vortex at 0.5 mbar in 2020 (see Figure 13). As discussed in Section 3.3.4, this temperature structure appears variable in time.

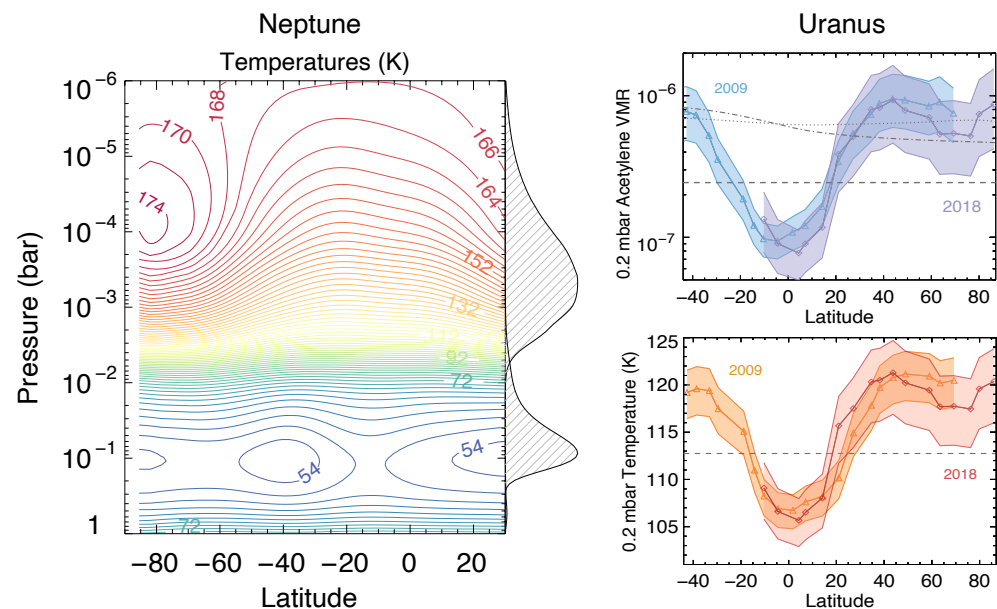


**Figure 13.** Retrieved stratospheric properties from ground-based images of the Ice Giants. Left: Neptune's temperature structure, retrieved from 2020 VLT-VISIR imaging data [74]. Temperatures are indicated by the colored contours at 2 K intervals. The heights constrained by the data are suggested by the vertical curves on the right, with maxima contributions peaking near 100 and 0.5. A warm polar vortex is evident at south polar (planetocentric) latitudes. Right: Meridional gradients in  $\text{C}_2\text{H}_2$  (top) and temperature (bottom), consistent with Uranus' observed stratospheric radiances (see Figure 14). Current data cannot differentiate between the two potential extreme solutions, given the ambiguous nature of the stratospheric emission [33].

Finally, and most peculiar of all, Uranus' stratosphere appears completely different from all other giant planets. Uranus' lower stratosphere is very cold and relatively dry [39,71,76,317], and as such, no methane-sensing images ( $7.9\ \mu\text{m}$ ) currently exist (see Figure 11). However, a few images at  $13\ \mu\text{m}$ , sensitive to stratospheric  $\text{C}_2\text{H}_2$ , do exist, and they show excess radiance at high latitudes in the northern and southern hemispheres [33,298,357] (see Figure 14). From existing data, it cannot be determined whether these greater high-latitude radiances are due to warmer temperatures or an enhancement in  $\text{C}_2\text{H}_2$  (see Figure 13). Additionally, the peak latitude of this radiance cannot be strongly constrained given the low signal-to-noise ratio (SNR) of the data. It is tentatively placed at  $40^\circ$  latitude, but it may remain constant poleward of this value, depending on the amount of limb-brightening present [33]. The determination of the distribution is significant. A peak at  $40^\circ$  would coincide with the latitudes of temperature minima and assumed maxima upwelling in the upper troposphere, implying a dynamical connection from below. This could be in the form of a vertically coincident but opposite circulation cell, or, in contrast, an extension of the existing upper-tropospheric circulation simply supplying excess hydrocarbons to the local stratosphere. However, a uniform distribution north of  $40^\circ$  would require a completely different explanation. The latter would imply either a separate and somewhat independent circulation, or simply that a completely different mechanism (e.g., annual radiative heating, photochemistry, or breaking waves) is shaping the stratospheric radiance [33]. In any case, the lack of data is limiting our ability to understand the stratospheric dynamics and/or chemistry of Uranus. Fortunately, JWST should soon provide the data necessary to make considerable advances in our understanding of Uranus' stratosphere.

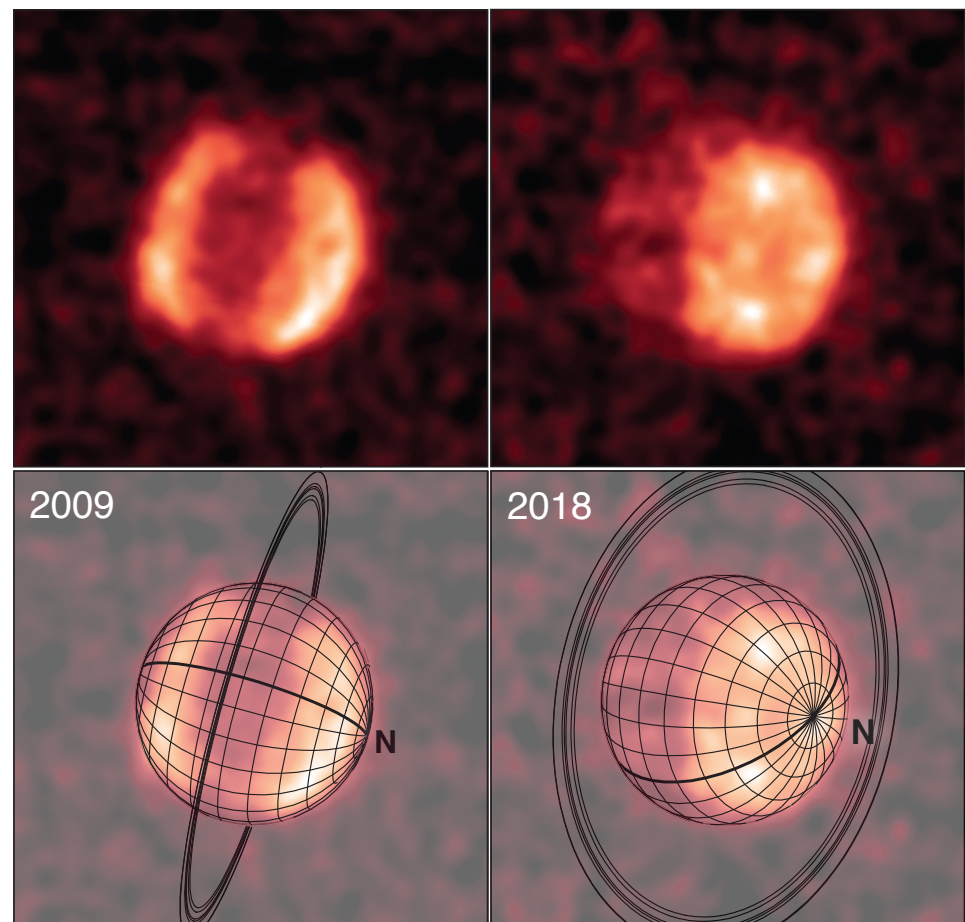


**Figure 14.** Uranus' stratosphere at  $13\ \mu\text{m}$ , as seen from VLT-VISIR in 2009 (left) and 2018 (right). Differences in the geometry of the observations are illustrated in the bottom panels. The cause and precise spatial distribution of the enhanced radiance at high latitudes is unclear [33].

### 3.3. Temporal Variability

The atmospheres of the giant planets exhibit significant variation at visible and near-infrared wavelengths, where we observe sunlight scattered and/or absorbed by gases, clouds, and hazes [342,358–372] (see Simon et al. [373] for a review). Corresponding variations in atmospheric temperatures and chemistry may naturally be expected. With decades of mid-infrared observations now available, investigations of temporal variability at thermal wavelengths have revealed intriguing findings in recent years.

In general, many potential sources of temporal variability exist in planetary atmospheres, acting over a wide range of timescales [374]. We can divide these sources into two basic groups, categorized as either internal or external mechanisms. Internal mechanisms include meteorological phenomena and generally stochastic processes within the atmosphere that are poorly understood in the giant planets, whereas external mechanisms act upon the atmosphere and may be considered more deterministic (impactors may be considered a notably stochastic exception). The latter category includes solar energy incident upon the atmosphere, the effects of which can be assessed with seasonal models [37,211,317,375,376].

For planets with significant axial tilts (the angle between the direction of the positive pole and the normal to the orbital plane), the daily mean insolation (per unit area) varies seasonally across the disk, with the greatest variation at higher latitudes. The axial tilts are  $3.12^\circ$ ,  $26.73^\circ$ ,  $97.77^\circ$ , and  $28.33^\circ$ , for Jupiter, Saturn, Uranus, and Neptune, respectively, (although, note that this differs from the definition adopted by the International Astronomical Union (IAU), which defines Uranus' north pole as the one that lies on the north side of the Solar System's invariable plane, thus placing Uranus' tilt at  $82.23^\circ$  [377,378]). The period of this cyclic, seasonal variation is determined by the tropical orbital period of the planet (the period of time that the Sun takes to return to the same position in the sky as viewed from the planet), and this period is 11.86, 29.42, 83.75, and 163.72 years for Jupiter, Saturn, Uranus, and Neptune, respectively, [123,377]. With a  $98^\circ$  axial tilt and 84-year orbit, Uranus arguably serves as the most extreme example of variable seasonal forcing, with much of the planet experiencing decades of uninterrupted summer daylight and winter darkness [206,317]. Although solar fluxes are weak in the outer Solar System, modeling suggests seasonal variation in temperatures and chemistry are likely [37,317], and, in the case of Saturn, well documented by observations [379] (see Section 3.3.2).

In addition to these larger changes in seasonal forcing, the Sun is intrinsically variable over the course of a roughly 11-year solar cycle. While the total solar irradiance differs by little more than 0.1% over a typical solar cycle [380], variation in far-ultraviolet (e.g., 121.57 nm Lyman- $\alpha$  irradiance) can exceed 40%. Such high-energy photons are the main drivers behind methane photochemistry, and so modulation in the UV flux can potentially produce observable variation in photochemistry if the reaction timescales are sufficiently short [37].

The expected extent of the seasonal variation will depend on the change in solar forcing and the capacity of the atmosphere to respond to that change. Characteristic timescales for the atmospheric responses can be calculated from radiative and chemical models, and by comparing these timescales to the orbital periods, the potential for seasonal changes can be assessed. Figure 15 illustrates the results of two separate studies, in which radiative time constants were calculated by perturbing the temperature profile and calculating the resultant change in cooling rates [211,326]. While significant differences exist between the results (likely owing to the use of updated gaseous absorption coefficients [381] and more rigorous radiative-transfer modeling by Li et al. [326]), both analyses suggest that Uranus is an outlier, with radiative time constants far longer than the orbital/seasonal timescales, as discussed in Section 3.3.3. However, variation in the stratospheric temperatures of the other giant planets seems likely according to the more recent analysis, and, indeed, this potential appears consistent with observed variability.

Analyses of the characteristic timescales of chemical reactions [36,37,317] and dynamical transport [173,211,324,336] have similarly been explored to assess the potential for variability. Uranus again appears relatively sluggish compared to the other plan-

ets, with expectations for less seasonal photochemical variation [317] and exceedingly long dynamical time constants (estimated at 700 years compared to  $\leq 200$  for the others) [173]. Chemical variation has been detected in the atmospheres of Jupiter and Saturn [63,243,285,290,382,383], but Uranus and Neptune remain poorly constrained given their long seasonal timescales. Likewise, dynamical timescales for all the planets remain highly theoretical and uncertain owing to the obvious challenges of observationally constraining such parameters.

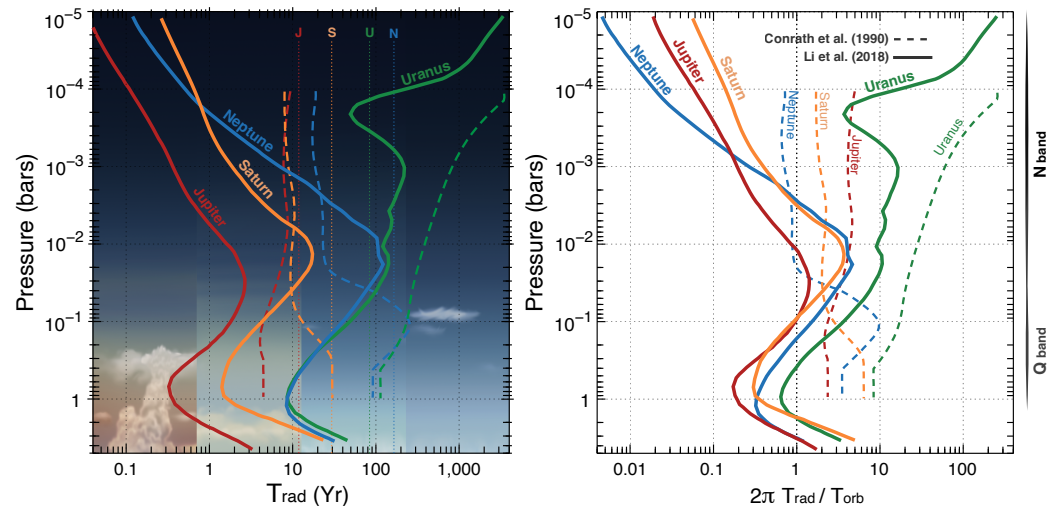


**Figure 15.** Theoretical radiative time constants for the giant planets. Plots show these characteristic timescales for each planet over a range of pressures, as derived in two separate studies—dashed lines are Conrath et al. [211] while solid lines are from Li et al. [326]. The left plot presents the radiative time constant in years, with the orbital periods of each planet indicated by the vertical dotted lines (labeled “J” for Jupiter, “S” for Saturn, etc.). The right plot expresses the values in terms of a ratio parameter (of a form akin to the resonance behavior of an underdamped harmonic oscillator [211]), for which values of order unity or smaller indicate the potential for stronger seasonal responses. The approximate pressures sensed by the N and Q bands are suggested at the far right. Note that Uranus has the longest radiative time constants throughout the stratosphere.

### 3.3.1. Jupiter Variability

Multi-wavelength imaging of Jupiter over the past nearly 40 years has revealed surprisingly complex variability in Jupiter’s atmosphere, (e.g., [333]). Data have revealed gradual changes in low latitude temperatures, with little seasonal or short-term variation [384]. Emission at 5- $\mu\text{m}$  has been used to reveal significant variability in the cloud opacity [54,289,385], while stratospheric temperatures, appear more variable and complicated on shorter timescales [50,386].

Observations of Jupiter’s stratospheric temperatures via methane at 7.9  $\mu\text{m}$  have been used to infer variability between 1980 and 2011 [387] (see Figure 16). This investigation revealed significantly different periods of oscillation (the quasi-quadrennial oscillation), with a 5.7-year period between 1980 and 1990 and a 3.9-year period between 1996 and 2006. Planetary-scale disturbances in 1992 and 2007 disrupted the predicted quasi-quadrennial oscillation pattern, suggesting that these oscillations are related to vertically propagating waves generated by meteorological sources below [387].

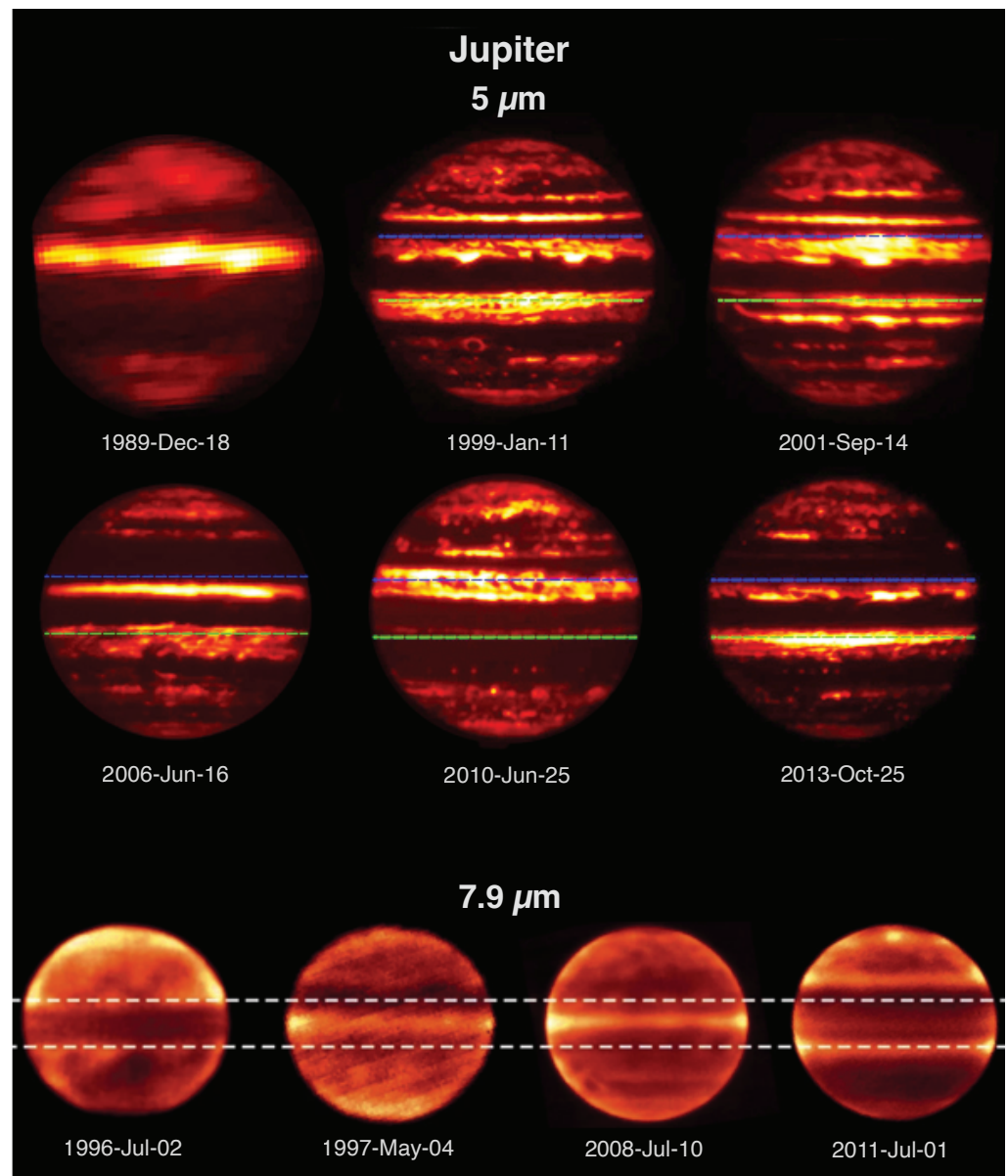


**Figure 16.** Sequences of mid-infrared images of Jupiter at 5  $\mu\text{m}$  (top) and 7.9  $\mu\text{m}$  (bottom) showing changes over time, adapted from Antuñano et al. [385] and Antuñano et al. [387]. Variation at 5  $\mu\text{m}$  suggests changes in tropospheric temperature and cloud opacity, with large temporal variability mainly at the equatorial and tropical latitudes and less temporal variability at mid-latitudes [385]. Dashed blue and green lines mark 16° N and 10° S planetocentric latitudes, respectively. Emission at 7.9  $\mu\text{m}$  sense stratospheric temperatures (via methane emission), revealing roughly periodic variation associated with the quasi-quadrennial oscillation [387]. 5- $\mu\text{m}$  images are from various instruments on the IRTF, including BOLO-1 (1984) [384], NSFCam (1999, 2001) [388], NSFCam2 (2006) [51], and SpeX (2010, 2013). 7.9- $\mu\text{m}$  images are from IRTF-MIRLIN (1996, 1997) and IRTF-MIRSI (2008, 2011).

Similar studies have revealed surprising apparent correlations (and anti-correlations) between different altitudes and locations. Equatorial temperature variations in the upper troposphere appear anti-correlated with higher altitudes, in a manner that suggests stratospheric dynamics may also influence the upper tropospheric temperatures below. Intriguingly, anti-correlations in temperatures have been detected for conjugate latitudes in opposite hemispheres [333,387,389].

Though the sources of such oscillations are not definitively known, some are thought to be associated with stratospheric winds and temperature oscillations, analogous to Earth's

quasi-biennial oscillation [50,236,390]. Theories suggest wave or eddy-driven meridional winds likely play an important role in modulating the temperatures and winds in the upper troposphere and stratosphere on seasonal and shorter timescales [391], and analyses of the thermal variability could potentially be used to estimate variation in the mechanical forcing [236].

### 3.3.2. Saturn Variability

Unlike Jupiter, Saturn has a significant axial tilt ( $26.73^\circ$ ), as illustrated by the changing views from Earth seen in Figure 17. The resulting seasonal variation in sunlight over a Saturnian year (29.4 Earth years) dominates Saturn's temporal variability in the mid-infrared. The Cassini-Huygens mission orbited Saturn for 13 years—enough to gain unprecedented detail of how the planet changed over the course of nearly two seasons. Cassini-CIRS observed Saturn's northern mid-latitude stratosphere warming by 6–10 K as this region emerged from ring-shadow in spring, while the southern mid-latitudes cooled by 4–6 K [249] (see Figure 18). The tropospheric temperatures also changed, but to a lesser degree, consistent with theoretical expectations of larger thermal inertia and longer radiative time constants. The fall and winter hemispheres also saw significant depletion in acetylene, consistent with seasonal photochemical modeling [37,392].

As part of Saturn's seasonal cycle, its polar stratosphere sees the development of a warm circumpolar vortex that peaks in the summer and dissipates in the winter. Cassini-CIRS observed the dissipation of Saturn's southern polar vortex in southern mid-autumn (2012) [78,379], followed by the eventual formation of the northern polar vortex in late northern spring (2015) [78]. The northern feature was associated with warmer temperatures poleward of  $\sim 75^\circ$  planetographic latitude. Interestingly, this feature exhibited a hexagonal boundary, echoing the hexagonal Rossby wave made visible in the clouds far below. This suggests a dynamical link between the features separated by 300 km in height [78]. A comprehensive review of Saturn's seasonal changes during the Cassini era can be found in Fletcher et al. [63].

A recent multi-decadal study of ground-based mid-infrared imaging similarly found seasonal temperature changes of  $\sim 30$  K in the stratosphere and  $\sim 10$  K in the upper troposphere, consistent with Cassini observations and predictions from radiative climate models [65]. The most recent observations from VLT-VISIR show warming is continuing at the northern summer polar stratosphere. However, comparison of  $\sim 7.9$   $\mu\text{m}$ -imaging revealed evidence of inter-annual variations at equatorial latitudes. Variations on these timescales are inconsistent with the strictly semi-annual 15-year equatorial stratospheric oscillation [250,393], suggesting the oscillation's period is either intrinsically variable and/or subject to disruption by storms or other meteorological phenomenon.

Aside from seasonal phenomena, mid-infrared observations have also notably detected warm stratospheric features associated with an immense northern-hemisphere storm that appeared in December 2010. The storm was observed to produce enormous changes in stratospheric temperatures and chemistry, warming the localized region by 80 K compared with its surroundings at 2 mbar [285]. The stratospheric warm "beacons" eventually evolved into a stratospheric anticyclonic vortex in 2011 [62,285] (see Figure 17). Cassini-CIRS observations were compared with chemical models to explain the mid-infrared changes, and it was found that elevated temperatures alone could not explain the enhanced thermal emission from ethane and acetylene. Downwelling winds, transporting hydrocarbons to higher pressures, were also needed to reproduce the CIRS observations.

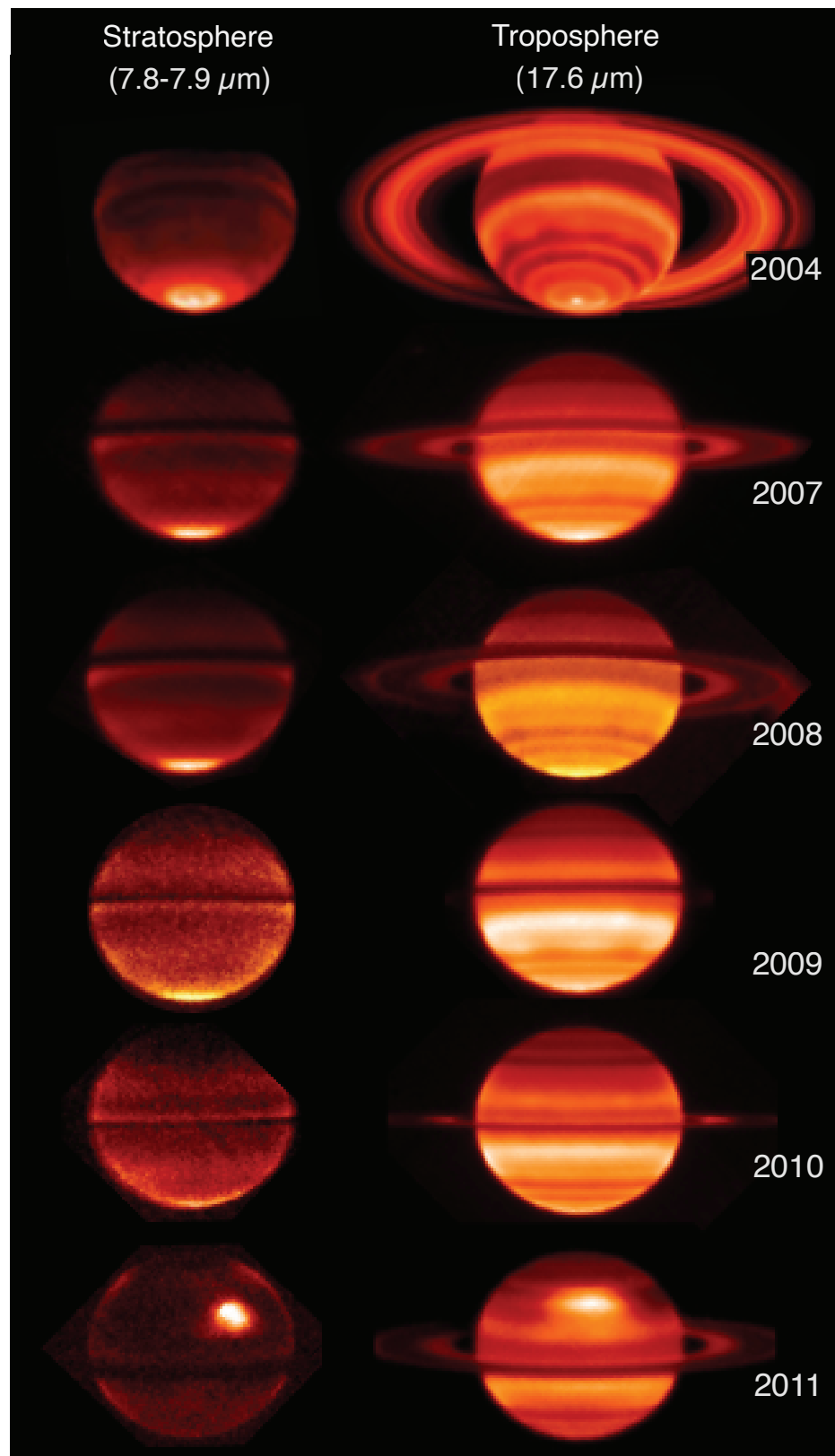


**Figure 17.** Saturn images showing changes between 2004 and 2012, adapted from [65]. Images sense stratospheric temperatures via methane emission at 7.8  $\mu\text{m}$  (left) and tropospheric temperatures via collision-induced hydrogen at 17.6  $\mu\text{m}$  (right). Images are from Keck-LWS (2004) [394], Subaru-COMICS (2007), and VLT-VISIR (2008-2012). Note the prominent warm spot associated with a remarkable storm in the northern hemisphere in 2011 [62,395].

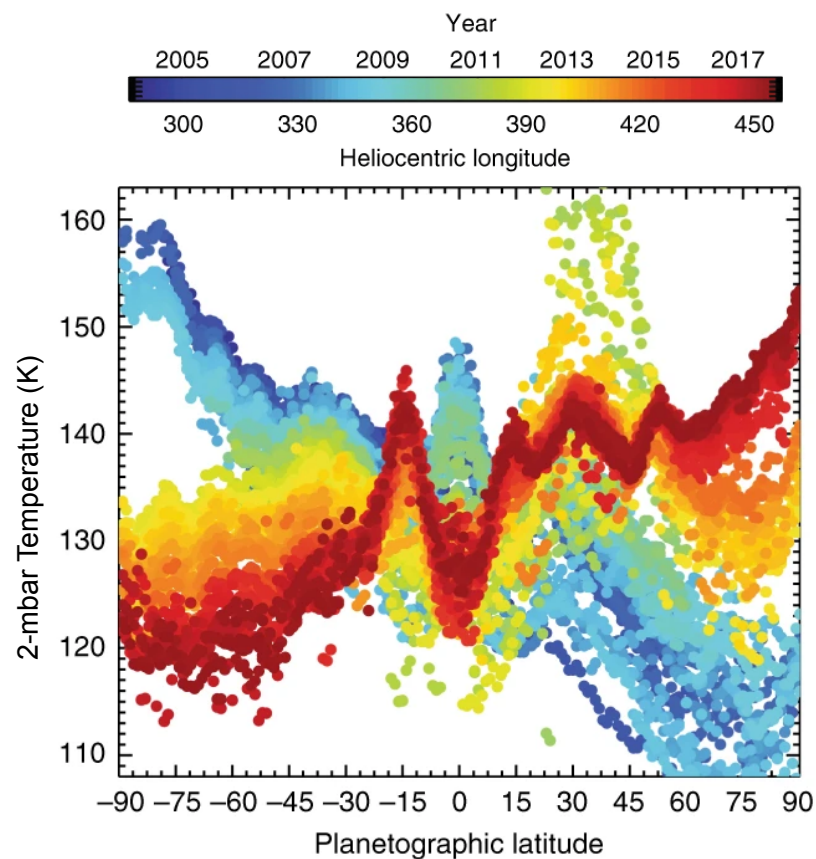


**Figure 18.** Retrieved temperatures of Saturn’s stratosphere at 2 mbar versus latitude over the entire Cassini mission, adapted from Fletcher et al. [78]. The years and heliocentric longitudes—indicating the seasonal phase, with 270 and 360 marking the northern winter solstice and spring equinox, respectively—are indicated by the color bar.

### 3.3.3. Uranus Variability

Reviewing all temporal variability detected in the mid-infrared on Uranus is unfortunately a very brief exercise. There is simply very little to compare given the limited amount of mid-infrared data that exists. Furthermore, what does exist appears largely invariant over the short history of these observations relative to the lengthy 21-year seasons on Uranus.

One might reasonably expect seasonality on Uranus to be interesting given its extreme axial tilt of  $98^\circ$ , which forces nearly all latitudes into extended periods of total daylight and darkness [317]. However, its atmosphere is sluggish vertical mixing, low stratospheric methane abundances, and cold temperatures result in a great thermal inertia that leads to theoretically small seasonal changes and large lags [211,326,352]. The atmospheric temperatures are thus expected to remain close to the annual mean radiative equilibrium values, even though the seasonal amplitude of the radiative forcing is large [211]. There is some discrepancy in the literature over the length of the theoretical radiative time constants as a function of height for the outer planet atmospheres (see Section 3.3 and Figure 15). Conrath et al. [211] calculated values of over 130 years in the upper-troposphere and stratosphere, but Li et al. [326] found them to be significantly shorter—ranging from roughly 10 to 70 years at pressures of 400 to 70 mbar. The latter would suggest the potential for variability, and observations could potentially confirm or refute these theoretical expectations.

When Voyager-IRIS produced the first temperature maps of Uranus near the time of the southern summer, there were little differences between the summer and winter hemispheric temperatures at the tropopause. The summer pole was no warmer than the winter pole in

the tropopause and only marginally warmer in the lower stratosphere [77]. This indicated that seasonal variation in the upper troposphere was indeed very small. Subsequent comparisons between Voyager-era temperatures and ground-based imaging acquired over 20 and 32 years later revealed no significant changes in the upper-tropospheric (70–400 mbar) temperatures more than a full season later [33,77]. Significant temperature changes have yet to be found.

In the stratosphere, observations are even more limited. Only nine years separate the existing images sensitive to stratospheric emission, and they appear invariant within the considerable uncertainties [33] (see Figures 13 and 14). There have been some hints of possible variation in ground-based images [33] and Spitzer-IRS observations, averaged over different sub-observer longitudes, but these have been interpreted as possible evidence of longitudinal variation, rather than temporal variability [276]. A lack of temporal variability in the stratosphere would be consistent with the expected long stratospheric radiative time constants [211,326] (see Figure 15). However, additional mid-infrared observations, repeated frequently over the coming decade, will be needed to determine whether significant temperature or chemical changes actually occur on Uranus.

### 3.3.4. Neptune Variability

Despite its supremely long seasonal timescales (165 year orbit) and great distance from the Sun, Neptune exhibits remarkable variability at mid-infrared wavelengths. Like Uranus, Neptune's temperatures were first mapped by Voyager-IRIS. Like Uranus, comparisons with subsequent ground-based imaging have shown the upper tropospheric temperatures are largely invariant in time within uncertainties [72,74]. The possible exception is at the south pole, which demonstrates possible variability in the troposphere with no obvious pattern [72,74], but it is subject to large uncertainties. However, unlike Uranus, Neptune's stratosphere clearly exhibits considerable variability.

A recent analysis of all mid-infrared observations of Neptune existing prior to 2020 has revealed an overall decline in mid-infrared radiances since reliable imaging began in 2003 [74] (see Figure 19). Combined with spectral data sensitive to atmospheric temperatures via the  $\sim 17.03\text{-}\mu\text{m}$   $\text{H}_2\text{ S}(1)$  quadrupole emission, these observations indicated that Neptune's disk-integrated temperatures dropped by roughly 8 K in the lower stratosphere [74]. These changes are unexpected, since radiative-seasonal models predicted that temperatures should rise in Neptune's southern hemisphere in early summer [70,211].

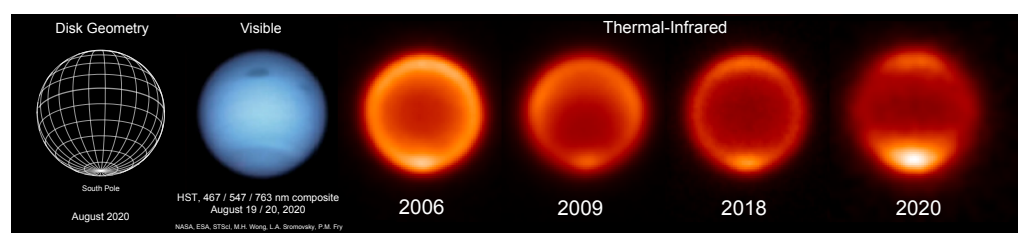


**Figure 19.** A sequence of mid-infrared images showing the variation of Neptune at roughly  $12\ \mu\text{m}$  in different years, along with disk geometry and a Hubble Space Telescope (HST) visible image for comparison. The mid-infrared images were taken from VLT-VISIR (2006, 2009, 2018) and Subaru-COMICS (2020) [74]. The sequence shows a global decline in radiances accompanied by dramatic warming at Neptune's south pole between 2018 and 2020. The HST image was taken in 2020, three weeks after the Subaru-COMICS image. (HST Image credit: NASA, ESA, STScI, M.H. Wong (University of California, Berkeley), and L.A. Sromovsky and P.M. Fry (University of Wisconsin-Madison)).

While global temperatures dropped, images sensitive to  $12\text{-}\mu\text{m}$  emission from stratospheric ethane showed a dramatic surge in radiance from Neptune's south pole between 2018 and 2020—again attributed to a rise in temperatures ( $\sim 13\ \text{K}$ ) inferred from nearly contemporaneous  $\text{H}_2\text{ S}(1)$  spectra [74]. This warming circumpolar vortex was combined with a drop in temperatures at nearly all other latitudes (see Figure 20). Radiative and

chemical models have predicted a gradual brightening of the south pole following the southern summer solstice in 2005 [70,211], but such rapid change is unexpected.

The cause of these stratospheric temperature changes is currently unknown. Roman et al. [74] speculated that it may be related to seasonal changes in chemistry [317], which alters the cooling rates, but explanations involving solar cycle variations, stratospheric oscillations, and meteorological activity cannot be discounted. With such dramatic and unexpected changes in recent years, regular observations over the next decade will be crucial for understanding the nature and trends shaping the stratospheric variability of Neptune.

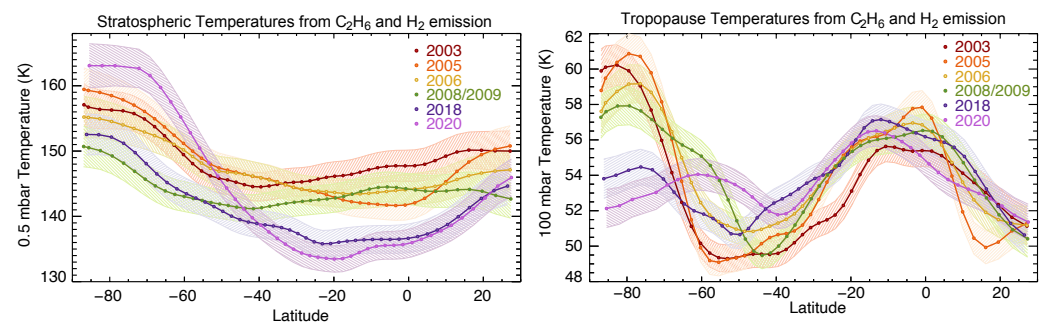


**Figure 20.** Neptune’s temperatures versus planetocentric latitude from ground-based images dating from different years, adapted from Roman et al. [74]. Shaded envelopes indicate uncertainties. Temperatures are shown at 0.5 mbar (left) and 100 mbar (right), corresponding to peaks in the contribution from stratospheric ethane (12.2  $\mu\text{m}$ ) and tropospheric hydrogen CIA ( $\sim 18\text{--}25 \mu\text{m}$ ). The stratospheric temperatures vary in time, with brightening at the pole in recent years. Tropospheric temperatures are largely invariant, except for the south pole. Data are from Keck-LWS (2003), Gemini-N-Michelle (2005), VLT-VISIR (2006–2018), and Subaru-COMICS (2020).

#### 4. Conclusions

From more than a century of remote sensing at mid-IR wavelengths, a remarkably detailed picture of the temperature structure, chemistry, and dynamics of the giant planets has emerged. Many questions and challenges remain, particularly regarding how and why the planets change over time.

Much of the knowledge written in this review will soon be rewritten. The upcoming Solar System observations of the giant planets by JWST-MIRI have the potential to greatly surpass existing observations and revise our knowledge of the atmospheres of the giant planets, particularly regarding the Ice Giants [1,317]. Nonetheless, this brief look into the history and results of mid-infrared remote sensing can hopefully continue to provide insight and inspiration, if simply by considering how far the field has come.

**Funding:** During the preparation of this manuscript, the author was supported by a European Research Council Consolidator Grant, under the European Union’s Horizons 2020 research and innovation program, grant number 723890.

**Data Availability Statement:** No new data were created or analyzed in this study. Data sharing is not applicable to this article. The data presented in this study are available from the original sources, as referenced.

**Acknowledgments:** I wish to thank Leigh Fletcher and Imke de Pater for offering the opportunity, support, and patience necessary for completing this review. I also wish to acknowledge Arrate Antuñano for her readiness to assist with her expertise on the Gas Giant atmospheres.

In memory of Peter Jay Gierasch (1940–2023), an insightful scientist and generous advisor, whose many enduring contributions have uniquely shaped the field of planetary atmospheres, as demonstrated throughout this review.

**Conflicts of Interest:** The authors declare no conflict of interest.

## References

1. Norwood, J.; Moses, J.; Fletcher, L.N.; Orton, G.; Irwin, P.G.; Atreya, S.; Rages, K.; Cavalié, T.; Sánchez-Lavega, A.; Hueso, R.; et al. Giant planet observations with the James Webb Space Telescope. *Publ. Astron. Soc. Pac.* **2016**, *128*, 018005. [[CrossRef](#)]
2. CIE S 017:2020; ILV: International Lighting Vocabulary, 2nd ed.; Commission Internationale de L'Éclairage: Vienna, Austria, 2020.
3. ISO 20473:2007; Optics and Photonics—Spectral Bands. ISO: Geneva, Switzerland, 2007.
4. Guan, X.; Yu, X.; Periyangounder, D.; Benzigar, M.R.; Huang, J.K.; Lin, C.H.; Kim, J.; Singh, S.; Hu, L.; Liu, G.; et al. Recent progress in short-to long-wave infrared photodetection using 2D materials and heterostructures. *Adv. Opt. Mater.* **2021**, *9*, 2001708. [[CrossRef](#)]
5. Noll, S.; Kausch, W.; Barden, M.; Jones, A.; Szyszka, C.; Kimeswenger, S.; Vinther, J. An atmospheric radiation model for Cerro Paranal-I. The optical spectral range. *Astron. Astrophys.* **2012**, *543*, A92. [[CrossRef](#)]
6. Jones, A.; Noll, S.; Kausch, W.; Szyszka, C.; Kimeswenger, S. An advanced scattered moonlight model for Cerro Paranal. *Astron. Astrophys.* **2013**, *560*, A91. [[CrossRef](#)]
7. Fazio, G. Infrared array detectors in astrophysics. *Infrared Phys. Technol.* **1994**, *35*, 107–117. [[CrossRef](#)]
8. Haller, E. Advanced far-infrared detectors. *Infrared Phys. Technol.* **1994**, *35*, 127–146. [[CrossRef](#)]
9. Glass, I.S.; Glass, I. *Handbook of Infrared Astronomy*; Cambridge University Press: Cambridge, UK, 1999; Number 1.
10. Tokunaga, A. Infrared astronomy. In *Allen's Astrophysical Quantities*; Springer: Berlin/Heidelberg, Germany, 2002; pp. 143–167.
11. Rieke, G. *Detection of Light: From the Ultraviolet to the Submillimeter*; Cambridge University Press: Cambridge, UK, 2003.
12. McLean, I.S. *Infrared Astronomy with Arrays: The Next Generation*; Springer Science & Business Media: Berlin/Heidelberg, Germany, 2012; Volume 190.
13. Ives, D.; Finger, G.; Jakob, G.; Beckmann, U. AQUARIUS: The next generation mid-IR detector for ground-based astronomy, an update. In *High Energy, Optical, and Infrared Detectors for Astronomy VI*; SPIE: Bellingham, WA, USA, 2014; Volume 9154, pp. 489–499.
14. Larson, H.P. Infrared spectroscopic observations of the outer planets, their satellites, and the asteroids. *Annu. Rev. Astron. Astrophys.* **1980**, *18*, 43–75. [[CrossRef](#)]
15. Mampaso, A.; Prieto, M.; Sánchez, F. *Infrared Astronomy*; Cambridge University Press: Cambridge, UK, 2004.
16. Rieke, M.J.; Kelly, D.M.; Horner, S.D. Overview of James Webb Space Telescope and NIRCAM's Role. In *Cryogenic Optical Systems and Instruments XI*; SPIE: Bellingham, WA, USA, 2005; Volume 5904, p. 590401.
17. Wells, M.; Lee, D.; Oudenhuisen, A.; Hastings, P.; Pel, J.W.; Glasse, A. The MIRI medium resolution spectrometer for the James Webb Space Telescope. In *Space Telescopes and Instrumentation I: Optical, Infrared, and Millimeter*; SPIE: Bellingham, WA, USA, 2006; Volume 6265, pp. 358–369.
18. Rieke, G.H.; Wright, G.; Böker, T.; Bouwman, J.; Colina, L.; Glasse, A.; Gordon, K.; Greene, T.; Güdel, M.; Henning, T.; et al. The mid-infrared instrument for the James Webb Space Telescope, I: Introduction. *Publ. Astron. Soc. Pac.* **2015**, *127*, 584–594. [[CrossRef](#)]
19. Encrenaz, T. Infrared spectroscopy of exoplanets: Observational constraints. *Philos. Trans. R. Soc. Lond.* **2014**, *372*, 20130083. [[CrossRef](#)] [[PubMed](#)]
20. Pluriel, W. Hot Exoplanetary Atmospheres in 3D. *Remote Sens.* **2023**, *15*, 635. [[CrossRef](#)]
21. Naylor, D.A.; Clark, T.A.; Schultz, A.A.; Davis, G.R. Atmospheric transmission at submillimetre wavelengths from Mauna Kea. *Mon. Not. R. Astron. Soc.* **1991**, *251*, 199–202. [[CrossRef](#)]
22. De Pater, I. The significance of microwave observations for the planets. *Phys. Rep.* **1991**, *200*, 1–50. [[CrossRef](#)]
23. Encrenaz, T.; Moreno, R. The microwave spectra of planets. In *AIP Conference Proceedings*; American Institute of Physics: College Park, MD, USA, 2002; Volume 616, pp. 330–337.
24. de Pater, I.; Romani, P.N.; Atreya, S.K. Possible microwave absorption by H<sub>2</sub>S gas in Uranus' and Neptune's atmospheres. *Icarus* **1991**, *91*, 220–233. [[CrossRef](#)]
25. Gebbie, H.; Harding, W.; Hilsum, C.; Pryce, A.; Roberts, V. Atmospheric transmission in the 1 to 14  $\mu$  region. *Proc. R. Soc. Lond. Ser. A Math. Phys. Sci.* **1951**, *206*, 87–107.
26. Taylor, J.H.; Yates, H.W. Atmospheric transmission in the infrared. *JOSA* **1957**, *47*, 223–226. [[CrossRef](#)]
27. Smette, A.; Sana, H.; Noll, S.; Horst, H.; Kausch, W.; Kimeswenger, S.; Barden, M.; Szyszka, C.; Jones, A.M.; Gallenne, A.; et al. Molecfit: A general tool for telluric absorption correction-I. Method and application to ESO instruments. *Astron. Astrophys.* **2015**, *576*, A77. [[CrossRef](#)]
28. Thomas, J.; Robinson, G.; Hyland, A. Intermediate Bandwidth Spectrometry in the 10-Micron Region and its Interpretation. *Mon. Not. R. Astron. Soc.* **1976**, *174*, 711–723. [[CrossRef](#)]
29. Kendrew, S.; Jolissaint, L.; Brandl, B.; Lenzen, R.; Pantin, E.; Glasse, A.; Blommaert, J.; Venema, L.; Siebenmorgen, R.; Molster, F. Mid-infrared astronomy with the E-ELT: Performance of METIS. In *Ground-Based and Airborne Instrumentation for Astronomy III*; SPIE: Bellingham, WA, USA, 2010; Volume 7735, pp. 2017–2029.
30. Noll, S.; Kausch, W.; Barden, M.; Jones, A.M.; Szyszka, C.; Kimeswenger, S. *The Cerro Paranal Advanced Sky Model*; VLT-MAN-ESO-19550-5339; European Southern Observatory: München, Germany, 2013; Issue 1.1.1, p. 50.
31. Holzlohner, R.; Kimeswenger, S.; Kausch, W.; Noll, S. Bolometric night sky temperature and subcooling of telescope structures. *Astron. Astrophys.* **2021**, *645*, A32. [[CrossRef](#)]
32. Papoular, R. The processing of infrared sky noise by chopping, nodding and filtering. *Astron. Astrophys.* **1983**, *117*, 46–52.

33. Roman, M.T.; Fletcher, L.N.; Orton, G.S.; Rowe-Gurney, N.; Irwin, P.G. Uranus in northern midspring: Persistent atmospheric temperatures and circulations inferred from thermal imaging. *Astron. J.* **2020**, *159*, 45. [[CrossRef](#)]
34. Wiedemann, G. Science with the VLT: High-resolution infrared spectroscopy. *Messenger* **1996**, *86*, 24–30.
35. Kasper, M.; Arsenault, R.; Käufl, H.U.; Jakob, G.; Fuenteseca, E.; Riquelme, M.; Siebenmorgen, R.; Sterzik, M.; Zins, G.; Ageorges, N.; et al. NEAR: Low-mass planets in Cen with VISIR. *Messenger* **2017**, *169*, 16–20.
36. Moses, J.I.; Fouchet, T.; Yelle, R.V.; Friedson, A.J.; Orton, G.S.; Bézard, B.; Drossart, P.; Gladstone, G.R.; Kostiuik, T.; Livengood, T.A. The stratosphere of Jupiter. In *Jupiter: Planet, Satellites and Magnetosphere*; Cambridge University Press: Cambridge, UK, 2004; pp. 129–157.
37. Moses, J.; Fouchet, T.; Bézard, B.; Gladstone, G.; Lellouch, E.; Feuchtgruber, H. Photochemistry and diffusion in Jupiter's stratosphere: Constraints from ISO observations and comparisons with other giant planets. *J. Geophys. Res. Planets* **2005**, *110*. [[CrossRef](#)]
38. Fouchet, T.; Moses, J.I.; Conrath, B.J. Saturn: Composition and chemistry. In *Saturn from Cassini-Huygens*; Springer: Dordrecht, The Netherlands, 2009; pp. 83–112.
39. Moses, J.; Cavalié, T.; Fletcher, L.; Roman, M. Atmospheric chemistry on Uranus and Neptune. *Philos. Trans. R. Soc. A* **2020**, *378*, 20190477. [[CrossRef](#)] [[PubMed](#)]
40. Irwin, P.; Teanby, N.; De Kok, R.; Fletcher, L.; Howett, C.; Tsang, C.; Wilson, C.; Calcutt, S.; Nixon, C.; Parrish, P. The NEMESIS planetary atmosphere radiative transfer and retrieval tool. *J. Quant. Spectrosc. Radiat. Transf.* **2008**, *109*, 1136–1150. [[CrossRef](#)]
41. Kuiper, G.P. New absorptions in the uranian atmosphere. *Astrophys. J.* **1949**, *109*, 540–541. [[CrossRef](#)]
42. Weidenschilling, S.; Lewis, J. Atmospheric and cloud structures of the Jovian planets. *Icarus* **1973**, *20*, 465–476. [[CrossRef](#)]
43. Orton, G.S.; Ingersoll, A.P. Saturn's atmospheric temperature structure and heat budget. *J. Geophys. Res. Space Phys.* **1980**, *85*, 5871–5881. [[CrossRef](#)]
44. Conrath, B.; Pirraglia, J. Thermal structure of Saturn from Voyager infrared measurements: Implications for atmospheric dynamics. *Icarus* **1983**, *53*, 286–292. [[CrossRef](#)]
45. Fletcher, L.; Orton, G.; Teanby, N.; Irwin, P.; Bjoraker, G. Methane and its isotopologues on Saturn from Cassini/CIRS observations. *Icarus* **2009**, *199*, 351–367. [[CrossRef](#)]
46. Fletcher, L.N.; de Pater, I.; Reach, W.; Wong, M.; Orton, G.; Irwin, P.; Gehrz, R. Jupiter's para-H<sub>2</sub> distribution from SOFIA/FORCAST and Voyager/IRIS 17–37 μm spectroscopy. *Icarus* **2017**, *286*, 223–240. [[CrossRef](#)]
47. Burgdorf, M.; Orton, G.; van Cleve, J.; Meadows, V.; Houck, J. Detection of new hydrocarbons in Uranus' atmosphere by infrared spectroscopy. *Icarus* **2006**, *184*, 634–637. [[CrossRef](#)]
48. Feuchtgruber, H.; Lellouch, E.; de Graauw, T.; Bézard, B.; Encrenaz, T.; Griffin, M. External supply of oxygen to the atmospheres of the giant planets. *Nature* **1997**, *389*, 159–162. [[CrossRef](#)]
49. Orton, G.S. The thermal structure of Jupiter II. Observations and analysis of 8–14 micron radiation. *Icarus* **1975**, *26*, 142–158. [[CrossRef](#)]
50. Orton, G.S.; Friedson, A.J.; Baines, K.H.; Martin, T.Z.; West, R.A.; Caldwell, J.; Hammel, H.B.; Bergstralh, J.T.; Malcom, M.E.; Golisch, W.F.; et al. Thermal maps of Jupiter: Spatial organization and time dependence of stratospheric temperatures, 1980 to 1990. *Science* **1991**, *252*, 537–542. [[CrossRef](#)] [[PubMed](#)]
51. Fletcher, L.N.; Orton, G.; Mousis, O.; Yanamandra-Fisher, P.; Parrish, P.; Irwin, P.; Fisher, B.; Vanzi, L.; Fujiyoshi, T.; Fuse, T.; et al. Thermal structure and composition of Jupiter's Great Red Spot from high-resolution thermal imaging. *Icarus* **2010**, *208*, 306–328. [[CrossRef](#)]
52. Fletcher, L.N.; Greathouse, T.; Orton, G.; Sinclair, J.; Giles, R.; Irwin, P.; Encrenaz, T. Mid-infrared mapping of Jupiter's temperatures, aerosol opacity and chemical distributions with IRTF/TEXES. *Icarus* **2016**, *278*, 128–161. [[CrossRef](#)]
53. Fletcher, L.N.; Orton, G.; Rogers, J.; Giles, R.; Payne, A.; Irwin, P.; Vedovato, M. Moist convection and the 2010–2011 revival of Jupiter's South Equatorial Belt. *Icarus* **2017**, *286*, 94–117. [[CrossRef](#)]
54. Antuñano, A.; Fletcher, L.N.; Orton, G.S.; Toledo, D.; Melin, H.; Roman, M.T.; Sinclair, J.A.; Donnelly, P.T.; Morton, E.K.; Selves, P. Characterizing temperature and aerosol variability during Jupiter's 2006–2007 Equatorial Zone disturbance. *J. Geophys. Res. Planets* **2020**, *125*, e2020JE006413. [[CrossRef](#)]
55. Courtin, R.; Gautier, D.; Marten, A.; Bézard, B.; Hanel, R. The composition of Saturn's atmosphere at northern temperate latitudes from Voyager IRIS spectra-NH<sub>3</sub>, PH<sub>3</sub>, C<sub>2</sub>H<sub>2</sub>, C<sub>2</sub>H<sub>6</sub>, CH<sub>3</sub>D, CH<sub>4</sub>, and the Saturnian D/H isotopic ratio. *Astrophys. J.* **1984**, *287*, 899–916. [[CrossRef](#)]
56. Noll, K.; Knacke, R.; Tokunaga, A.; Lacy, J.; Beck, S.; Serabyn, E. The abundances of ethane and acetylene in the atmospheres of Jupiter and Saturn. *Icarus* **1986**, *65*, 257–263. [[CrossRef](#)]
57. Sada, P.V.; McCabe, G.H.; Bjoraker, G.L.; Jennings, D.E.; Reuter, D.C. 13C-ethane in the atmospheres of Jupiter and Saturn. *Astrophys. J.* **1996**, *472*, 903. [[CrossRef](#)]
58. Fletcher, L.; Irwin, P.; Teanby, N.; Orton, G.; Parrish, P.; Calcutt, S.; Bowles, N.; de Kok, R.; Howett, C.; Taylor, F. The meridional phosphine distribution in Saturn's upper troposphere from Cassini/CIRS observations. *Icarus* **2007**, *188*, 72–88. [[CrossRef](#)]
59. Fletcher, L.; Irwin, P.; Orton, G.; Teanby, N.; Achterberg, R.; Bjoraker, G.; Read, P.; Simon-Miller, A.; Howett, C.; de Kok, R.; et al. Temperature and composition of Saturn's polar hot spots and hexagon. *Science* **2008**, *319*, 79–81. [[CrossRef](#)]

60. Hesman, B.E.; Jennings, D.E.; Sada, P.V.; Bjoraker, G.L.; Achterberg, R.K.; Simon-Miller, A.A.; Anderson, C.M.; Boyle, R.J.; Nixon, C.A.; Fletcher, L.N.; et al. Saturn's latitudinal C<sub>2</sub>H<sub>2</sub> and C<sub>2</sub>H<sub>6</sub> abundance profiles from Cassini/CIRS and ground-based observations. *Icarus* **2009**, *202*, 249–259. [[CrossRef](#)]
61. Fletcher, L.; Orton, G.; Yanamandra-Fisher, P.; Fisher, B.; Parrish, P.; Irwin, P. Retrievals of atmospheric variables on the gas giants from ground-based mid-infrared imaging. *Icarus* **2009**, *200*, 154–175. [[CrossRef](#)]
62. Fletcher, L.N.; Hesman, B.; Achterberg, R.; Irwin, P.; Bjoraker, G.; Goriuss, N.; Hurley, J.; Sinclair, J.; Orton, G.; Legarreta, J.; et al. The origin and evolution of Saturn's 2011–2012 stratospheric vortex. *Icarus* **2012**, *221*, 560–586. [[CrossRef](#)]
63. Fletcher, L.N.; Greathouse, T.K.; Guerlet, S.; Moses, J.I.; West, R.A. Saturn's Seasonally Changing Atmosphere. In *Saturn in the 21st Century*; Cambridge University Press: Cambridge, UK, 2018; Volume 20, p. 251.
64. Blake, J.S.; Fletcher, L.N.; Greathouse, T.K.; Orton, G.S.; Melin, H.; Roman, M.T.; Antuñano, A.; Donnelly, P.T.; Rowe-Gurney, N.; King, O. Refining Saturn's deuterium-hydrogen ratio via IRTF/TEXES spectroscopy. *Astron. Astrophys.* **2021**, *653*, A66. [[CrossRef](#)]
65. Blake, J.S.; Fletcher, L.N.; Orton, G.S.; Antuñano, A.; Roman, M.T.; Kasaba, Y.; Fujiyoshi, T.; Melin, H.; Bardet, D.; Sinclair, J.A.; et al. Saturn's seasonal variability from four decades of ground-based mid-infrared observations. *Icarus* **2023**, *392*, 115347. [[CrossRef](#)]
66. Tokunaga, A.; Orton, G.; Caldwell, J. New observational constraints on the temperature inversions of Uranus and Neptune. *Icarus* **1983**, *53*, 141–146. [[CrossRef](#)]
67. Orton, G.S.; Tokunaga, A.T.; Caldwell, J. Observational constraints on the atmospheres of Uranus and Neptune from new measurements near 10  $\mu$ m. *Icarus* **1983**, *56*, 147–164. [[CrossRef](#)]
68. Orton, G.S.; Lacy, J.H.; Achtermann, J.M.; Parmar, P.; Blass, W.E. Thermal spectroscopy of Neptune: The stratospheric temperature, hydrocarbon abundances, and isotopic ratios. *Icarus* **1992**, *100*, 541–555. [[CrossRef](#)]
69. Fletcher, L.N.; Drossart, P.; Burgdorf, M.; Orton, G.; Encrenaz, T. Neptune's atmospheric composition from AKARI infrared spectroscopy. *Astron. Astrophys.* **2010**, *514*, A17. [[CrossRef](#)]
70. Greathouse, T.K.; Richter, M.; Lacy, J.; Moses, J.; Orton, G.; Encrenaz, T.; Hammel, H.; Jaffe, D. A spatially resolved high spectral resolution study of Neptune's stratosphere. *Icarus* **2011**, *214*, 606–621. [[CrossRef](#)]
71. Orton, G.S.; Moses, J.I.; Fletcher, L.N.; Mainzer, A.K.; Hines, D.; Hammel, H.B.; Martin-Torres, J.; Burgdorf, M.; Merlet, C.; Line, M.R. Mid-infrared spectroscopy of Uranus from the Spitzer infrared spectrometer: 2. Determination of the mean composition of the upper troposphere and stratosphere. *Icarus* **2014**, *243*, 471–493. [[CrossRef](#)]
72. Fletcher, L.N.; de Pater, I.; Orton, G.S.; Hammel, H.B.; Sitko, M.L.; Irwin, P.G. Neptune at summer solstice: Zonal mean temperatures from ground-based observations, 2003–2007. *Icarus* **2014**, *231*, 146–167. [[CrossRef](#)]
73. de Pater, I.; Fletcher, L.N.; Luszcz-Cook, S.; DeBoer, D.; Butler, B.; Hammel, H.B.; Sitko, M.L.; Orton, G.; Marcus, P.S. Neptune's global circulation deduced from multi-wavelength observations. *Icarus* **2014**, *237*, 211–238. [[CrossRef](#)]
74. Roman, M.T.; Fletcher, L.N.; Orton, G.S.; Greathouse, T.K.; Moses, J.I.; Rowe-Gurney, N.; Irwin, P.G.; Antuñano, A.; Sinclair, J.; Kasaba, Y.; et al. Subseasonal Variation in Neptune's Mid-infrared Emission. *Planet. Sci. J.* **2022**, *3*, 78. [[CrossRef](#)]
75. de Pater, I.; Fletcher, L.N.; Pérez-Hoyos, S.; Hammel, H.B.; Orton, G.S.; Wong, M.H.; Luszcz-Cook, S.; Sánchez-Lavega, A.; Boslough, M. A multi-wavelength study of the 2009 impact on Jupiter: Comparison of high resolution images from Gemini, Keck and HST. *Icarus* **2010**, *210*, 722–741. [[CrossRef](#)]
76. Orton, G.S.; Fletcher, L.N.; Moses, J.I.; Mainzer, A.K.; Hines, D.; Hammel, H.B.; Martin-Torres, F.J.; Burgdorf, M.; Merlet, C.; Line, M.R. Mid-infrared spectroscopy of Uranus from the Spitzer Infrared Spectrometer: 1. Determination of the mean temperature structure of the upper troposphere and stratosphere. *Icarus* **2014**, *243*, 494–513. [[CrossRef](#)]
77. Orton, G.S.; Fletcher, L.N.; Encrenaz, T.; Leyrat, C.; Roe, H.G.; Fujiyoshi, T.; Pantin, E. Thermal imaging of Uranus: Upper-tropospheric temperatures one season after Voyager. *Icarus* **2015**, *260*, 94–102. [[CrossRef](#)]
78. Fletcher, L.; Orton, G.; Sinclair, J.; Guerlet, S.; Read, P.; Antuñano, A.; Achterberg, R.; Flasar, F.; Irwin, P.; Bjoraker, G.; et al. A hexagon in Saturn's northern stratosphere surrounding the emerging summertime polar vortex. *Nat. Commun.* **2018**, *9*, 3564. [[CrossRef](#)]
79. Fletcher, L.N.; Orton, G.S.; Greathouse, T.K.; Rogers, J.H.; Zhang, Z.; Oyafuso, F.A.; Eichstädt, G.; Melin, H.; Li, C.; Levin, S.M.; et al. Jupiter's equatorial plumes and hot spots: Spectral mapping from Gemini/TEXES and Juno/MWR. *J. Geophys. Res. Planets* **2020**, *125*, e2020JE006399. [[CrossRef](#)]
80. Gillett, F.; Low, F.; Stein, W. The 2.8–14-micron spectrum of Jupiter. *Astrophys. J.* **1969**, *157*, 925–934. [[CrossRef](#)]
81. Westphal, J. Observations of localised 5-micron radiation from Jupiter. *Astrophys. J.* **1969**, *157*, L63–L64. [[CrossRef](#)]
82. Keay, C.; Low, F.; Rieke, G.; Minton, R. High-resolution maps of Jupiter at 5 microns. *Astrophys. J.* **1973**, *183*, 1063–1074. [[CrossRef](#)]
83. Westphal, J.; Matthews, K.; Terrile, R.J. Five-micron pictures of Jupiter. *Astrophys. J.* **1974**, *188*, L111–L112. [[CrossRef](#)]
84. Fink, U.; Larson, H.P.; Treffers, R.R. Germane in the atmosphere of Jupiter. *Icarus* **1978**, *34*, 344–354. [[CrossRef](#)]
85. Bjoraker, G.L.; Larson, H.P.; Kunde, V.G. The gas composition of Jupiter derived from 5- $\mu$ m airborne spectroscopic observations. *Icarus* **1986**, *66*, 579–609. [[CrossRef](#)]
86. Bjoraker, G.; Wong, M.; De Pater, I.; Ádámkóvics, M. Jupiter's deep cloud structure revealed using Keck observations of spectrally resolved line shapes. *Astrophys. J.* **2015**, *810*, 122. [[CrossRef](#)]
87. Bjoraker, G.L.; Wong, M.H.; de Pater, I.; Hewagama, T.; Ádámkóvics, M.; Orton, G.S. The gas composition and deep cloud structure of Jupiter's Great Red Spot. *Astron. J.* **2018**, *156*, 101. [[CrossRef](#)]
88. Bjoraker, G.L. Jupiter's elusive water. *Nat. Astron.* **2020**, *4*, 558–559. [[CrossRef](#)]

89. Bjoraker, G.L.; Wong, M.H.; de Pater, I.; Hewagama, T.; Ádámkóvics, M. The Spatial Variation of Water Clouds, NH<sub>3</sub>, and H<sub>2</sub>O on Jupiter Using Keck Data at 5 Microns. *Remote Sens.* **2022**, *14*, 4567. [CrossRef]
90. Wong, M.H.; Bjoraker, G.L.; Goullaud, C.; Stephens, A.W.; Luszcz-Cook, S.H.; Atreya, S.K.; de Pater, I.; Brown, S.T. Deep Clouds on Jupiter. *Remote Sens.* **2023**, *15*, 702. [CrossRef]
91. Momary, T.W.; Baines, K.; Cassini/VIMS Science Team. The zoology of Saturn: The bizarre features unveiled by the 5 micron eyes of Cassini/VIMS. In *AAS/Division for Planetary Sciences Meeting Abstracts# 38*; AAS: Washington, DC, USA, 2006; Volume 38, pp. 11–21.
92. Bjoraker, G.; Chanover, N.; Glenar, D.; Hewagama, T. Ammonia, phosphine, and cloud structure on Saturn derived from 5-micron spectra. In *AAS/Division for Planetary Sciences Meeting Abstracts# 38*; AAS: Washington, DC, USA, 2006; Volume 38, p. 488.
93. Bjoraker, G.; Chanover, N.; Glenar, D.; Hewagama, T. Saturn's deep cloud structure derived from 5-micron spectra. In *AGU Fall Meeting Abstracts*; AGU: Washington, DC, USA, 2007; Volume 2007, p. P31A-0184.
94. Fletcher, L.N.; Baines, K.H.; Momary, T.W.; Showman, A.P.; Irwin, P.G.; Orton, G.S.; Roos-Serote, M.; Merlet, C. Saturn's tropospheric composition and clouds from Cassini/VIMS 4.6–5.1  $\mu\text{m}$  nightside spectroscopy. *Icarus* **2011**, *214*, 510–533. [CrossRef]
95. Barstow, J.K.; Irwin, P.G.; Fletcher, L.N.; Giles, R.S.; Merlet, C. Probing Saturn's tropospheric cloud with Cassini/VIMS. *Icarus* **2016**, *271*, 400–417. [CrossRef]
96. Yanamandra-Fisher, P.A.; Gutierrez, S.M.; Payne, A.; Orton, G.S.; Sinclair, J. Probing the Depths of Jupiter and Saturn at Five-Microns. In *AAS/Division for Planetary Sciences Meeting Abstracts# 47*; AAS: Washington, DC, USA, 2015; Volume 47, pp. 311–335.
97. Encrenaz, T.; Lellouch, E.; Drossart, P.; Feuchtgruber, H.; Orton, G.S.; Atreya, S.K. First detection of CO in Uranus. *Astron. Astrophys.* **2004**, *413*, L5–L9. [CrossRef]
98. Hodapp, K.W.; Jensen, J.B.; Irwin, E.M.; Yamada, H.; Chung, R.; Fletcher, K.; Robertson, L.; Hora, J.L.; Simons, D.A.; Mays, W.; et al. The Gemini Near-Infrared Imager (NIRI). *Publ. Astron. Soc. Pac.* **2003**, *115*, 1388–1406. [CrossRef]
99. International Gemini Observatory/NOIRLab/NSF/AURA, M.H. Wong, (UC Berkeley) et al. Available online: <https://noirlab.edu/public/images/noirlab2116a/> (accessed on 21 December 2022).
100. Herschel, W. XIV. Experiments on the refrangibility of the invisible rays of the sun. *Philos. Trans. R. Soc. Lond.* **1800**, *90*, 284–292.
101. Coblentz, W.W. Early History of Infrared Spectroradiometry. *Sci. Mon.* **1949**, *68*, 102–107. [PubMed]
102. Langley, S.P. The bolometer and radiant energy. In *Proceedings of the American Academy of Arts and Sciences*; JSTOR: Cambridge, MA, USA 1880; Volume 16, pp. 342–358.
103. Pasachoff, J.M. *Contemporary Astronomy*; Saunders College Pub: Philadelphia, PA, USA, 1985.
104. Walker, H.J. A brief history of infrared astronomy. *Astron. Geophys.* **2000**, *41*, 5–10. [CrossRef]
105. Holland, W.; Duncan, W.; Griffin, M. Bolometers for submillimeter and millimeter astronomy. In *Single-Dish Radio Astronomy: Techniques and Applications*; Astronomical Society of the Pacific: San Francisco, CA, USA, 2002; Volume 278, pp. 463–491.
106. Balog, Z.; Müller, T.; Nielbock, M.; Altieri, B.; Klaas, U.; Blommaert, J.; Linz, H.; Lutz, D.; Moór, A.; Billot, N.; et al. The Herschel-PACS photometer calibration. *Exp. Astron.* **2014**, *37*, 129–160. [CrossRef]
107. Stroke, G.W. Diffraction gratings. *Handbuch Physik* **1967**, *29*, 426–754.
108. Palik, E. History of far-infrared research. I. The Rubens era. *JOSA* **1977**, *67*, 857–865. [CrossRef]
109. Rosse, E.o. On the Radiation of Heat from the Moon.—No. II. *Proc. R. Soc. Lond.* **1870**, *19*, 9–14.
110. Langley, S.P. *The Temperature of the Moon: From Studies at the Allegheny Observatory by SP Langley, With the Assistance of FW Very*; National Academy of Sciences: Washington, DC, USA, 1889; Volume 7.
111. Boys, C.V. III. On the heat of the Moon and stars. *Proc. R. Soc. Lond.* **1890**, *47*, 480–499.
112. Very, F.W. The Probable Range of Temperature on the Moon. I. *Astrophys. J.* **1898**, *8*, 199–217. [CrossRef]
113. Very, F.W. The Probable Range of Temperature on the Moon. II. *Astrophys. J.* **1898**, *8*, 265–286. [CrossRef]
114. Coblentz, W. Further Measurements of Stellar Temperatures and Planetary Radiation. *Proc. Natl. Acad. Sci. USA* **1922**, *8*, 330–333. [CrossRef] [PubMed]
115. Coblentz, W.W.; Lampland, C.O. Measurements of planetary radiation. *Lowell Obs. Bull.* **1923**, *3*, 91–134.
116. Coblentz, W.W.; Lampland, C. New measurements of planetary radiation. *Science* **1924**, *60*, 295. [CrossRef] [PubMed]
117. Coblentz, W.W.; Lampland, C. Some measurements of the spectral components of planetary radiation and planetary temperatures. *J. Frankl. Inst.* **1925**, *199*, 785–841. [CrossRef]
118. Coblentz, W.W.; Lampland, C.; Menzel, D. Temperatures of Mars, 1926, as derived from the Water-Cell Transmissions. *Publ. Astron. Soc. Pac.* **1927**, *39*, 97–100. [CrossRef]
119. Pettit, E.; Nicholson, S.B. Measurements of the Radiation from the Planet Mercury. *Publ. Astron. Soc. Pac.* **1923**, *35*, 194–198. [CrossRef]
120. Pettit, E.; Nicholson, S.B. Radiation measures on the planet Mars. *Publ. Astron. Soc. Pac.* **1924**, *36*, 269–272.
121. Menzel, D.; Coblentz, W.; Lampland, C. Planetary temperatures derived from water-cell transmissions. *Astrophys. J.* **1926**, *63*, 177–187. [CrossRef]
122. Menzel, D.H. Water-cell transmissions and planetary temperatures. *Astrophys. J.* **1923**, *58*, 65–74. [CrossRef]
123. Tholen, D.J.; Tejfel, V.G.; Cox, A.N. Planets and Satellites. In *Allen's Astrophysical Quantities*; Cox, A.N., Ed.; Springer: New York, NY, USA, 2002; pp. 293–313. [CrossRef]
124. Menzel, D.H. Hydrogen abundance and the constitution of the giant planets. *Publ. Astron. Soc. Pac.* **1930**, *42*, 228–232. [CrossRef]

125. Sinton, W.M.; Strong, J. Radiometric Observations of Venus. *Astrophys. J.* **1960**, *131*, 470–490. [[CrossRef](#)]
126. Pfund, A. Resonance radiometry. *Science* **1929**, *69*, 71–72. [[CrossRef](#)]
127. Kivenson, G.; Steinback, R.T.; Rider, M. An Infra-Red Chopped-Radiation Analyzer. *JOSA* **1948**, *38*, 1086–1091. [[CrossRef](#)] [[PubMed](#)]
128. Westphal, J.A.; Murray, B.C.; Martz, D.E. An 8–14 micron infrared astronomical photometer. *Appl. Opt.* **1963**, *2*, 749–753. [[CrossRef](#)]
129. Murray, B.C.; Wildey, R.L.; Westphal, J.A. Observations of Jupiter and the Galilean Satellites at 10 Microns. *Astrophys. J.* **1964**, *139*, 986–993. [[CrossRef](#)]
130. Low, F. Infrared Brightness Temperature of Saturn. *Astron. J.* **1964**, *69*, 550–551. [[CrossRef](#)]
131. Low, F.J. Observations of Venus, Jupiter, and Saturn at  $\lambda 20 \mu$ . *Astron. J.* **1966**, *71*, 391. [[CrossRef](#)]
132. Low, F.J. The infrared brightness temperature of Uranus. *Astrophys. J.* **1966**, *146*, 326–328. [[CrossRef](#)]
133. Harwit, M.; Munutt, D.; Shivanandan, K.; Zajac, B. Results of the first infrared astronomical rocket flight. *Astron. J.* **1966**, *71*, 1026–1029. [[CrossRef](#)]
134. Houck, J.R.; Pollack, J.B.; Schaack, D.; Reed, R.A.; Summers, A. Jupiter: Its infrared spectrum from 16 to 40 micrometers. *Science* **1975**, *189*, 720–722. [[CrossRef](#)] [[PubMed](#)]
135. Danielson, R.E. The infrared spectrum of Jupiter. *Astrophys. J.* **1966**, *143*, 949–960. [[CrossRef](#)]
136. Strong, J. Infrared astronomy by balloon. *Sci. Am.* **1965**, *212*, 28–37. [[CrossRef](#)]
137. Aumann, H.; Gillespie, C., Jr.; Low, F. The internal powers and effective temperatures of Jupiter and Saturn. *Astrophys. J.* **1969**, *157*, L69. [[CrossRef](#)]
138. Armstrong, K.; Harper, D., Jr.; Low, F. Far-infrared brightness temperatures of the planets. *Astrophys. J.* **1972**, *178*, L89–L92. [[CrossRef](#)]
139. Pearl, J.; Conrath, B. The albedo, effective temperature, and energy balance of Neptune, as determined from Voyager data. *J. Geophys. Res. Space Phys.* **1991**, *96*, 18921–18930. [[CrossRef](#)]
140. Li, L.; Jiang, X.; West, R.; Gierasch, P.; Perez-Hoyos, S.; Sanchez-Lavega, A.; Fletcher, L.; Fortney, J.; Knowles, B.; Porco, C.; et al. Less absorbed solar energy and more internal heat for Jupiter. *Nat. Commun.* **2018**, *9*, 3709. [[CrossRef](#)] [[PubMed](#)]
141. Li, L.; Conrath, B.J.; Gierasch, P.J.; Achterberg, R.K.; Nixon, C.A.; Simon-Miller, A.A.; Flasar, F.M.; Banfield, D.; Baines, K.H.; West, R.A.; et al. Saturn's emitted power. *J. Geophys. Res. Planets* **2010**, *115*. [[CrossRef](#)]
142. Simon, T.; Morrison, D.; Cruikshank, D.P. Twenty-micron fluxes of bright stellar standards. *Astrophys. J.* **1972**, *177*, L17. [[CrossRef](#)]
143. Morrison, D.; Cruikshank, D.P. Temperatures of Uranus and Neptune at 24 microns. *Astrophys. J.* **1973**, *179*, 329–332. [[CrossRef](#)]
144. Rieke, G.; Low, F. Infrared measurements of Uranus and Neptune. *Astrophys. J.* **1974**, *193*, L147. [[CrossRef](#)]
145. Macy, W., Jr.; Sinton, W. Detection of methane and ethane emission on Neptune but not on Uranus. *Astrophys. J.* **1977**, *218*, L79–L81. [[CrossRef](#)]
146. Murphy, R.; Trafton, L. Evidence for an internal heat source in Neptune. *Astrophys. J.* **1974**, *193*, 253–255. [[CrossRef](#)]
147. Wright, E. Recalibration of the far-infrared brightness temperatures of the planets. *Astrophys. J.* **1976**, *210*, 250–253. [[CrossRef](#)]
148. Loewenstein, R.; Harper, D.; Moseley, H. The effective temperature of Neptune. *Astrophys. J.* **1977**, *218*, L145–L146. [[CrossRef](#)]
149. Whitcomb, S.; Hildebrand, R.; Keene, J.; Stiening, R.; Harper, D. Submillimeter brightness temperatures of Venus, Jupiter, Uranus, and Neptune. *Icarus* **1979**, *38*, 75–80. [[CrossRef](#)]
150. Epstein, E.E.; Dworetzky, M.M.; Montgomery, J.W.; Fogarty, W.G.; Schorn, R.A. Mars, Jupiter, Saturn, and Uranus: 3.3-mm brightness temperatures and a search for variations with time or phase angle. *Icarus* **1970**, *13*, 276–281. [[CrossRef](#)]
151. Ulich, B.; Cogdell, J.; Davis, J. Planetary brightness temperature measurements at 8.6 mm and 3.1 mm wavelengths. *Icarus* **1973**, *19*, 59–82. [[CrossRef](#)]
152. Werner, M.; Neugebauer, G.; Houck, J.; Hauser, M. New values for the 1-mm brightness temperatures of Mercury, Venus, Jupiter, Saturn, Uranus, and Neptune have been determined using Mars as the absolute photometric standard. *Icarus* **1978**, *35*, 289–296. [[CrossRef](#)]
153. Kellermann, K. Thermal radio emission from the major planets. *Radio Sci.* **1970**, *5*, 487–493. [[CrossRef](#)]
154. Mayer, C.; McCullough, T. Microwave radiation of Uranus and Neptune. *Icarus* **1971**, *14*, 187–191. [[CrossRef](#)]
155. Connes, J.; Connes, P. Near-infrared planetary spectra by Fourier spectroscopy. I. Instruments and results. *JOSA* **1966**, *56*, 896–910. [[CrossRef](#)]
156. Huggins, W.; Huggins, M.L. VII. Note on the photographic spectra of Uranus and Saturn. *Proc. R. Soc. Lond.* **1890**, *46*, 231–233.
157. Draper, H. On photographing the spectra of the stars and planets. *Am. J. Sci.* **1879**, *3*, 419–425. [[CrossRef](#)]
158. Slipher, V.M. The spectra of the major planets. *Lowell Obs. Bull.* **1909**, *1*, 231–238.
159. Adel, A.; Slipher, V. The constitution of the atmospheres of the giant planets. *Phys. Rev.* **1934**, *46*, 902. [[CrossRef](#)]
160. Wildt, R. Absorptionsspektren und atmosphären der gros; en planeten. *Veroeffentlichungen Universitaets-Sternwarte Goettingen* **1932**, *2*, 171–180.
161. Dunham, T. Note on the spectra of Jupiter and Saturn. *Publ. Astron. Soc. Pac.* **1933**, *45*, 42–44. [[CrossRef](#)]
162. Kiess, C.; Corliss, C.; Kiess, H.K. High-Dispersion Spectra of Jupiter. *Astrophys. J.* **1960**, *132*, 221–231. [[CrossRef](#)]
163. Lewis, J.S. Observability of spectroscopically active compounds in the atmosphere of Jupiter. *Icarus* **1969**, *10*, 393–409. [[CrossRef](#)]
164. Wildt, R. Photochemistry of planetary atmospheres. *Astrophys. J.* **1937**, *86*, 321. [[CrossRef](#)]
165. Strobel, D.F. The photochemistry of methane in the jovian atmosphere. *J. Atmos. Sci.* **1969**, *26*, 906–911. [[CrossRef](#)]

166. Ridgway, S. Jupiter: Identification of ethane and acetylene. *Astrophys. J.* **1974**, *187*, L41–L43. [[CrossRef](#)]
167. Tokunaga, A.; Knacke, R.; Owen, T. Ethane and acetylene abundances in the Jovian atmosphere. *Astrophys. J.* **1976**, *209*, 294–301. [[CrossRef](#)]
168. Gillett, F.; Forrest, W. The 7.5-to 13.5-micron spectrum of Saturn. *Astrophys. J.* **1974**, *187*, L37–L39. [[CrossRef](#)]
169. Wark, D.; Hilleary, D. Atmospheric temperature: Successful test of remote probing. *Science* **1969**, *165*, 1256–1258. [[CrossRef](#)] [[PubMed](#)]
170. Ohring, G. The temperature and ammonia profiles in the jovian atmospheres from inversion of the jovian emission spectrum. *Astrophys. J.* **1973**, *184*, 1027–1040. [[CrossRef](#)]
171. Taylor, F. Temperature sounding experiments for the Jovian planets. *J. Atmos. Sci.* **1972**, *29*, 950–958. [[CrossRef](#)]
172. Rodgers, C.D. Retrieval of atmospheric temperature and composition from remote measurements of thermal radiation. *Rev. Geophys.* **1976**, *14*, 609–624. [[CrossRef](#)]
173. Conrath, B.J.; Gierasch, P.J.; Ustinov, E.A. Thermal Structure and Para Hydrogen Fraction on the Outer Planets from Voyager IRIS Measurements. *Icarus* **1998**, *135*, 501–517. [[CrossRef](#)]
174. Connes, P.; Connes, J.; Kaplan, L.; Benedict, W. Carbon monoxide in the Venus atmosphere. *Astrophys. J.* **1968**, *152*, 731–743. [[CrossRef](#)]
175. Connes, J.; Connes, P.; Maillard, J.P. *Atlas des Spectres dans le Proche Infrarouge de Venus, Mars, Jupiter et Saturn*; Centre National de la Recherche Scientifique: Paris, France, 1969.
176. Beer, R.; Taylor, F.W. The abundance of CH<sub>3</sub>D and the D/H ratio in Jupiter. *Astrophys. J.* **1973**, *179*, 309–328. [[CrossRef](#)]
177. Encrenaz, T.; Combes, M.; Zeau, Y. The Spectrum of Jupiter between 10 and 13  $\mu$ . *Astron. Astrophys.* **1978**, *70*, 29–36.
178. Larson, H.; Fink, U.; Treffers, R.; Gautier, T., III. Detection of water vapor on Jupiter. *Astrophys. J.* **1975**, *197*, L137–L140. [[CrossRef](#)]
179. Ridgway, S.; Wallace, L.; Smith, G. The 800–1200 inverse centimeter absorption spectrum of Jupiter. *Astrophys. J.* **1976**, *207*, 1002–1006. [[CrossRef](#)]
180. Larson, H.; Treffers, R.; Fink, U. Phosphine in Jupiter’s atmosphere—The evidence from high-altitude observations at 5 micrometers. *Astrophys. J.* **1977**, *211*, 972–979. [[CrossRef](#)]
181. Beer, R. Detection of carbon monoxide in Jupiter. *Astrophys. J.* **1975**, *200*, L167–L169. [[CrossRef](#)]
182. Larson, H.; Fink, U.; Treffers, R. Evidence for CO in Jupiter’s atmosphere from airborne spectroscopic observations at 5 microns. *Astrophys. J.* **1978**, *219*, 1084–1092. [[CrossRef](#)]
183. Prinn, R.G.; Lewis, J.S. Phosphine on Jupiter and implications for the Great Red Spot. *Science* **1975**, *190*, 274–276. [[CrossRef](#)]
184. Prinn, R.G.; Barshay, S.S. Carbon monoxide on Jupiter and implications for atmospheric convection. *Science* **1977**, *198*, 1031–1034. [[CrossRef](#)]
185. Fink, U.; Larson, H.P. Deuterated methane observed on Saturn. *Science* **1978**, *201*, 343–345. [[CrossRef](#)] [[PubMed](#)]
186. Bregman, J.; Lester, D.; Rank, D. Observation of the nu-squared band of PH<sub>3</sub> in the atmosphere of Saturn. *Astrophys. J.* **1975**, *202*, L55–L56. [[CrossRef](#)]
187. Larson, H.; Fink, U.; Smith, H.; Davis, D. The middle-infrared spectrum of Saturn—Evidence for phosphine and upper limits to other trace atmospheric constituents. *Astrophys. J.* **1980**, *240*, 327–337. [[CrossRef](#)]
188. Tokunaga, A.; Knacke, R.; Owen, T. The detection of ethane on Saturn. *Astrophys. J.* **1975**, *197*, L77–L78. [[CrossRef](#)]
189. Encrenaz, T.; Combes, M.; Zeau, Y.; Vapillon, L.; Berezne, J. A tentative identification of C<sub>2</sub>H<sub>4</sub> in the spectrum of Saturn. *Astron. Astrophys.* **1975**, *42*, 355–356.
190. Encrenaz, T.; Owen, T.; Woodman, J. The abundance of ammonia on Jupiter, Saturn and Titan. *Astron. Astrophys.* **1974**, *37*, 49–55.
191. Noll, K.S.; Knacke, R.; Geballe, T.; Tokunaga, A. Evidence for germane in Saturn. *Icarus* **1988**, *75*, 409–422. [[CrossRef](#)]
192. Chase, S.; Ruiz, R.; Mnch, G.; Neugebauer, G.; Schroeder, M.; Trafton, L. Pioneer 10 infrared radiometer experiment: Preliminary results. *Science* **1974**, *183*, 315–317. [[CrossRef](#)]
193. Ingersoll, A.; Münch, G.; Neugebauer, G.; Diner, D.; Orton, G.; Schupler, B.; Schroeder, M.; Chase, S.; Ruiz, R.; Trafton, L. Pioneer 11 infrared radiometer experiment: The global heat balance of Jupiter. *Science* **1975**, *188*, 472–473. [[CrossRef](#)]
194. Ingersoll, A.; Münch, G.; Neugebauer, G.; Orton, G. Results of the infrared radiometer experiment on Pioneers 10 and 11. In *IAU Colloq. 30: Jupiter: Studies of the Interior, Atmosphere, Magnetosphere and Satellites*; University of Arizona Press: Tucson, AZ, USA, 1976; pp. 197–205.
195. Ingersoll, A.; Orton, G.; Münch, G.; Neugebauer, G.; Chase, S. Pioneer Saturn infrared radiometer: Preliminary results. *Science* **1980**, *207*, 439–443. [[CrossRef](#)] [[PubMed](#)]
196. Hanel, R.; Conrath, B.; Herath, L.; Kunde, V.; Pirraglia, J. Albedo, internal heat, and energy balance of Jupiter: Preliminary results of the Voyager infrared investigation. *J. Geophys. Res. Space Phys.* **1981**, *86*, 8705–8712. [[CrossRef](#)]
197. Hanel, R.; Conrath, B.; Flasar, M.; Kunde, V.; Lowman, P.; Maguire, W.; Pearl, J.; Pirraglia, J.; Samuelson, R.; Gautier, D.; et al. Infrared observations of the Jovian system from Voyager 1. *Science* **1979**, *204*, 972–976. [[CrossRef](#)]
198. Kim, S.J.; Caldwell, J.; Rivolo, A.; Wagener, R.; Orton, G.S. Infrared polar brightening on Jupiter: III. Spectrometry from the Voyager 1 IRIS experiment. *Icarus* **1985**, *64*, 233–248. [[CrossRef](#)]
199. Marten, A.; Rouan, D.; Baluteau, J.P.; Gautier, D.; Conrath, B.J.; Hanel, R.A.; Kunde, V.; Samuelson, R.; Chedin, A.; Scott, N. Study of the ammonia ice cloud layer in the equatorial region of Jupiter from the infrared interferometric experiment on Voyager. *Icarus* **1981**, *46*, 233–248. [[CrossRef](#)]

200. Gautier, D.; Conrath, B.; Flasar, M.; Hanel, R.; Kunde, V.; Chedin, A.; Scott, N. The helium abundance of Jupiter from Voyager. *J. Geophys. Res. Space Phys.* **1981**, *86*, 8713–8720. [[CrossRef](#)]
201. Pirraglia, J.; Conrath, B.; Allison, M.; Gierasch, P. Thermal structure and dynamics of Saturn and Jupiter. *Nature* **1981**, *292*, 677–679. [[CrossRef](#)]
202. Conrath, B.; Gautier, D.; Hanel, R.; Hornstein, J. The helium abundance of Saturn from Voyager measurements. *Astrophys. J.* **1984**, *282*, 807–815. [[CrossRef](#)]
203. Hanel, R.; Conrath, B.; Kunde, V.; Pearl, J.; Pirraglia, J. Albedo, internal heat flux, and energy balance of Saturn. *Icarus* **1983**, *53*, 262–285. [[CrossRef](#)]
204. Bézard, B.; Gautier, D.; Conrath, B. A seasonal model of the Saturnian upper troposphere: Comparison with Voyager infrared measurements. *Icarus* **1984**, *60*, 274–288. [[CrossRef](#)]
205. Conrath, B.J.; Gautier, D. Saturn helium abundance: A reanalysis of Voyager measurements. *Icarus* **2000**, *144*, 124–134. [[CrossRef](#)]
206. Pearl, J.; Conrath, B.; Hanel, R.; Pirraglia, J.; Coustenis, A. The albedo, effective temperature, and energy balance of Uranus, as determined from Voyager IRIS data. *Icarus* **1990**, *84*, 12–28. [[CrossRef](#)]
207. Conrath, B.; Gautier, D.; Hanel, R.; Lindal, G.; Marten, A. The helium abundance of Uranus from Voyager measurements. *J. Geophys. Res. Space Phys.* **1987**, *92*, 15003–15010. [[CrossRef](#)]
208. Conrath, B.; Gautier, D.; Lindal, G.; Samuelson, R.; Shaffer, W. The helium abundance of Neptune from Voyager measurements. *J. Geophys. Res. Space Phys.* **1991**, *96*, 18907–18919. [[CrossRef](#)]
209. Smith, B.A.; Soderblom, L.A.; Banfield, D.; Basilevsky, A.; Beebe, R.; Bollinger, K.; Boyce, J.; Brahic, A.; Briggs, G.; Brown, R.; et al. Voyager 2 at Neptune: Imaging science results. *Science* **1989**, *246*, 1422–1449. [[CrossRef](#)]
210. Conrath, B.; Flasar, F.; Hanel, R.; Kunde, V.; Maguire, W.; Pearl, J.; Pirraglia, J.; Samuelson, R.; Gierasch, P.; Weir, A.; et al. Infrared observations of the Neptunian system. *Science* **1989**, *246*, 1454–1459. [[CrossRef](#)] [[PubMed](#)]
211. Conrath, B.J.; Gierasch, P.J.; Leroy, S.S. Temperature and circulation in the stratosphere of the outer planets. *Icarus* **1990**, *83*, 255–281. [[CrossRef](#)]
212. Smith, W.H. On the ortho-para equilibrium of H<sub>2</sub> in the atmospheres of the Jovian planets. *Icarus* **1978**, *33*, 210–216. [[CrossRef](#)]
213. Fletcher, L.N.; Gustafsson, M.; Orton, G.S. Hydrogen dimers in giant-planet infrared spectra. *Astrophys. J. Suppl. Ser.* **2018**, *235*, 24. [[CrossRef](#)]
214. Conrath, B.J.; Gierasch, P.J. Evidence for disequilibrium of ortho and para hydrogen on Jupiter from Voyager IRIS measurements. *Nature* **1983**, *306*, 571–572. [[CrossRef](#)]
215. Gierasch, P.J.; Conrath, B.J.; Magalha, J.A. Zonal mean properties of Jupiter's upper troposphere from Voyager infrared observations. *Icarus* **1986**, *67*, 456–483. [[CrossRef](#)]
216. Bagenal, F.; Dowling, T.E.; McKinnon, W.B.; McKinnon, W. *Jupiter: The Planet, Satellites and Magnetosphere*; Cambridge University Press: Cambridge, UK, 2007; Volume 1.
217. Fischer, D. *Mission Jupiter: The Spectacular Journey of the Galileo Spacecraft*; Springer: Berlin/Heidelberg, Germany, 2001.
218. Hunten, D.; Colin, L.; Hansen, J. Atmospheric science on the Galileo mission. *Space Sci. Rev.* **1986**, *44*, 191–240. [[CrossRef](#)]
219. Russell, C.T. *The Galileo Mission*; Springer Science & Business Media: Berlin/Heidelberg, Germany, 2012.
220. Carlson, R.; Weissman, P.; Smythe, W.; Mahoney, J. Near-infrared mapping spectrometer experiment on Galileo. In *The Galileo Mission*; Springer Science+Business Media: Dordrecht, The Netherlands, 1992; pp. 457–502.
221. Russell, E.; Brown, F.; Chandos, R.; Fincher, W.; Kubel, L.; Lasis, A.; Travis, L. Galileo photopolarimeter/radiometer experiment. *Space Sci. Rev.* **1992**, *60*, 531–563. [[CrossRef](#)]
222. Nixon, C.; Irwin, P.; Calcutt, S.; Taylor, F.; Carlson, R. Atmospheric composition and cloud structure in Jovian 5- $\mu$ m hotspots from analysis of Galileo NIMS measurements. *Icarus* **2001**, *150*, 48–68. [[CrossRef](#)]
223. Irwin, P.; Calcutt, S.; Taylor, F. Radiative transfer models for Galileo NIMS studies of the atmosphere of Jupiter. *Adv. Space Res.* **1997**, *19*, 1149–1158. [[CrossRef](#)]
224. Dyudina, U.; Ingersoll, A.; Danielson, G.; Baines, K.; Carlson, R.; NIMS, T.G.; Teams, S. Interpretation of NIMS and SSI images on the Jovian cloud structure. *Icarus* **2001**, *150*, 219–233. [[CrossRef](#)]
225. Irwin, P.; Dyudina, U. The retrieval of cloud structure maps in the equatorial region of Jupiter using a principal component analysis of Galileo/NIMS data. *Icarus* **2002**, *156*, 52–63. [[CrossRef](#)]
226. Orton, G.; Spencer, J.; Travis, L.; Martin, T.; Tamppari, L. Galileo photopolarimeter-radiometer observations of Jupiter and the Galilean satellites. *Science* **1996**, *274*, 389–391. [[CrossRef](#)]
227. Matson, D.L.; Spilker, L.J.; Lebreton, J.P. The Cassini/Huygens mission to the Saturnian system. *Space Sci. Rev.* **2002**, *104*, 1–58. [[CrossRef](#)]
228. Dougherty, M.; Esposito, L.; Krimigis, S.M. *Saturn from Cassini-huygens*; Springer: Berlin/Heidelberg, Germany, 2009.
229. Hansen, C.J.; Bolton, S.J.; Matson, D.L.; Spilker, L.J.; Lebreton, J.P. The Cassini–Huygens flyby of jupiter. *Icarus* **2004**, *172*, 1–8. [[CrossRef](#)]
230. Brown, R.H.; Baines, K.H.; Bellucci, G.; Bibring, J.P.; Buratti, B.J.; Capaccioni, F.; Cerroni, P.; Clark, R.N.; Coradini, A.; Cruikshank, D.P.; et al. The Cassini visual and infrared mapping spectrometer (VIMS) investigation. In *The Cassini-Huygens Mission: Orbiter Remote Sensing Investigations*; Springer: Dordrecht, The Netherlands, 2004; pp. 111–168.

231. Flasar, F.M.; Kunde, V.; Abbas, M.; Achterberg, R.; Ade, P.; Barucci, A.; Bézard, B.; Bjoraker, G.; Brasunas, J.; Calcutt, S.; et al. Exploring the Saturn system in the thermal infrared: The composite infrared spectrometer. In *The Cassini-Huygens Mission*; Springer: Dordrecht, The Netherlands, 2004; pp. 169–297.
232. Jennings, D.E.; Flasar, F.; Kunde, V.; Nixon, C.; Segura, M.; Romani, P.; Gorius, N.; Albright, S.; Brasunas, J.; Carlson, R.; et al. Composite infrared spectrometer (CIRS) on Cassini. *Appl. Opt.* **2017**, *56*, 5274–5294. [[CrossRef](#)]
233. Sromovsky, L.; Fry, P. The source of widespread 3- $\mu\text{m}$  absorption in Jupiter's clouds: Constraints from 2000 Cassini VIMS observations. *Icarus* **2010**, *210*, 230–257. [[CrossRef](#)]
234. Sromovsky, L.; Baines, K.; Fry, P. Models of bright storm clouds and related dark ovals in Saturn's Storm Alley as constrained by 2008 Cassini/VIMS spectra. *Icarus* **2018**, *302*, 360–385. [[CrossRef](#)]
235. Sromovsky, L.; Baines, K.; Fry, P. Evolution of Saturn's north polar color and cloud structure between 2012 and 2017 inferred from Cassini VIMS and ISS observations. *Icarus* **2021**, *362*, 114409. [[CrossRef](#)]
236. Simon-Miller, A.A.; Conrath, B.J.; Gierasch, P.J.; Orton, G.S.; Achterberg, R.K.; Flasar, F.M.; Fisher, B.M. Jupiter's atmospheric temperatures: From Voyager IRIS to Cassini CIRS. *Icarus* **2006**, *180*, 98–112. [[CrossRef](#)]
237. Li, L.; Baines, K.H.; Smith, M.A.; West, R.A.; Pérez-Hoyos, S.; Trammell, H.J.; Simon-Miller, A.A.; Conrath, B.J.; Gierasch, P.J.; Orton, G.S.; et al. Emitted power of Jupiter based on Cassini CIRS and VIMS observations. *J. Geophys. Res. Planets* **2012**, *117*. [[CrossRef](#)]
238. Matcheva, K.I.; Conrath, B.J.; Gierasch, P.J.; Flasar, F.M. The cloud structure of the jovian atmosphere as seen by the Cassini/CIRS experiment. *Icarus* **2005**, *179*, 432–448. [[CrossRef](#)]
239. Wong, M.H.; Bjoraker, G.L.; Smith, M.D.; Flasar, F.M.; Nixon, C.A. Identification of the 10- $\mu\text{m}$  ammonia ice feature on Jupiter. *Planet. Space Sci.* **2004**, *52*, 385–395. [[CrossRef](#)]
240. Achterberg, R.K.; Conrath, B.J.; Gierasch, P.J. Cassini CIRS retrievals of ammonia in Jupiter's upper troposphere. *Icarus* **2006**, *182*, 169–180. [[CrossRef](#)]
241. Irwin, P.; Parrish, P.; Fouchet, T.; Calcutt, S.; Taylor, F.; Simon-Miller, A.; Nixon, C. Retrievals of jovian tropospheric phosphine from Cassini/CIRS. *Icarus* **2004**, *172*, 37–49. [[CrossRef](#)]
242. Fletcher, L.; Orton, G.; Teanby, N.; Irwin, P. Phosphine on jupiter and saturn from cassini/cirs. *Icarus* **2009**, *202*, 543–564. [[CrossRef](#)]
243. Nixon, C.; Achterberg, R.; Conrath, B.; Irwin, P.; Teanby, N.; Fouchet, T.; Parrish, P.; Romani, P.; Abbas, M.; LeClair, A.; et al. Meridional variations of C<sub>2</sub>H<sub>2</sub> and C<sub>2</sub>H<sub>6</sub> in Jupiter's atmosphere from Cassini CIRS infrared spectra. *Icarus* **2007**, *188*, 47–71. [[CrossRef](#)]
244. Pierel, J.; Nixon, C.; Lellouch, E.; Fletcher, L.; Bjoraker, G.; Achterberg, R.; Bézard, B.; Hesman, B.; Irwin, P.; Flasar, F. D/H ratios on Saturn and Jupiter from Cassini CIRS. *Astron. J.* **2017**, *154*, 178. [[CrossRef](#)]
245. Fouchet, T.; Orton, G.; Irwin, P.G.; Calcutt, S.B.; Nixon, C.A. Upper limits on hydrogen halides in Jupiter from Cassini/CIRS observations. *Icarus* **2004**, *170*, 237–241. [[CrossRef](#)]
246. Nixon, C.A.; Achterberg, R.K.; Romani, P.N.; Allen, M.; Zhang, X.; Teanby, N.A.; Irwin, P.G.; Flasar, F.M. Abundances of Jupiter's trace hydrocarbons from Voyager and Cassini. *Planet. Space Sci.* **2010**, *58*, 1667–1680. [[CrossRef](#)]
247. Sinclair, J.; Moses, J.; Hue, V.; Greathouse, T.; Orton, G.; Fletcher, L.; Irwin, P. Jupiter's auroral-related stratospheric heating and chemistry III: Abundances of C<sub>2</sub>H<sub>4</sub>, CH<sub>3</sub>C<sub>2</sub>H, C<sub>4</sub>H<sub>2</sub> and C<sub>6</sub>H<sub>6</sub> from Voyager-IRIS and Cassini-CIRS. *Icarus* **2019**, *328*, 176–193. [[CrossRef](#)]
248. Fletcher, L.; Irwin, P.; Teanby, N.; Orton, G.; Parrish, P.; de Kok, R.; Howett, C.; Calcutt, S.; Bowles, N.; Taylor, F. Characterising Saturn's vertical temperature structure from Cassini/CIRS. *Icarus* **2007**, *189*, 457–478. [[CrossRef](#)]
249. Fletcher, L.N.; Achterberg, R.K.; Greathouse, T.K.; Orton, G.S.; Conrath, B.J.; Simon-Miller, A.A.; Teanby, N.; Guerlet, S.; Irwin, P.G.; Flasar, F. Seasonal change on Saturn from Cassini/CIRS observations, 2004–2009. *Icarus* **2010**, *208*, 337–352. [[CrossRef](#)]
250. Guerlet, S.; Fouchet, T.; Bézard, B.; Flasar, F.; Simon-Miller, A. Evolution of the equatorial oscillation in Saturn's stratosphere between 2005 and 2010 from Cassini/CIRS limb data analysis. *Geophys. Res. Lett.* **2011**, *38*. [[CrossRef](#)]
251. Sinclair, J.; Irwin, P.; Fletcher, L.; Moses, J.; Greathouse, T.; Friedson, A.; Hesman, B.; Hurley, J.; Merlet, C. Seasonal variations of temperature, acetylene and ethane in Saturn's atmosphere from 2005 to 2010, as observed by Cassini-CIRS. *Icarus* **2013**, *225*, 257–271. [[CrossRef](#)]
252. Sylvestre, M.; Guerlet, S.; Fouchet, T.; Spiga, A.; Flasar, F.; Hesman, B.; Bjoraker, G. Seasonal changes in Saturn's stratosphere inferred from Cassini/CIRS limb observations. *Icarus* **2015**, *258*, 224–238. [[CrossRef](#)]
253. Fletcher, L.N.; Irwin, P.G.; Achterberg, R.K.; Orton, G.S.; Flasar, F.M. Seasonal variability of Saturn's tropospheric temperatures, winds and para-H<sub>2</sub> from Cassini far-IR spectroscopy. *Icarus* **2016**, *264*, 137–159. [[CrossRef](#)]
254. Guerlet, S.; Fouchet, T.; Bézard, B.; Moses, J.I.; Fletcher, L.N.; Simon-Miller, A.A.; Flasar, F.M. Meridional distribution of CH<sub>3</sub>C<sub>2</sub>H and C<sub>4</sub>H<sub>2</sub> in Saturn's stratosphere from CIRS/Cassini limb and nadir observations. *Icarus* **2010**, *209*, 682–695. [[CrossRef](#)]
255. Guerlet, S.; Fouchet, T.; Bézard, B.; Simon-Miller, A.A.; Flasar, F.M. Vertical and meridional distribution of ethane, acetylene and propane in Saturn's stratosphere from CIRS/Cassini limb observations. *Icarus* **2009**, *203*, 214–232. [[CrossRef](#)]
256. Teanby, N.; Fletcher, L.; Irwin, P.; Fouchet, T.; Orton, G. New upper limits for hydrogen halides on Saturn derived from Cassini-CIRS data. *Icarus* **2006**, *185*, 466–475. [[CrossRef](#)]

257. Howett, C.; Irwin, P.; Teanby, N.; Simon-Miller, A.; Calcutt, S.; Fletcher, L.; de Kok, R. Meridional variations in stratospheric acetylene and ethane in the southern hemisphere of the saturnian atmosphere as determined from Cassini/CIRS measurements. *Icarus* **2007**, *190*, 556–572. [[CrossRef](#)]
258. Hesman, B.; BJORAKER, G.; Sada, P.; Achterberg, R.; Jennings, D.; Romani, P.; Lunsford, A.; Fletcher, L.; Boyle, R.; Simon-Miller, A.; et al. Elusive ethylene detected in Saturn's northern storm region. *Astrophys. J.* **2012**, *760*, 24. [[CrossRef](#)]
259. Hurley, J.; Fletcher, L.; Irwin, P.; Calcutt, S.; Sinclair, J.; Merlet, C. Latitudinal variation of upper tropospheric NH<sub>3</sub> on Saturn derived from Cassini/CIRS far-infrared measurements. *Planet. Space Sci.* **2012**, *73*, 347–363. [[CrossRef](#)]
260. Abbas, M.; LeClair, A.; Woodard, E.; Young, M.; Stanbro, M.; Flasar, F.; Kunde, V.; Achterberg, R.; BJORAKER, G.; Brasunas, J.; et al. Distribution of CO<sub>2</sub> in Saturn's atmosphere from Cassini/CIRS infrared observations. *Astrophys. J.* **2013**, *776*, 73. [[CrossRef](#)]
261. Koskinen, T.; Moses, J.; West, R.; Guerlet, S.; Jouchoux, A. The detection of benzene in Saturn's upper atmosphere. *Geophys. Res. Lett.* **2016**, *43*, 7895–7901. [[CrossRef](#)]
262. Koskinen, T.; Guerlet, S. Atmospheric structure and helium abundance on Saturn from Cassini/UVIS and CIRS observations. *Icarus* **2018**, *307*, 161–171. [[CrossRef](#)]
263. Ingersoll, A.P. Cassini exploration of the planet Saturn: A comprehensive review. *Space Sci. Rev.* **2020**, *216*, 122. [[CrossRef](#)]
264. Leech, K.; Kester, D.; Shipman, R.; Beintema, D.; Feuchtgruber, H.; Heras, A.; Huygen, R.; Lahuis, F.; Lutz, D.; Morris, P.; et al. *The ISO Handbook, Volume V-SWS-The Short Wavelength Spectrometer*; ESA Special Publication: Noordwijk, The Netherlands, 2003.
265. Sloan, G.; Kraemer, K.E.; Price, S.D.; Shipman, R.F. A uniform database of 2.4–45.4 micron spectra from the Infrared Space Observatory Short Wavelength Spectrometer. *Astrophys. J. Suppl. Ser.* **2003**, *147*, 379–401. [[CrossRef](#)]
266. Encrenaz, T.; de Graauw, T.; Schaeidt, S.; Lellouch, E.; Feuchtgruber, H.; Beintema, D.; Bézard, B.; Drossart, P.; Griffin, M.; Heras, A.; et al. First results of ISO-SWS observations of Jupiter. *Astron. Astrophys.* **1996**, *315*, L397–L400.
267. Bézard, B.; Feuchtgruber, H.; Moses, J.; Encrenaz, T. Detection of methyl radicals (CH<sub>3</sub>) on Saturn. *Astron. Astrophys.* **1998**, *334*, L41–L44.
268. De Graauw, T.; Feuchtgruber, H.; Bézard, B.; Drossart, P.; Encrenaz, T.; Beintema, D.; Griffin, M.; Heras, A.; Kessler, M.; Leech, K.; et al. First results of ISO-SWS observations of Saturn: Detection of CO<sub>2</sub>, CH<sub>3</sub>C<sub>2</sub>H, C<sub>4</sub>H<sub>2</sub> and tropospheric H<sub>2</sub>O. *Astron. Astrophys.* **1997**, *321*, L13–L16.
269. Lellouch, E.; Feuchtgruber, H.; de Graauw, T.; Bézard, B.; Encrenaz, T.; Griffin, M. H<sub>2</sub>O and CO<sub>2</sub> in the Upper Atmospheres of the Giant Planets. In *AAS/Division for Planetary Sciences Meeting Abstracts# 29*; ASS: Washington, DC, USA 1997; Volume 29, p. 992.
270. Bézard, B.; Romani, P.; Feuchtgruber, H.; Encrenaz, T. Detection of the methyl radical on Neptune. *Astrophys. J.* **1999**, *515*, 868. [[CrossRef](#)]
271. Encrenaz, T.; Drossart, P.; Feuchtgruber, H.; Lellouch, E.; Bézard, B.; Fouchet, T.; Atreya, S. The atmospheric composition and structure of Jupiter and Saturn from ISO observations: A preliminary review. *Planet. Space Sci.* **1999**, *47*, 1225–1242. [[CrossRef](#)]
272. Werner, M.W.; Roellig, T.; Low, F.; Rieke, G.H.; Rieke, M.; Hoffmann, W.; Young, E.; Houck, J.; Brandl, B.; Fazio, G.; et al. The Spitzer space telescope mission. *Astrophys. J. Suppl. Ser.* **2004**, *154*, 1. [[CrossRef](#)]
273. Houck, J.R.; Roellig, T.L.; Van Cleve, J.; Forrest, W.J.; Herter, T.; Lawrence, C.R.; Matthews, K.; Reitsema, H.J.; Soifer, B.T.; Watson, D.M.; et al. The infrared spectrograph\*(IRS) on the Spitzer space telescope. *Astrophys. J. Suppl. Ser.* **2004**, *154*, 18. [[CrossRef](#)]
274. Meadows, V.S.; Orton, G.; Line, M.; Liang, M.C.; Yung, Y.L.; Van Cleve, J.; Burgdorf, M.J. First Spitzer observations of Neptune: Detection of new hydrocarbons. *Icarus* **2008**, *197*, 585–589. [[CrossRef](#)]
275. Rowe-Gurney, N.; Fletcher, L.; Orton, G.; Roman, M.; Sinclair, J.; Moses, J.; Irwin, P. Neptune's Atmospheric Structure from the Spitzer Infrared Spectrometer. Technical Report. In *Proceedings of the 15th Europlanet Science Congress 2021*, Online, 13–24 September 2021.
276. Rowe-Gurney, N.; Fletcher, L.N.; Orton, G.S.; Roman, M.T.; Mainzer, A.; Moses, J.I.; De Pater, I.; Irwin, P.G. Longitudinal variations in the stratosphere of Uranus from the Spitzer infrared spectrometer. *Icarus* **2021**, *365*, 114506. [[CrossRef](#)]
277. Gezari, D.Y.; Mumma, M.J.; Espenak, F.; Deming, D.; BJORAKER, G.; Woods, L.; Folz, W. New features in Saturn's atmosphere revealed by high-resolution thermal infrared images. *Nature* **1989**, *342*, 777–780. [[CrossRef](#)]
278. Hoffmann, W.F.; Fazio, G.G.; Shivanandan, K.; Hora, J.L.; Deutsch, L.K. MIRAC: A mid-infrared array camera for astronomy. In *Infrared Detectors and Instrumentation*; SPIE: Bellingham, WA, USA, 1993; Volume 1946, pp. 449–460.
279. Hoffmann, W.F.; Fazio, G.G.; Shivanandan, K.; Hora, J.L.; Deutsch, L.K. Astronomical observations with the Mid-Infrared Array Camera, MIRAC. *Infrared Phys. Technol.* **1994**, *35*, 175–194. [[CrossRef](#)]
280. Jones, B.; Puetter, R.C. Keck long-wavelength spectrometer. In *Infrared Detectors and Instrumentation*; International Society for Optics and Photonics: Bellingham, WA, USA, 1993; Volume 1946, pp. 610–621.
281. Glasse, A.C.; Etedgui-Atad, E.; Harris, J.W. Michelle midinfrared spectrometer and imager. In *Optical Telescopes of Today and Tomorrow*; International Society for Optics and Photonics: Bellingham, WA, USA, 1997; Volume 2871, pp. 1197–1203.
282. Lagage, P.; Pel, J.; Authier, M.; Belorgey, J.; Claret, A.; Doucet, C.; Dubreuil, D.; Durand, G.; Elswijk, E.; Girardot, P.; et al. Successful Commissioning OF. *Messenger* **2004**, *117*, 12.
283. De Buizer, J.M.; Fisher, R.S. T-ReCS and Michelle: The mid-infrared spectroscopic capabilities of the Gemini observatory. In *High Resolution Infrared Spectroscopy in Astronomy*; Springer: Berlin/Heidelberg, Germany, 2005; pp. 84–87.
284. Kataza, H.; Okamoto, Y.; Takubo, S.; Onaka, T.; Sako, S.; Nakamura, K.; Miyata, T.; Yamashita, T. COMICS: The cooled mid-infrared camera and spectrometer for the Subaru telescope. In *Optical and IR Telescope Instrumentation and Detectors*; International Society for Optics and Photonics: Bellingham, WA, USA, 2000; Volume 4008, pp. 1144–1152.

285. Fletcher, L.N.; Hesman, B.E.; Irwin, P.G.; Baines, K.H.; Momary, T.W.; Sanchez-Lavega, A.; Flasar, F.M.; Read, P.L.; Orton, G.S.; Simon-Miller, A.; et al. Thermal structure and dynamics of Saturn's northern springtime disturbance. *Science* **2011**, *332*, 1413–1417. [[CrossRef](#)] [[PubMed](#)]
286. Lacy, J.; Richter, M.; Greathouse, T.; Jaffe, D.; Zhu, Q. TEXES: A sensitive high-resolution grating spectrograph for the mid-infrared. *Publ. Astron. Soc. Pac.* **2002**, *114*, 153–168. [[CrossRef](#)]
287. Fletcher, L.N.; Greathouse, T.K.; Orton, G.S.; Irwin, P.G.; Mousis, O.; Sinclair, J.A.; Giles, R.S. The origin of nitrogen on Jupiter and Saturn from the 15N/14N ratio. *Icarus* **2014**, *238*, 170–190. [[CrossRef](#)]
288. Sinclair, J.; Orton, G.; Greathouse, T.; Fletcher, L.N.; Moses, J.; Hue, V.; Irwin, P. Jupiter's auroral-related stratospheric heating and chemistry II: Analysis of IRTF-TEXES spectra measured in December 2014. *Icarus* **2018**, *300*, 305–326. [[CrossRef](#)]
289. Fletcher, L.N.; Melin, H.; Adriani, A.; Simon, A.; Sanchez-Lavega, A.; Donnelly, P.; Antuñano, A.; Orton, G.; Hueso, R.; Kraaikamp, E.; et al. Jupiter's Mesoscale Waves Observed at 5  $\mu\text{m}$  by Ground-based Observations and Juno JIRAM. *Astron. J.* **2018**, *156*, 67. [[CrossRef](#)]
290. Melin, H.; Fletcher, L.; Donnelly, P.; Greathouse, T.; Lacy, J.; Orton, G.; Giles, R.; Sinclair, J.; Irwin, P. Assessing the long-term variability of acetylene and ethane in the stratosphere of Jupiter. *Icarus* **2018**, *305*, 301–313. [[CrossRef](#)]
291. Blain, D.; Fouchet, T.; Greathouse, T.; Encrenaz, T.; Charnay, B.; Bézard, B.; Li, C.; Lellouch, E.; Orton, G.; Fletcher, L.N.; et al. Mapping of Jupiter's tropospheric NH<sub>3</sub> abundance using ground-based IRTF/TEXES observations at 5  $\mu\text{m}$ . *Icarus* **2018**, *314*, 106–120. [[CrossRef](#)]
292. Sinclair, J.A.; Greathouse, T.K.; Giles, R.S.; Antuñano, A.; Moses, J.I.; Fouchet, T.; Bézard, B.; Tao, C.; Martín-Torres, J.; Clark, G.B.; et al. Spatial Variations in the Altitude of the CH<sub>4</sub> Homopause at Jupiter's Mid-to-high Latitudes, as Constrained from IRTF-TEXES Spectra. *Planet. Sci. J.* **2020**, *1*, 85. [[CrossRef](#)]
293. Greathouse, T.K.; Lacy, J.H.; Bézard, B.; Moses, J.I.; Griffith, C.A.; Richter, M.J. Meridional variations of temperature, C<sub>2</sub>H<sub>2</sub> and C<sub>2</sub>H<sub>6</sub> abundances in Saturn's stratosphere at southern summer solstice. *Icarus* **2005**, *177*, 18–31. [[CrossRef](#)]
294. Moses, J.; Greathouse, T. Latitudinal and seasonal models of stratospheric photochemistry on Saturn: Comparison with infrared data from IRTF/TEXES. *J. Geophys. Res. Planets* **2005**, *110*. [[CrossRef](#)]
295. Greathouse, T.K.; Lacy, J.H.; Bézard, B.; Moses, J.I.; Richter, M.J.; Knez, C. The first detection of propane on Saturn. *Icarus* **2006**, *181*, 266–271. [[CrossRef](#)]
296. Fouchet, T.; Greathouse, T.K.; Spiga, A.; Fletcher, L.N.; Guerlet, S.; Leconte, J.; Orton, G.S. Stratospheric aftermath of the 2010 Storm on Saturn as observed by the TEXES instrument. I. Temperature structure. *Icarus* **2016**, *277*, 196–214. [[CrossRef](#)]
297. Trafton, L.M.; Orton, G.; Greathouse, T.; Lacy, J.; Encrenaz, T. Mid-IR Observations of Uranus' H<sub>2</sub> Quadrupole Emission Near Equinox. In *AAS/Division for Planetary Sciences Meeting Abstracts# 44*; AAS: Washington, DC, USA, 2012; Volume 44, p. 412.21.
298. Orton, G.; Trafron, L.; Fletcher, L.; Encrenaz, T.; Roman, M.; Greathouse, T.; Lacy, J.; Sinclair, J.; Moses, J.; Leyrat, C.; et al. Spatial Variability in the Stratosphere of Uranus. *Geophys. Res. Abstr.* **2019**, *21*, 1.
299. Kamizuka, T.; Miyata, T.; Sako, S.; Nakamura, T.; Asano, K.; Uchiyama, M.; Okada, K.; Onaka, T.; Sakon, I.; Kataza, H.; et al. Development of MIMIZUKU: A mid-infrared multi-field imager for 6.5-m TAO telescope. In *Ground-Based and Airborne Instrumentation for Astronomy IV*; SPIE: Bellingham, WA, USA, 2012; Volume 8446, pp. 1982–1992.
300. Miyata, T.; Yoshii, Y.; Doi, M.; Kohno, K.; Tanaka, M.; Motohara, K.; Minezaki, T.; Sako, S.; Morokuma, T.; Tanabe, T.; et al. The University of Tokyo Atacama Observatory 6.5 m telescope: Project status 2022. In *Ground-Based and Airborne Telescopes IX*; SPIE: Bellingham, WA, USA, 2022; Volume 12182, pp. 385–393.
301. Kamizuka, T. Challenging the Difficulties in Ground-Based MIR Observations: The Case of TAO/MIMIZUKU. IR2022: An Infrared Bright Future for Ground-Based IR Observatories in the Era of JWST. 2022; p. 19. Available online: <https://zenodo.org/communities/ir2022> (accessed on 27 December 2022).
302. Kamizuka, T.; Miyata, T.; Sako, S.; Ohsawa, R.; Asano, K.; Uchiyama, M.S.; Mori, T.; Yoshida, Y.; Tachibana, K.; Michifuji, T.; et al. The University of Tokyo Atacama Observatory 6.5 m telescope: On-sky performance evaluations of the mid-infrared instrument MIMIZUKU on the Subaru telescope. In *Ground-Based and Airborne Instrumentation for Astronomy VIII*; SPIE: Bellingham, WA, USA, 2020; Volume 11447, pp. 1296–1314.
303. Brandl, B.R.; Lenzen, R.; Pantin, E.; Glasse, A.; Blommaert, J.; Meyer, M.; Guedel, M.; Venema, L.; Molster, F.; Stuik, R.; et al. METIS: The thermal infrared instrument for the E-ELT. In *Ground-Based and Airborne Instrumentation for Astronomy IV*; SPIE: Bellingham, WA, USA, 2012; Volume 8446, pp. 554–566.
304. Brandl, B.R.; Bettonvil, F.; van Boekel, R.; Glauser, A.; Quanz, S.P.; Absil, O.; Feldt, M.; Garcia, P.J.; Glasse, A.; Guedel, M.; et al. Status update on the development of METIS, the mid-infrared ELT imager and spectrograph. In *Ground-Based and Airborne Instrumentation for Astronomy IX*; SPIE: Bellingham, WA, USA, 2022; Volume 12184, pp. 690–705.
305. Drossart, P. Saturn tropospheric water measured with ISO/SWS. In *AAS/Division for Planetary Sciences Meeting Abstracts# 30*; AAS: Washington, DC, USA, 1998; Volume 30, p. 1060.
306. Öberg, K.I.; Murray-Clay, R.; Bergin, E.A. The effects of snowlines on C/O in planetary atmospheres. *Astrophys. J. Lett.* **2011**, *743*, L16. [[CrossRef](#)]
307. Mousis, O.; Lunine, J.I.; Madhusudhan, N.; Johnson, T.V. Nebular water depletion as the cause of Jupiter's low oxygen abundance. *Astrophys. J. Lett.* **2012**, *751*, L7. [[CrossRef](#)]
308. Lunine, J.I.; Hunten, D.M. Abundance of condensable species at planetary cold traps: The role of moist convection. *Planet. Space Sci.* **1989**, *37*, 151–166. [[CrossRef](#)]

309. Taylor, F.; Atreya, S.; Encrenaz, T.; Hunten, D.; Irwin, P.; Owen, T. The composition of the atmosphere of Jupiter. In *Jupiter: The Planet, Satellites and Magnetosphere*; Cambridge University Press: Cambridge, UK, 2004; pp. 59–78.
310. Giles, R.S.; Fletcher, L.N.; Irwin, P.G. Latitudinal variability in Jupiter’s tropospheric disequilibrium species: GeH<sub>4</sub>, AsH<sub>3</sub> and PH<sub>3</sub>. *Icarus* **2017**, *289*, 254–269. [[CrossRef](#)]
311. Moreno, R.; Marten, A.; Lellouch, E. Search for PH<sub>3</sub> in the atmospheres of Uranus and Neptune at millimeter wavelength. In *AAS/Division for Planetary Sciences Meeting Abstracts# 41*; AAS: Washington, DC, USA, 2009; Volume 41, p. 28.02.
312. Lecluse, C.; Robert, F.; Gautier, D.; Guiraud, M. Deuterium enrichment in giant planets. *Planet. Space Sci.* **1996**, *44*, 1579–1592. [[CrossRef](#)]
313. Griffin, M.; Naylor, D.; Davis, G.; Ade, P.A.; Oldham, P.; Swinyard, B.; Gautier, D.; Lellouch, E.; Orton, G.; Encrenaz, T.; et al. First detection of the 56- $\mu\text{m}$  rotational line of HD in Saturn’s atmosphere. *Astron. Astrophys.* **1996**, *315*, L389–L392.
314. Feuchtgruber, H.; Lellouch, E.; Bézard, B.; Encrenaz, T.; de Graauw, T.; Davis, G. Detection of HD in the atmospheres of Uranus and Neptune: A new determination of the D/H ratio. *Astron. Astrophys.* **1999**, *341*, L17–L21.
315. Lellouch, E.; Bézard, B.; Fouchet, T.; Feuchtgruber, H.; Encrenaz, T.; de Graauw, T. The deuterium abundance in Jupiter and Saturn from ISO-SWS observations. *Astron. Astrophys.* **2001**, *370*, 610–622. [[CrossRef](#)]
316. Moses, J.I.; Allen, M.; Yung, Y.L. Hydrocarbon nucleation and aerosol formation in Neptune’s atmosphere. *Icarus* **1992**, *99*, 318–346. [[CrossRef](#)] [[PubMed](#)]
317. Moses, J.I.; Fletcher, L.N.; Greathouse, T.K.; Orton, G.S.; Hue, V. Seasonal stratospheric photochemistry on Uranus and Neptune. *Icarus* **2018**, *307*, 124–145. [[CrossRef](#)] [[PubMed](#)]
318. Lellouch, E.; Moreno, R.; Orton, G.; Feuchtgruber, H.; Cavalié, T.; Moses, J.; Hartogh, P.; Jarchow, C.; Sagawa, H. New constraints on the CH<sub>4</sub> vertical profile in Uranus and Neptune from Herschel observations. *Astron. Astrophys.* **2015**, *579*, A121. [[CrossRef](#)]
319. Baines, K.H.; Smith, W.H. The atmospheric structure and dynamical properties of Neptune derived from ground-based and IUE spectrophotometry. *Icarus* **1990**, *85*, 65–108. [[CrossRef](#)]
320. Baines, K.H.; Hammel, H.B. Clouds, hazes, and the stratospheric methane abundance in Neptune. *Icarus* **1994**, *109*, 20–39. [[CrossRef](#)] [[PubMed](#)]
321. Stoker, C.R. Moist convection: A mechanism for producing the vertical structure of the Jovian equatorial plumes. *Icarus* **1986**, *67*, 106–125. [[CrossRef](#)]
322. Orton, G.S.; Encrenaz, T.; Leyrat, C.; Puetter, R.; Friedson, A.J. Evidence for methane escape and strong seasonal and dynamical perturbations of Neptune’s atmospheric temperatures. *Astron. Astrophys.* **2007**, *473*, L5–L8. [[CrossRef](#)]
323. Appleby, J.F. Radiative-convective equilibrium models of Uranus and Neptune. *Icarus* **1986**, *65*, 383–405. [[CrossRef](#)]
324. Friedson, J.; Ingersoll, A.P. Seasonal meridional energy balance and thermal structure of the atmosphere of Uranus: A radiative-convective-dynamical model. *Icarus* **1987**, *69*, 135–156. [[CrossRef](#)]
325. Marley, M.S.; McKay, C.P. Thermal structure of Uranus’ atmosphere. *Icarus* **1999**, *138*, 268–286. [[CrossRef](#)] [[PubMed](#)]
326. Li, C.; Le, T.; Zhang, X.; Yung, Y.L. A high-performance atmospheric radiation package: With applications to the radiative energy budgets of giant planets. *J. Quant. Spectrosc. Radiat. Transf.* **2018**, *217*, 353–362. [[CrossRef](#)]
327. Melin, H.; Fletcher, L.N.; Irwin, P.G.; Edgington, S.G. Jupiter in the Ultraviolet: Acetylene and Ethane Abundances in the Stratosphere of Jupiter from Cassini Observations between 0.15 and 0.19  $\mu\text{m}$ . *Astron. J.* **2020**, *159*, 291. [[CrossRef](#)]
328. Lellouch, E.; Bézard, B.; Moses, J.; Davis, G.; Drossart, P.; Feuchtgruber, H.; Bergin, E.; Moreno, R.; Encrenaz, T. The origin of water vapor and carbon dioxide in Jupiter’s stratosphere. *Icarus* **2002**, *159*, 112–131. [[CrossRef](#)]
329. Encrenaz, T.; Lellouch, E.; Feuchtgruber, H.; Altieri, B.; Bézard, B.; Davis, M.; de Graauw, T.; Drossart, P.; Griffin, M.; Kessler, M.; et al. The giant planets as seen by ISO. In *The First ISO Workshop on Analytical Spectroscopy*; ESA Publications Division: Noordwijk, The Netherlands, 1997; Volume 419, p. 125.
330. Moses, J.I.; Poppe, A.R. Dust ablation on the giant planets: Consequences for stratospheric photochemistry. *Icarus* **2017**, *297*, 33–58. [[CrossRef](#)] [[PubMed](#)]
331. Seager, S.; Deming, D. Exoplanet atmospheres. *Annu. Rev. Astron. Astrophys.* **2010**, *48*, 631–672. [[CrossRef](#)]
332. Barstow, J.K.; Heng, K. Outstanding challenges of exoplanet atmospheric retrievals. *Space Sci. Rev.* **2020**, *216*, 82. [[CrossRef](#)]
333. Antunano, A.; Fletcher, L.N.; Orton, G.S.; Melin, H.; Donnelly, P.T.; Roman, M.T.; Sinclair, J.A.; Kasaba, Y. Cycles of Variability in Jupiter’s Atmosphere from Ground-Based Mid-Infrared Observations. In *Proceedings of the European Planetary Science Congress 2021*, Online, 13–24 September 2021.
334. Fletcher, L.N.; Kaspi, Y.; Guillot, T.; Showman, A.P. How well do we understand the belt/zone circulation of giant planet atmospheres? *Space Sci. Rev.* **2020**, *216*, 30. [[CrossRef](#)]
335. Dowling, T. Emoticons for Teaching Jupiter’s Belts, Zones, and Spots. In *AAS/Division for Planetary Sciences Meeting Abstracts*; AAS: Washington, DC, USA, 2021; Volume 53, p. 410.10.
336. Conrath, B.J.; Gierasch, P.J. Global variation of the para hydrogen fraction in Jupiter’s atmosphere and implications for dynamics on the outer planets. *Icarus* **1984**, *57*, 184–204. [[CrossRef](#)]
337. de Pater, I.; Fletcher, L.N.; Reach, W.T.; Goullaud, C.; Orton, G.S.; Wong, M.H.; Gehrz, R.D. SOFIA Observations of Variability in Jupiter’s Para-H<sub>2</sub> Distribution and Subsurface Emission Characteristics of the Galilean Satellites. *Planet. Sci. J.* **2021**, *2*, 226. [[CrossRef](#)]
338. Porco, C.C.; West, R.A.; McEwen, A.; Del Genio, A.D.; Ingersoll, A.P.; Thomas, P.; Squyres, S.; Dones, L.; Murray, C.D.; Johnson, T.V.; et al. Cassini imaging of Jupiter’s atmosphere, satellites, and rings. *Science* **2003**, *299*, 1541–1547. [[CrossRef](#)] [[PubMed](#)]

339. García-Melendo, E.; Pérez-Hoyos, S.; Sánchez-Lavega, A.; Hueso, R. Saturn's zonal wind profile in 2004–2009 from Cassini ISS images and its long-term variability. *Icarus* **2011**, *215*, 62–74. [[CrossRef](#)]
340. Tollefson, J.; Wong, M.H.; Pater, I.d.; Simon, A.A.; Orton, G.S.; Rogers, J.H.; Atreya, S.K.; Cosentino, R.G.; Januszewski, W.; Morales-Juberías, R.; et al. Changes in Jupiter's Zonal Wind Profile preceding and during the Juno mission. *Icarus* **2017**, *296*, 163–178. [[CrossRef](#)]
341. Sromovsky, L.; Fry, P.; Dowling, T.; Baines, K.; Limaye, S. Neptune's atmospheric circulation and cloud morphology: Changes revealed by 1998 HST imaging. *Icarus* **2001**, *150*, 244–260. [[CrossRef](#)]
342. Sromovsky, L.; Fry, P. Dynamics of cloud features on Uranus. *Icarus* **2005**, *179*, 459–484. [[CrossRef](#)]
343. Liang, M.C.; Shia, R.L.; Lee, A.Y.T.; Allen, M.; Friedson, A.J.; Yung, Y.L. Meridional transport in the stratosphere of Jupiter. *Astrophys. J.* **2005**, *635*, L177. [[CrossRef](#)]
344. Zhang, X.; West, R.; Banfield, D.; Yung, Y. Stratospheric aerosols on Jupiter from Cassini observations. *Icarus* **2013**, *226*, 159–171. [[CrossRef](#)]
345. Orsolini, Y.; Leovy, C. A model of large-scale instabilities in the jovian troposphere: 1. Linear model. *Icarus* **1993**, *106*, 392–405. [[CrossRef](#)]
346. Ingersoll, A.; Gierasch, P.; Banfield, D.; Vasavada, A.; Team, G.I. Moist convection as an energy source for the large-scale motions in Jupiter's atmosphere. *Nature* **2000**, *403*, 630–632. [[CrossRef](#)]
347. Ingersoll, A.P.; Atreya, S.; Bolton, S.J.; Brueshaber, S.; Fletcher, L.N.; Levin, S.M.; Li, C.; Li, L.; Lunine, J.I.; Orton, G.S.; et al. Jupiter's overturning circulation: Breaking waves take the place of solid boundaries. *Geophys. Res. Lett.* **2021**, *48*, e2021GL095756. [[CrossRef](#)] [[PubMed](#)]
348. Duer, K.; Gavriel, N.; Galanti, E.; Kaspi, Y.; Fletcher, L.N.; Guillot, T.; Bolton, S.J.; Levin, S.M.; Atreya, S.K.; Grassi, D.; et al. Evidence for multiple Ferrel-like cells on Jupiter. *Geophys. Res. Lett.* **2021**, *48*, e2021GL095651. [[CrossRef](#)]
349. Fletcher, L.N.; Oyafuso, F.A.; Allison, M.; Ingersoll, A.; Li, L.; Kaspi, Y.; Galanti, E.; Wong, M.H.; Orton, G.S.; Duer, K.; et al. Jupiter's temperate belt/zone contrasts revealed at depth by Juno microwave observations. *J. Geophys. Res. Planets* **2021**, *126*, e2021JE006858. [[CrossRef](#)]
350. Achterberg, R.; Flasar, F.; BJORAKER, G.; Hesman, B.; GORIOUS, N.; Mamoutkine, A.; Fletcher, L.; Segura, M.; Edgington, S.; Brooks, S. Thermal Emission From Saturn's Polar Cyclones. *Geophys. Res. Lett.* **2018**, *45*, 5312–5319. [[CrossRef](#)]
351. Fletcher, L.N.; Guerlet, S.; Orton, G.S.; Cosentino, R.G.; Fouchet, T.; Irwin, P.G.; Li, L.; Flasar, F.M.; GORIOUS, N.; Morales-Juberías, R. Disruption of Saturn's quasi-periodic equatorial oscillation by the great northern storm. *Nat. Astron.* **2017**, *1*, 765–770. [[CrossRef](#)]
352. Flasar, F.; Conrath, B.; Gierasch, P.; Pirraglia, J. Voyager infrared observations of Uranus' atmosphere: Thermal structure and dynamics. *J. Geophys. Res. Space Phys.* **1987**, *92*, 15011–15018. [[CrossRef](#)]
353. Sánchez-Lavega, A.; Sromovsky, L.; Showman, A.P.; Del Genio, A.; Young, R.; Hueso, R.; Garcia-Melendo, E.; Kaspi, Y.; Orton, G.S.; Barrado-Izagirre, N.; et al. Gas giants. In *Zonal Jets*; Technical Report; Cambridge University Press: Cambridge, UK, 2019.
354. Hammel, H.; de Pater, I.; Gibbard, S.; Lockwood, G.; Rages, K. New cloud activity on Uranus in 2004: First detection of a southern feature at 2.2  $\mu\text{m}$ . *Icarus* **2005**, *175*, 284–288. [[CrossRef](#)]
355. Hammel, H.; Lynch, D.; Russell, R.; Sitko, M.; Bernstein, L.; Hewagama, T. Mid-infrared ethane emission on Neptune and Uranus. *Astrophys. J.* **2006**, *644*, 1326. [[CrossRef](#)]
356. Orton, G.S.; Fletcher, L.N.; Liu, J.; Schneider, T.; Yanamandra-Fisher, P.A.; de Pater, I.; Edwards, M.; Geballe, T.R.; Hammel, H.B.; Fujiyoshi, T.; et al. Recovery and characterization of Neptune's near-polar stratospheric hot spot. *Planet. Space Sci.* **2012**, *61*, 161–167. [[CrossRef](#)]
357. Orton, G.; Moses, J.; Encrenaz, T.; Fletcher, L.; Greathouse, T.; Leyrat, C.; Sinclair, J.; Trafton, L.; Lacy, J.; Pantin, E. Spatial Variability in the Stratosphere of Uranus. In Proceedings of the 42nd COSPAR Scientific Assembly, Pasadena, CA, USA, 14–22 July, 2018; Volume 42.
358. Peek, B.M.; Moore, P. *The Planet Jupiter: The Observer's Handbook*; Faber and Faber: London, UK; Boston, MA, USA, 1981.
359. Rogers, J.H. *The Giant Planet Jupiter*; Cambridge University Press: Cambridge, UK, 1995; Volume 6.
360. Simon-Miller, A.A.; Gierasch, P.J. On the long-term variability of Jupiter's winds and brightness as observed from Hubble. *Icarus* **2010**, *210*, 258–269. [[CrossRef](#)]
361. Karkoschka, E.; Tomasko, M. Saturn's vertical and latitudinal cloud structure 1991–2004 from HST imaging in 30 filters. *Icarus* **2005**, *179*, 195–221. [[CrossRef](#)]
362. Lockwood, G.; Thompson, D. Photometric variability of Neptune, 1972–2000. *Icarus* **2002**, *156*, 37–51. [[CrossRef](#)]
363. Lockwood, G.; Jerzykiewicz, M. Photometric variability of Uranus and Neptune, 1950–2004. *Icarus* **2006**, *180*, 442–452. [[CrossRef](#)]
364. Sromovsky, L.A.; Fry, P.; Hammel, H.; Ahue, W.; de Pater, I.; Rages, K.; Showalter, M.; van Dam, M. Uranus at equinox: Cloud morphology and dynamics. *Icarus* **2009**, *203*, 265–286. [[CrossRef](#)]
365. Roman, M.T.; Banfield, D.; Gierasch, P.J. Aerosols and methane in the ice giant atmospheres inferred from spatially resolved, near-infrared spectra: I. Uranus, 2001–2007. *Icarus* **2018**, *310*, 54–76. [[CrossRef](#)]
366. Sromovsky, L.A.; Karkoschka, E.; Fry, P.M.; de Pater, I.; Hammel, H.B. The methane distribution and polar brightening on Uranus based on HST/STIS, Keck/NIRC2, and IRTF/SpEx observations through 2015. *Icarus* **2019**, *317*, 266–306. [[CrossRef](#)]
367. Lockwood, G. Final compilation of photometry of Uranus and Neptune, 1972–2016. *Icarus* **2019**, *324*, 77–85. [[CrossRef](#)]
368. Karkoschka, E. Neptune's cloud and haze variations 1994–2008 from 500 HST-WFPC2 images. *Icarus* **2011**, *215*, 759–773. [[CrossRef](#)]

369. Hueso, R.; De Pater, I.; Simon, A.; Sánchez-Lavega, A.; Delcroix, M.; Wong, M.; Tollefson, J.; Baranec, C.; de Kleer, K.; Luszcz-Cook, S.; et al. Neptune long-lived atmospheric features in 2013–2015 from small (28-cm) to large (10-m) telescopes. *Icarus* **2017**, *295*, 89–109. [CrossRef]
370. Wong, M.H.; Tollefson, J.; Hsu, A.I.; de Pater, I.; Simon, A.A.; Hueso, R.; Sánchez-Lavega, A.; Sromovsky, L.; Fry, P.; Luszcz-Cook, S.; et al. A new dark vortex on Neptune. *Astron. J.* **2018**, *155*, 117. [CrossRef]
371. Molter, E.; de Pater, I.; Luszcz-Cook, S.; Hueso, R.; Tollefson, J.; Alvarez, C.; Sánchez-Lavega, A.; Wong, M.H.; Hsu, A.I.; Sromovsky, L.A.; et al. Analysis of Neptune’s 2017 bright equatorial storm. *Icarus* **2019**, *321*, 324–345. [CrossRef]
372. Hueso, R.; Sánchez-Lavega, A. Atmospheric dynamics and vertical structure of Uranus and Neptune’s weather layers. *Space Sci. Rev.* **2019**, *215*, 52. [CrossRef]
373. Simon, A.A.; Wong, M.H.; Sromovsky, L.A.; Fletcher, L.N.; Fry, P.M. Giant Planet Atmospheres: Dynamics and Variability from UV to Near-IR Hubble and Adaptive Optics Imaging. *Remote Sens.* **2022**, *14*, 1518. [CrossRef]
374. Mitchell, J.M. An overview of climatic variability and its causal mechanisms. *Quat. Res.* **1976**, *6*, 481–493. [CrossRef]
375. Wallace, L. The seasonal variation of the thermal structure of the atmosphere of Uranus. *Icarus* **1983**, *54*, 110–132. [CrossRef]
376. Greathouse, T.; Strong, S.; Moses, J.; Orton, G.; Fletcher, L.; Dowling, T. A General Radiative Seasonal Climate Model Applied to Saturn, Uranus, and Neptune. In *AGU Fall Meeting Abstracts*; AGU: Washington, DC, USA, 2008; Volume 2008, p. P21B-06.
377. Seidelmann, P.K. *Explanatory Supplement to the Astronomical Almanac*; University Science Books: Melville, NY, USA, 1992.
378. Meeus, J. Equinoxes and solstices on Uranus and Neptune. *J. Br. Astron. Assoc.* **1997**, *107*, 332.
379. Fletcher, L.N.; Irwin, P.; Sinclair, J.; Orton, G.; Giles, R.; Hurley, J.; Gorius, N.; Achterberg, R.; Hesman, B.; Bjoraker, G. Seasonal evolution of Saturn’s polar temperatures and composition. *Icarus* **2015**, *250*, 131–153. [CrossRef]
380. Kopp, G. SORCE Level 3 Total Solar Irradiance Daily Means, Version 018. 2019. Available online: [https://disc.gsfc.nasa.gov/datasets/SOR3TSID\\_019/summary](https://disc.gsfc.nasa.gov/datasets/SOR3TSID_019/summary) (accessed on 15 October 2022).
381. Orton, G.S.; Gustafsson, M.; Burgdorf, M.; Meadows, V. Revised ab initio models for H<sub>2</sub>–H<sub>2</sub> collision-induced absorption at low temperatures. *Icarus* **2007**, *189*, 544–549. [CrossRef]
382. Cavalié, T.; Dobrijevic, M.; Fletcher, L.N.; Loison, J.C.; Hickson, K.; Hue, V.; Hartogh, P. Photochemical response to the variation of temperature in the 2011–2012 stratospheric vortex of Saturn. *Astron. Astrophys.* **2015**, *580*, A55. [CrossRef]
383. Hue, V.; Hersant, F.; Cavalié, T.; Dobrijevic, M.; Sinclair, J. Photochemistry, mixing and transport in Jupiter’s stratosphere constrained by Cassini. *Icarus* **2018**, *307*, 106–123. [CrossRef]
384. Orton, G.S.; Friedson, A.J.; Yanamandra-Fisher, P.A.; Caldwell, J.; Hammel, H.B.; Baines, K.H.; Bergstralh, J.T.; Martin, T.Z.; West, R.A.; Veeder, G.J., Jr.; et al. Spatial organization and time dependence of Jupiter’s tropospheric temperatures, 1980–1993. *Science* **1994**, *265*, 625–631. [CrossRef] [PubMed]
385. Antuñano, A.; Fletcher, L.N.; Orton, G.S.; Melin, H.; Milan, S.; Rogers, J.; Greathouse, T.; Harrington, J.; Donnelly, P.T.; Giles, R. Jupiter’s atmospheric variability from long-term ground-based observations at 5 μm. *Astron. J.* **2019**, *158*, 130. [CrossRef]
386. Friedson, A.J. New observations and modelling of a QBO-like oscillation in Jupiter’s stratosphere. *Icarus* **1999**, *137*, 34–55. [CrossRef]
387. Antuñano, A.; Cosentino, R.G.; Fletcher, L.N.; Simon, A.A.; Greathouse, T.K.; Orton, G.S. Fluctuations in Jupiter’s equatorial stratospheric oscillation. *Nat. Astron.* **2021**, *5*, 71–77. [CrossRef]
388. Ortiz, J.; Orton, G.; Friedson, A.; Stewart, S.; Fisher, B.; Spencer, J. Evolution and persistence of 5-μm hot spots at the Galileo probe entry latitude. *J. Geophys. Res. Planets* **1998**, *103*, 23051–23069. [CrossRef]
389. Orton, G.S.; Antunano, A.; Fletcher, L.N.; Sinclair, J.A.; Momary, T.W.; Fujiyoshi, T.; Yanamandra-Fisher, P.; Donnelly, P.T.; Greco, J.J.; Payne, A.V.; et al. Unexpected Long-Term Variability in Jupiter’s Tropospheric Temperatures. *arXiv* **2022**, arXiv:2211.04398.
390. Leovy, C.B.; Friedson, A.J.; Orton, G.S. The quasiquadrennial oscillation of Jupiter’s equatorial stratosphere. *Nature* **1991**, *354*, 380–382. [CrossRef]
391. Greathouse, T.K.; Orton, G.S.; Cosentino, R.; Morales-Juberias, R.; Fletcher, L.N.; Giles, R.S.; Melin, H.; Encrenaz, T.A.; Fouchet, T.; DeWitt, C.N. Tracking Jupiter’s Quasi-Quadrennial Oscillation and Mid-Latitude Zonal Waves with High Spectral Resolution Mid-Infrared Observations. In *AAS/Division for Planetary Sciences Meeting Abstracts# 48*; AAS: Washington, DC, USA, 2016; Volume 48, p. 501.05.
392. Hue, V.; Greathouse, T.; Cavalié, T.; Dobrijevic, M.; Hersant, F. 2D photochemical modeling of Saturn’s stratosphere. Part II: Feedback between composition and temperature. *Icarus* **2016**, *267*, 334–343. [CrossRef]
393. Bardet, D.; Spiga, A.; Guerlet, S. Joint evolution of equatorial oscillation and interhemispheric circulation in Saturn’s stratosphere. *Nat. Astron.* **2022**, *6*, 804–811. [CrossRef]
394. Orton, G.; Yanamandra-Fisher, P. Saturn’s temperature field from high-resolution middle-infrared imaging. *Science* **2005**, *307*, 696–698. [CrossRef]
395. Fischer, G.; Kurth, W.S.; Gurnett, D.A.; Zarka, P.; Dyudina, U.A.; Ingersoll, A.P.; Ewald, S.P.; Porco, C.C.; Wesley, A.; Go, C.; Delcroix, M. A giant thunderstorm on Saturn. *Nature* **2011**, *475*, 75–77. [CrossRef] [PubMed]

**Disclaimer/Publisher’s Note:** The statements, opinions and data contained in all publications are solely those of the individual author(s) and contributor(s) and not of MDPI and/or the editor(s). MDPI and/or the editor(s) disclaim responsibility for any injury to people or property resulting from any ideas, methods, instructions or products referred to in the content.